Monolithic integration of silicon and polymer microstructures for Organ-on-Chip applications

Quiros Solano, William

DOI
10.4233/uuid:a03c8a30-4ab9-4bc1-9512-dd75cd3b5314

Publication date
2019

Document Version
Final published version

Citation (APA)
Quiros Solano, W. (2019). *Monolithic integration of silicon and polymer microstructures for Organ-on-Chip applications*. [Dissertation (TU Delft), Delft University of Technology]. https://doi.org/10.4233/uuid:a03c8a30-4ab9-4bc1-9512-dd75cd3b5314

MONOLITHIC INTEGRATION OF SILICON AND POLYMER MICROSTRUCTURES FOR ORGAN-ON-CHIP APPLICATIONS

MONOLITHIC INTEGRATION OF SILICON AND POLYMER MICROSTRUCTURES FOR ORGAN-ON-CHIP APPLICATIONS

Proefschrift

ter verkrijging van de graad van doctor
aan de Technische Universiteit Delft,
op gezag van de Rector Magnificus prof. dr. ir. T.H.J.J. van der Hagen,
voorzitter van het College voor Promoties,
in het openbaar te verdedigen op maandag 8 juli 2019 om 12:30 uur

door

William Fausto QUIRÓS SOLANO

Master of Science in Electronics Engineering,
Instituto Tecnológico de Costa Rica, Cartago, Costa Rica,
geboren te Turrialba, Costa Rica.

Dit proefschrift is goedgekeurd door de

promotor: prof. dr. ir. P.M. Sarro

Samenstelling promotiecommissie:

Rector Magnificus,	voorzitter
Prof. dr. ir. P.M. Sarro,	Technische Universiteit Delft
Onafhankelijke leden:	
Prof. dr. P.G. Steeneken,	Technische Universiteit Delft
Prof. dr. rer. nat. W. Mokwa,	RWTH Aachen University
Prof. dr. ir. J.M.J. den Toonder,	Technische Universiteit Eindhoven
Prof. dr. G. Barillaro,	University of Pisa
Prof. dr. P.J. French,	Technische Universiteit Delft, reservelid
Overige leden:	
Prof. dr. ir. R. Dekker,	Technische Universiteit Delft
Dr. G. Pandraud,	Technische Universiteit Delft

Keywords: Organ-on-Chip, MEMS, Silicon, PDMS, Membranes, Cell, Strain, Stress.

Printed by: Ipskamp.

Front & Back: Cover design by Luis Diego Obando Fernández, OZ Diseño.

ISBN 978-94-6384-051-4

A Dios,
por sus bendiciones.

A mi madre Martha,
a quien debo lo que soy.

A mi hermana Mariam,
quien siempre cree en mí.

A mi tío y abuelas, Ricardo, Belén y Cruz,
quienes siempre me apoyan.

A Laura,
por su amor incondicional.

CONTENTS

1

INTRODUCTION

"If you hear a voice within you say,'You cannot paint', then by all means paint, and that voice will be silenced."

Vincent van Gogh

1.1. PHARMACEUTICAL INDUSTRY AND DRUG DEVELOPMENT

Drug development is a complex, time-consuming and expensive process. The net expenses covered by the pharmaceutical industry after going through such complicated and long process (10 - 15 years) have been estimated to be around $2.6 billion for each new medicine that reaches the market [1]. Only in the European Union (EU), €26 billion were spent for drug development in 2007, involving more than 100 thousand scientists [2]. Around 32% of the total development costs are spent for *in vitro* screening studies [3].

Nevertheless, the risk of discovering adverse effects or toxicity cases after the drug has been brought to the market is always present. Once a toxicity case has been detected and confirmed, the new medicine is immediately withdrawn from the market. Such course of action is taken by regulatory authorities, especially when deaths might be attributed to the use of the new medicine [4]. A recent study estimates that between 1953 and 2013, 644 medicines were withdrawn from the market for different reasons (environmental, commercial or legal issues). Out of those withdraws, at least 462 cases were due to adverse effects such as hepatotoxicity, cardiotoxicity and neurotoxicity [5]. The pharmaceutical industry is well aware of this problem and has started evaluating over the years the procedures employed to assess safety in the many phases of the drug development process.

1.1.1. THE DRUG DEVELOPMENT PROCESS

Drug development can be divided in four main stages (Fig. 1.1a-f): target discovery or basic reserch, drug discovery, preclinical trials and clinical trials (Phase I - Phase III) [6, 7].

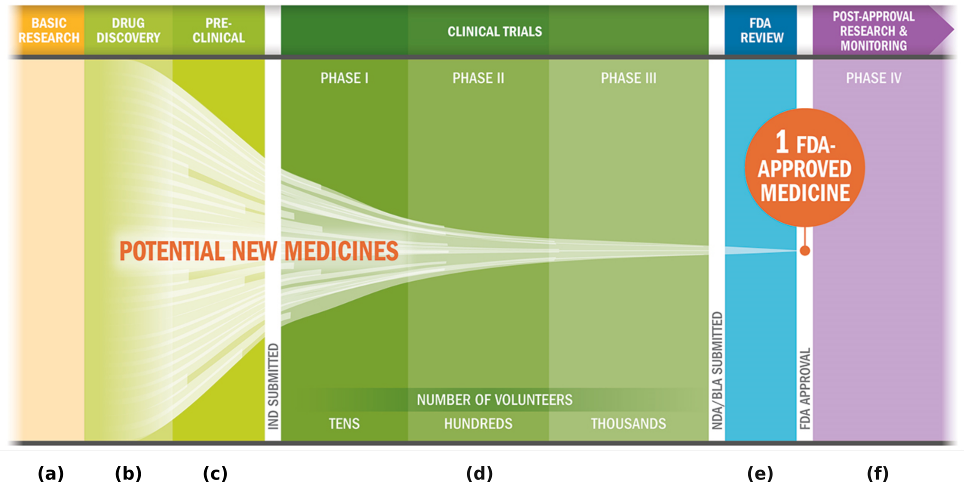

Figure 1.1: The drug development process. A long and extensive process comprising of four main stages: **(a)** Target discovery or Basic Research, **(b)** Drug discovery, **(c)** Preclinical trials, **(d)** Clinical trials. The process normally takes at least 10 years up to the moment of review **(e)** of the regulatory authorities. A final period of survaillance or post-aproval research **(f)** is given to monitor possible toxicity effects, often refered as Phase IV of clinical trials. Data and images adapted and reproduced with permission from [7, 8].

During the first stage, target discovery or basic research, key molecular and physiological mechanisms known to be related to a disease are studied in detail. The aim is to isolate specific proteins or micro-organisms strongly correlated with the symptomatology of the disease under study. Special attention is given to understand how certain molecules change over time and their influence in cell behaviour (*pathways*) thus establishing them as the target to mitigate [9–11]. Once such target is discovered and properly understood, the next phase can initiate.

The aim of the drug discovery stage is to find either a synthetic or biological compound that can alter the pathways of the target. Such alterations are expected to have a significant effect on the way the disease manifests in the patient. Once this happens, a so-called *hit* is found, the compound undergoes further improvements to increase its safety and effectiveness. In this phase up to 10000 compounds are tested, mainly using high-throughput *in vitro* screening procedures and computer simulation [7, 8].

Once the hit compound has successfully passed the initial screening, it becomes a *drug candidate* and the preclinical trials can be initiated. In such a stage, the safety of the new compound is evaluated, focusing on detecting any potential side effects and understanding the dosage dynamics. This is considered a critical phase since it aims at initially guaranteeing the maximum safety of the drug candidate. As in the previous phase, *in-vitro* screening procedures are used to do such a safety assessment, but in this case with a lower throughput as the number of drug candidates is lower than the number of hit compounds in previous phase. The use of animal models to test a drug candidate was also introduced several decades ago as secondary approach. This approach has been instated because some disease mechanisms and interactions with the drug candidate could only be observed under *in vivo* conditions, though not yet safe enough to test in humans. This method was later properly instated as a requirement for entities developing new drugs to minimize the risks during the subsequent human trials [12].

The final stage, before submission to regulatory authorities, is the clinical trials where the first test in human subjects are done to further evaluate both safety and efficacy of the drug candidate. This stage is often held in three phases: Phase I to Phase III. In Phase I, the drug candidate is tested on healthy human individuals to understand and discriminate additional toxicity effects and model the dynamics of the compound inside the human body. In Phase II, the drug candidate is tested in patients suffering from the specific disease the drug is targeting, focusing on monitoring the efficacy, possible side effects, proper dosage and to map the differences observed with respect to the results obtained with healthy individuals. During this phase the drug candidate is assessed in experiments with groups of up to 200 people. Subsequently, in phase III, the test group is increased to up to 3000 people to monitor side effects and acquire relevant statistical data to quantify efficacy of the drug candidate on patients and dose dynamics [6, 7].

Once the drug candidate has gone through this whole process, the data gathered from preclinical and clinical trials is provided and registered to the regulatory authorities, which decides whether to grant the licence to market it as a new medicine. The new medicine is then introduced to the market, but with a continuous post-approval research and under surveillance of the regulatory authorities.

1.2. BOTTLENECKS IN DRUG DEVELOPMENT

In the last two decades, it has been estimated that out of the 10000 *hit* compounds assessed for safety with *in vitro* screening at the first stage, only 200 go through to the clinical trials. Approximately one out them will go through the subsequent stages to reach the market [6]. The low conversion of hit compounds into possible drug candidates during the early stage is responsible for a significant part of the total development costs (Figure 1.2). The failure rates in the United States (US), EU and Japan has been estimated having drastically increased between 1990 and 2004, approximately 75% at preclinical stage, 70% at Phase I and 55% at Phase II and Phase III [13].

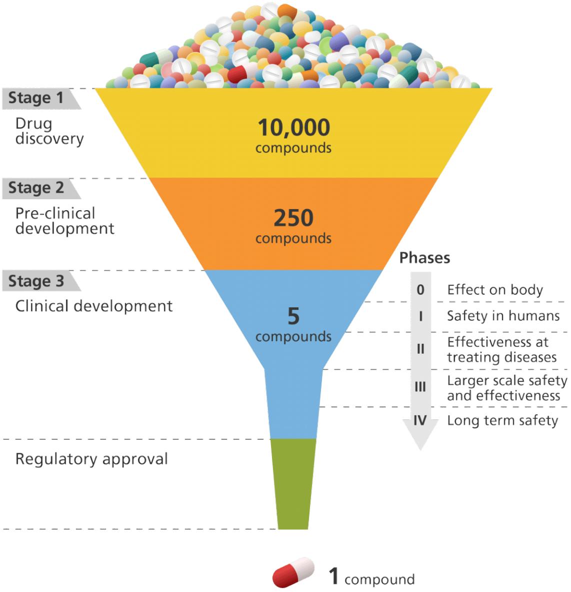

Figure 1.2: An illustratarion of the bottleneck on the number of potential compounds that go trough the whole drug development process and reach market. Image reproduced with the permission from [14].

Studies suggest that only 33% of the positive tests conducted on animals end up in a safe medicine [15], showing that such models are limited and do not always guarantee a high conversion rate of compounds into new medicines. Moreover, this is costly for pharmaceutical companies or biologists since these animals are expensive, used in large amounts and involve time-consuming procedures. The estimated price of mice, the most used animal models [16], is around $200 per subject with several hundreds of them normally used in weekly essays that last a few months.

The bottleneck in the conversion of hit compounds has lately been attributed to the limited accuracy of traditional *in vitro* screening and of the animal testing.

1.2.1. CONVENTIONAL *in vitro* SCREENING

The conventional *in vitro* screening is based on static cell culture models. Essentially, this screening approach consists of culturing cell lines involved in the mechanisms of the disease of interest in a Petri dish (Fig. 1.3). These cells are then exposed to the *hit* compound or candidate drug to observe and study their reaction through *in situ* end-point optical techniques, sequencing, cell staining or destructive essays. The data gathered allow to initially conclude whether there is a positive or negative effect of the compound on the cell behaviour.

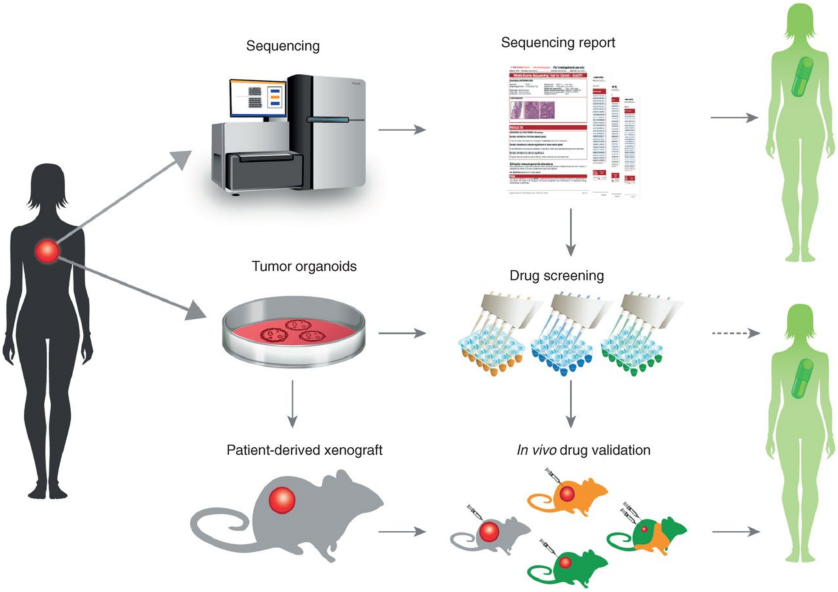

Figure 1.3: An illustration of the typical procedure followed when studying cancer with organoids for drug development. The safety and efficay assesment is carried out using traditional *in vitro* screening and animal testing. Image reproduced with permission from [17].

However, this approach is completely static. The cells are not experiencing certain environmental cues typical of human anatomy and physiology. As recently demonstrated, micro-environmental cues such as shear stress, oxygenation and surface roughness, strongly influence the cell behaviour for many cell lines [18, 19]. Therefore, there are additional variables missing in this approach that could influence the interaction of the cells with the *hit* compound and drug candidates under screening. Eventually, cells might not react or show any indication of toxicity to certain compounds due to the low complexity on the dynamics of the interaction. This causes late toxicity detection or in the worst case only after the new drug is on the market, determining its withdrawal.

Furthermore, the *in vitro* screening is mostly done using animal cell lines which do not faithfully express the same phenotypes as human cells nor consider the genetic background of the patient. In fact, it has been suggested that genetic background might play a key role on how new compounds affect patient responses [20]. New medicines with toxicity cases on only one segment of the population and positive outcomes on another one is an example of how such high heterogeneity in the genetic backgrounds might manifest in the general public [20].

1.2.2. ANIMAL TESTING

Using animal models has been the safest alternative available to study the dynamics and interaction of a candidate compound with a complex living organism prior to conducting exhaustive tests in humans. Animal trials are carried out during the clinical trial stage, specifically in the earliest phase (PHASE I). Different sort of animals serve research laboratories and pharmaceutical companies as test subjects (Fig. 1.4a) [21]. Their similar predisposition to suffer certain disease conditions or the possibility to easily induce on them pathologies and genetic deviations specific of the human disease under study, make them suitable to model the certain human diseases. This has made possible to understand and better model complex diseases such as Huntington's and Parkinsons's disease [22], among others (Fig. 1.4b).

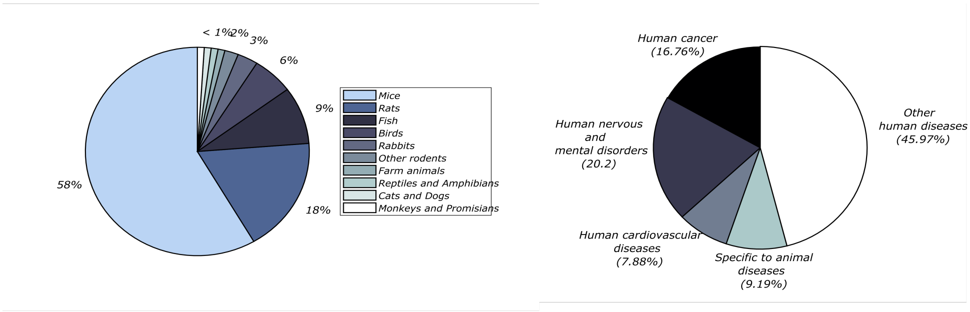

(a) **(b)**

Figure 1.4: **(a)** Statistics on the sort of animals often used in animal trials during the drug development process. **(b)** Proportions of animals used in the EU for studying diseases in 2011. Data taken from [21] and [23].

Nevertheless, there are inevitable differences between human and animal cells which interfere with the accuracy of such models in safety assessment. For instance, minimum differences between cellular ion channels along species can emerge as unreliable results during cardiotoxicity assessments, giving either false positives or false negatives at a later stage [24, 25].

Furthermore, a large effort in favour of animal protection over the last decade has resulted into more legislation aiming at reducing animal testing, thus imposing strong restrictions to all players using such models on a daily basis. Recently, more legislation is emerging to regulate the adherence of drug development research to the so-called Three R's guiding principles (Replacement, Reduction, Refinement) for more ethical use of animal testing [26]. In 2010, the EU with the Directive 2010/63/EU was the first in introducing explicitly legal basis and requirements to its state members, forcing industries to start implementing alternatives to reduce and eventually eliminate the use of animals when conducting research [27].

1.3. TOWARDS ENHANCED *in vitro* SCREENING

Pharmaceutical companies look forward to eliminate the toxicity cases in an early stage, decrease the development costs and to comply with increasingly stringent legislation with respect to animal testing. Biologists and the pharmaceutical industry have therefore started looking into novel alternatives to overcome the limitations imposed by traditional *in vitro* screening and animal testing. Enhanced procedures at all stages are necessary to increase the conversion rate of drug candidates into safer and more accessible medicines reaching the market.

Over the last decades, technological advances have contributed to deal with a variety of diseases, providing advanced tools to develop cures or novel treatments to improve life quality. Particularly, the tendency of the semiconductor industry towards diversification rather than only miniaturization, so-called "More than Moore" law [28, 29], have facilitated the development of technologies with dedicated capabilities. For instance, devices which enable the monitoring of human physiological cues or the stimulation of human tissues to aid or restore key human functions (e.g vision, motion, hearing), are becoming available [30, 31]. Novel high frequency (HF) and optical microdevices, and a variety of microelectromechanical systems (MEMS) allow creating the necessary interactive interfaces between advanced electronics and the human body, expanding the contribution of micro and nano-technologies in health worldwide. However, the potential of technological advances had not been fully exploited in the fundamental research for drug development processes. Thus, over the last two decades there has been an increasing interest to explore the possibility of exploiting micro and nano-technologies to strengthen further the above described processes, specially the safety assessments.

A synergy between microfluidics and tissue engineering, the so-called recently defined Organ-on-Chip (OOC), has been proposed as a potential strong candidate to replace traditional *in vitro* screening. The efforts from Academia have lately reflected in a growing output of publications in the Organ-on-Chip field supported by the last developments in microfluidics and material science, increasing the awareness of pharmaceutical companies on the opportunities that this novel interdisciplinary technology might bring to the drug development process (Fig. 1.5). This new approach promises, in the middle-term, enhancing the traditional *invitro* screening and in the long term, reducing and eventually eliminating animal models in safety and efficacy assessment.

1.3.1. ORGAN-ON-CHIP

Recent progress in tissue engineering on one side and developments in micro and nanotechnologies on the other, have significantly improved the study of cell biology. This progress contributed to originate the so-called Organs-on-Chips (OOCs). These devices exploit further the synergy between such fields to provide a better understanding of the complex mechanisms of the human body. Organ-on-Chip allows to include and accurately control various physical and chemical cues in conventional static cell cultures typically used in *in vitro* screening. The cells, through specifically engineered microstructures, can be subjected to physical cues such as shear stress, mechanical strain and other stimulation cues. A dynamic cell culture is thus created that better recapitulates the intricate *in vivo* conditions of the human body such as muscle cell contraction, blood flow, gradients of concentration and more [34].

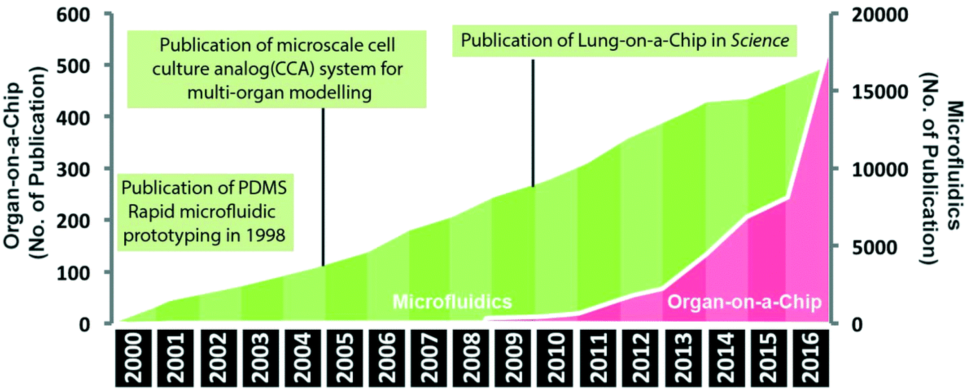

Figure 1.5: A graph showing the rise in research output from Academia in the area of Organ-on-Chip. Continuous advances in microfluidics, specially with the origin of techniques for rapid prototyping with Polydimethylsyloxane (PDMS) and the development of the Lung-on-Chip model [32], have enabled to provide pharmaceutical companies with many potential alternatives for enhanced drug screening. Image reproduced with permission from [33].

Many OOCs have recently allowed to mimic minimal functional units of human organs such as the blood-brain barrier and lung alveolar barrier, among others [15, 35]. As can be seen in Figure 1.6, the long-term goal is to have *in vitro* models of all human organs, namely a body-on-chip, where to perform complete toxicity screening procedures.

1.3.2. INDUCED PLURIPOTENT STEM CELLS

The recent breakthrough made in medicine with the derivation of stem cells from somatic cells, the so-called induced pluripotent stem cells (iPSCs) [37], have contributed to strengthen the possibility of using OOCs as alternative solutions for drug screening. The basic principle and derivation of such stem cells is depicted in Figure 1.7. Briefly, somatic cells taken from an adult, like fibroblasts from skin, are reprogrammed by introducing certain gene transcription factors so that they convert into pluripotent stem cells [37–40]. Such type of cells can then be specialized in any other cell type of the human body (e.g heart, neurons, pancreatic and liver cells) through biochemical or biophysical manipulations.

This breakthrough in cell biology brings the opportunity to progress towards regenerative and personalized medicine. The possibility to obtain the necessary biological material with the genetic background of the patient and the ability to provide dynamic conditions make of OOCs and iPSCs a suitable combination towards the highly envisioned next generation in medical treatments [26, 39, 40]. Thus, this opened the possibility of having an *in vitro* model that not only better recapitulates complex physiological mechanisms but that also includes the genetic background of the patient.

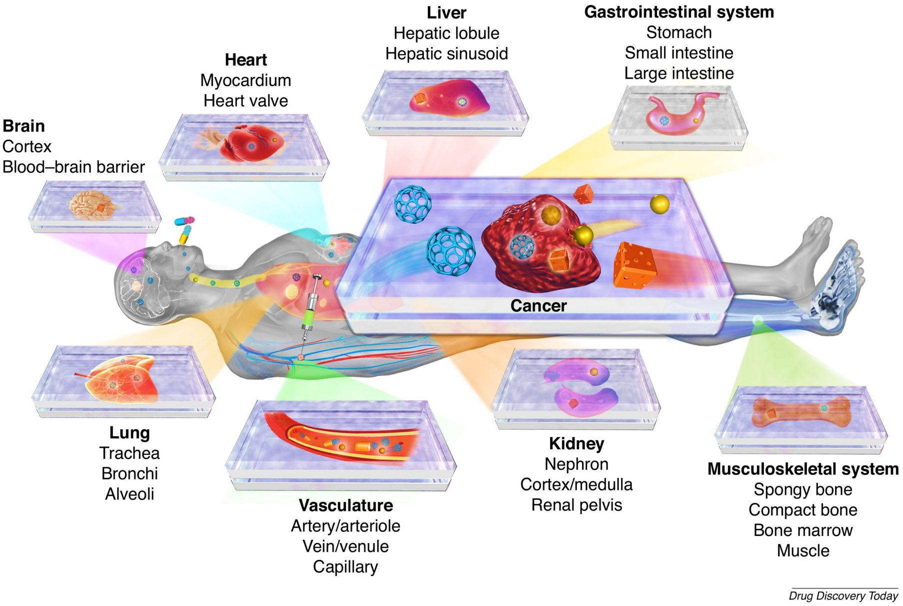

Figure 1.6: An illustration of the so-called Organs-on-Chips models envisioned to provide an alternative for *in vitro* screening of new drug compounds. Dynamic cell microenvironments enabled by artificially made micro and nano-structures, human cells and diverse physical and chemical cues. Image reproduced with permission from [36].

1.4. SCOPE AND OUTLINE OF THIS THESIS

1.4.1. SCOPE

Pharmaceutical companies and biologists recognize in Organs-on-Chips a potential alternative to perform enhanced *in vitro* screening. Lately, they are getting more eager to demonstrate their reliability by investigating technological and biological aspects. Nowadays, it is a promising alternative but at an early stage with many challenges to face. The cross validation of results with relevant clinical data, and the improvement of its fabrication, scalability and adaptability to the conventional drug development pipeline, are among the biggest challenges to overcome to get a robust and practical tool for drug development. Particularly, among the technological challenges, the fully integration of OOCs into the drug development pipeline is mainly limited by the methods currently used to fabricate them. The fabrication is based on techniques originally developed to meet in-house needs of biology researchers, which involve a high degree of manual handling, making them only suitable for the so-called rapid prototyping. Thus, limiting the possibility to exploit all the capabilities enabled by recent advances in Si-based microtechnologies.

The use of integrated circuits (IC) and MEMS fabrication techniques, characterized by their suitability for large scale manufacturing and the large accuracy, reliability and reproducibility, might present an opportunity to adapt these devices, improve their functionality and integrate them in the drug development pipeline. Moreover, this might also

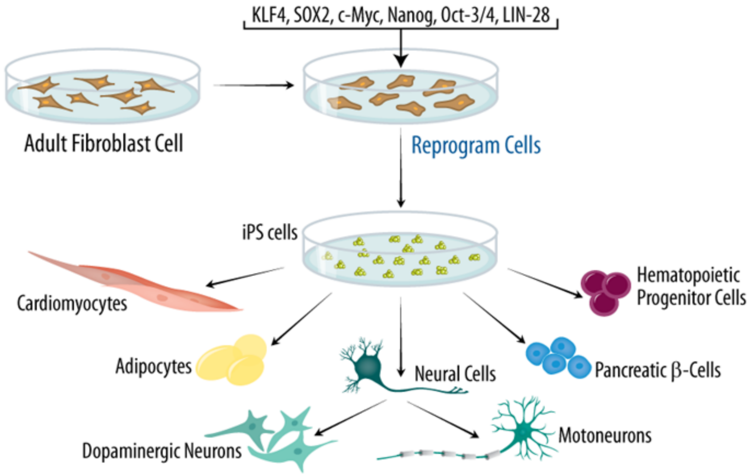

Figure 1.7: An illustration showing the concept of Induced Pluripotent Stem Cells (iPSCs). Most cell types of the human body are obtained reprogramming somatic cells, such as fibroblasts, through either biochemical or biophysical manipulation by introducing gene transcription factors. Image reproduced with permission from [41].

allow to include sensing and actuating microstructures that interface OOCs with high-performance data processing.

This thesis presents important steps aiming to improve the manufacturability of OOCs. The issues with the scalability and reliability of current fabrication methods are studied, and alternatives fabrication methods that exploit the capabilities of IC and MEMS fabrication techniques, are investigated.

1.4.2. OUTLINE

Following, a summary of the topics treated in each chapter of this thesis is given:

In **Chapter** 2, a detailed description on the state of the art of Organs-on-Chips, the fabrication approaches commonly used and challenges to overcome in terms of scalability and manufacturability to integrate OOCs in the drug development pipeline, are presented. Moreover, to facilitate reading of the following chapters, a brief description about relevant technical and biological concepts is given.

In **Chapter** 3, the development of porous PDMS membranes for barrier modelling in OOCs, is presented. Such microfabricated structures are envisioned and proposed as a first important step towards fully microfabricated microstructures for OOCs using IC and MEMS techniques. The chapter focuses on the fabrication of the microstructures, the novel method to enable its use in conventional OOCs, envisioned applications and the corresponding initial biocompatibility assessments.

In **Chapter** 4 further efforts towards manufacturable Organs-on-Chips, are presented. A monolithically microfabricated device as an alternative to currently developed Organs-on-Chips, is presented. In such chapter, design, microfabrication, simulation and fluidic characterization are reported in detail. Moreover, initial experiments on the biological assessment are presented. The envisioned applications of the device are introduced and discussed towards its potential use in *invitro* screening.

Finally, in **Chapter** 5, the demonstration of other possibilities enabled by the use of IC and MEMS techniques for fabricating Organs-on-Chips, are presented. The integration of microstructures that could provide transduction mechanisms to monitor the cell microenvironment are investigated.Specifically, strain gauges for stress sensing as an alternative to monitor *in situ* strain in microfabricated OOCs, are presented. The use of non-conventional polymeric materials in the fabrication of such devices, such as conductive polymers, are also investigated.

REFERENCES

[1] O. Gassmann, G. Reepmeyer, and M. von Zedtwitz, *Igarss 2014*, 1 (Springer-Verlag Berlin Heidelberg, 2014) pp. 1–5, arXiv:arXiv:1011.1669v3 .

[2] T. Hartung, *Food for thought... on evidence-based toxicology,* Altex **26**, 75 (2009).

[3] K. Kaitin, *Deconstructing the Drug Development Process: The New Face of Innovation,* Clin Pharmacol Ther. **87**, 356 (2010).

[4] I. J. Onakpoya, C. J. Heneghan, and J. K. Aronson, *Delays in the post-marketing withdrawal of drugs to which deaths have been attributed: A systematic investigation and analysis,* BMC Medicine **13**, 1 (2015), arXiv:arXiv:1011.1669v3 .

[5] I. J. Onakpoya, C. J. Heneghan, and J. K. Aronson, *Post-marketing withdrawal of 462 medicinal products because of adverse drug reactions: A systematic review of the world literature,* BMC Medicine **14**, 1 (2016).

[6] P. R. Robuck, J. I. Wurzelmann, and M. Merrick, *Understanding the drug development process,* Inflammatory Bowel Diseases **11**, S13 (2005).

[7] PhRMA, *The Biopharmaceutical Research and Development Process,* (2015).

[8] J. A. DiMasi, H. G. Grabowski, and R. W. Hansen, *Innovation in the pharmaceutical industry: New estimates of R&D costs,* Journal of Health Economics **47**, 20 (2016).

[9] B. Xi, N. Yu, X. Wang, X. Xu, and Y. a. Abassi, *The application of cell-based label-free technology in drug discovery,* Biotechnology Journal **3**, 484 (2008).

[10] S. P. MARKEY, *Pathways of drug metabolism,* in *Principles of Clinical Pharmacology* (Elsevier, 2007) pp. 143–162.

[11] G. G. Gibson and P. Skett, *Pathways of drug metabolism,* in *Introduction to Drug Metabolism* (Springer US, 1996) pp. 1–34.

[12] C. to Update Science Medicine and N. R. C. Animals, *Science, Medicine and Animals: A Circle of Discovery* (National Research, 2004).

[13] H. Ledford, *Translational research: 4 ways to fix the clinical trial,* Nature **477**, 526 (2011).

[14] Yourgenome.org, *How are drugs designed and developed?* (2016).

[15] G. B. Drummond, D. J. Paterson, and J. C. McGrath, *Animal research: Reporting in vivo experiments: The ARRIVE guidelines,* Experimental Physiology **95**, 842 (2010), arXiv:NIHMS150003 .

[16] D. K. Desai, Chetna; Badyal, *Animal use in pharmacology education and research: The changing scenario,* Indian Journal of Pharmacology **46**, 257 (2014).

[17] C. Pauli, B. D. Hopkins, D. Prandi, R. Shaw, T. Fedrizzi, A. Sboner, V. Sailer, M. Augello, L. Puca, R. Rosati, T. J. Mcnary, Y. Churakova, C. Cheung, J. Triscott, D. Pisapia, R. Rao, J. M. Mosquera, B. Robinson, B. M. Faltas, B. E. Emerling, V. K. Gadi, B. Bernard, O. Elemento, H. Beltran, F. Demichelis, C. J. Kemp, C. Grandori, L. C. Cantley, and M. A. Rubin, *Personalized In Vitro and In Vivo Cancer Models to Guide Precision Medicine,* Cancer Discovery (2017), 10.1158/2159-8290.CD-16-1154.

[18] H. S. Shin, *Shear Stress Effect on Transfection of Neurons Cultured in Microfluidic Devices,* Journal of Nanoscience and Nanotechnology **9**, 7330 (2009).

[19] D. A. Chistiakov, A. N. Orekhov, and Y. V. Bobryshev, *Effects of shear stress on endothelial cells: go with the flow,* Acta Physiologica **219**, 382 (2017).

[20] K. Lindpaintner, *Genetics in drug discovery and development: Challenge and promise of individualizing treatment in common complex diseases,* British Medical Bulletin **55**, 471 (1999).

[21] R. From, T. H. E. Commission, T. O. The, and T. H. E. European, *REPORT FROM THE COMMISSION TO THE COUNCIL AND THE EUROPEAN: Seventh Report on the Statistics on the Number of Animals used for Experimental and other Scientific Purposes in the Member States of the European Union*, Tech. Rep. (EUROPEAN COMISSION, Brussels, 2013).

[22] S. Ramaswamy, J. L. Mcbride, and J. H. Kordower, *Animal Models of Huntington's Disease,* ILAR Journal **46** (2007).

[23] Science Progress, *The Mouse Trap: How One Rodent Rules the Lab,* (2011).

[24] A. Polini, L. Prodanov, N. S. Bhise, V. Manoharan, M. R. Dokmeci, and A. Khademhosseini, *Organs-on-a-chip: a new tool for drug discovery.* Expert opinion on drug discovery **9**, 335 (2014).

[25] S. N. Bhatia and D. E. Ingber, *Microfluidic organs-on-chips.* Nature biotechnology **32**, 760 (2014).

[26] A. Williamson, S. Singh, U. Fernekorn, and A. Schober, *The future of the patient-specific Body-on-a-chip.* Lab on a chip **13**, 3471 (2013).

[27] European Commission, *Directive 2010/63/EU of the European Parliament and of the Council of 22 September 2010 on the protection of animals used for scientific purposes,* (2010).

[28] S. J. e. a. Wind, *"More-than-Moore" White Paper,* Nature **3**, 758 (2012).

[29] G. Harsányi, *Sensors in biomedical applications. May they change the quality of life?* Sens. Rev. **21**, 259 (2001).

[30] K. Meacham, R. Giuly, and L. Guo, *A lithographically-patterned, elastic multi-electrode array for surface stimulation of the spinal cord,* Biomedical … **10**, 259 (2008).

[31] R. B. North, D. H. Kidd, M. Zahurak, C. S. James, and D. M. Long, *Spinal Cord Stimulation for Chronic, Intractable PainExperience over Two Decades,* Neurosurgery **32**, 384 (1993).

[32] I. D. Huh D, Matthews B, Mammoto A, Montoya-Zavala M, Hsin H, *Reconstituting Organ-Level Lung,* Science **328**, 1662 (2010).

[33] B. Zhang and M. Radisic, *Organ-on-A-chip devices advance to market,* (2017).

[34] D. Huh, Y.-s. Torisawa, G. a. Hamilton, H. J. Kim, and D. E. Ingber, *Microengineered physiological biomimicry: organs-on-chips.* Lab on a chip **12**, 2156 (2012).

[35] R. Booth and H. Kim, *Characterization of a microfluidic in vitro model of the blood-brain barrier (μBBB),* Lab on a Chip **12**, 1784 (2012).

[36] Y. S. Zhang, Y.-n. Zhang, and W. Zhang, *Cancer-on-a-chip systems at the frontier of nanomedicine,* Drug Discovery Today **22**, 1392 (2017).

[37] K. Takahashi, K. Tanabe, M. Ohnuki, M. Narita, T. Ichisaka, K. Tomoda, and S. Yamanaka, *Induction of Pluripotent Stem Cells from Adult Human Fibroblasts by Defined Factors,* Cell **131**, 861 (2007), arXiv:arXiv:1011.1669v3 .

[38] K. Takahashi and S. Yamanaka, *Induced pluripotent stem cells in medicine and biology,* Development **140**, 2457 (2013).

[39] G. Amabile and A. Meissner, *Induced pluripotent stem cells: current progress and potential for regenerative medicine,* Trends in Molecular Medicine **15**, 59 (2009).

[40] A. Rolletschek and A. M. Wobus, *Induced human pluripotent stem cells: Promises and open questions,* Biological Chemistry **390**, 845 (2009).

[41] A. D. Theocharis, S. S. Skandalis, C. Gialeli, and N. K. Karamanos, *Extracellular matrix structure,* Advanced Drug Delivery Reviews **97**, 4 (2016).

2

ORGANS-ON-CHIPS: STATE-OF-THE-ART

2.1. ORGAN-ON-CHIP

Over the last decade, Organs-on-Chips along with the discovery of iPSCs have attracted the attention of academia and pharmaceutical companies due to the high potential to contribute to a better comprehension of human biology, enhanced drug *in vitro* screening and the promise of the highly envisioned personalized and regenerative medicines. Their potential improvement of the scrGenning process relyies in the enhanced capabilities to replicate human anatomy and phisiology [1–6].

2.1.1. REPLICATING THE HUMAN BODY

Organs-on-Chips, through specially designed microstructures in combination with specific tissues, allow the creation of an *in vitro* model that better resembles the basic units of human organs.

An Organ-on-Chip is generally described as a modular system with a central component, the cell culture, surrounded by several cues available to stimulate the cells (Fig. 2.1). These cues, can be of diverse nature: mechanical, chemical and biological, among others. For instance, as mechanical cues different types of microstructures or topographies are introduced to suply the cell culture the proper surface chemistry, arrangement or structural support [7, 8]. Moreover, the use of flexible substrates enables to introduce mechanical stretch, thus stimulating mechanically the entire cell microenvironment [9]. Chemical or nutrieuns are also accurately supplied through microchannels, providing the cells with biochemical agents at the right concentration [10]. With these microchannels, cues such as sheer stress, are also supplied through the accurate control of the flow. Such shear stress is highly dependent on geometrical parameters that can be tuned accordingly to offer the cell culture the right cues. This is done by controlling carefully the flow rate, pressure and fluid properties. In Figure 2.1, the types of cues more often reported in literature, are shown.

2.1.2. STATE-OF-THE-ART

The term "Organ-on-Chip" and the first demonstration of its potential advantages was introduced by scientists from Harvard University at the WYSS institute for Biological Inspired Engineering [11]. The basic structure of the first proof of concept is shown in Figure 2.2. This Organ-on-Chip device demonstrated for the first time the mimicking of the minimum unit of a human organ, in this case the alveolar-capillary interface of the lung (Fig. 2.2a), by using engineered microstructures. The device allowed the researchers to observe in real time and high resolution images, the inflammatory response the human body initiates when bacteria invade the respiratory vias.

In Figure 2.2b, the microengineered structure of the Lung-on-Chip is illustrated. It comprises four PDMS mould chambers, two of them interfaced trough a porous membrane of the same material, which create the mechanical support or substrate where endothelial and epithelial cells are cultured to replicate the alveolar epithelial and the microvasculature. This interface can be also stretched since the membrane is mechanically flexible, which allows stimulating the cells as it would happen in *in vivo* conditions. Such stretching is enabled by the two additional side chambers that can be externally and pneumatically actuated by establishing a pressure difference. Hence, the typical stretching of the lungs during breathing cycles is mimicked, along with the possibility

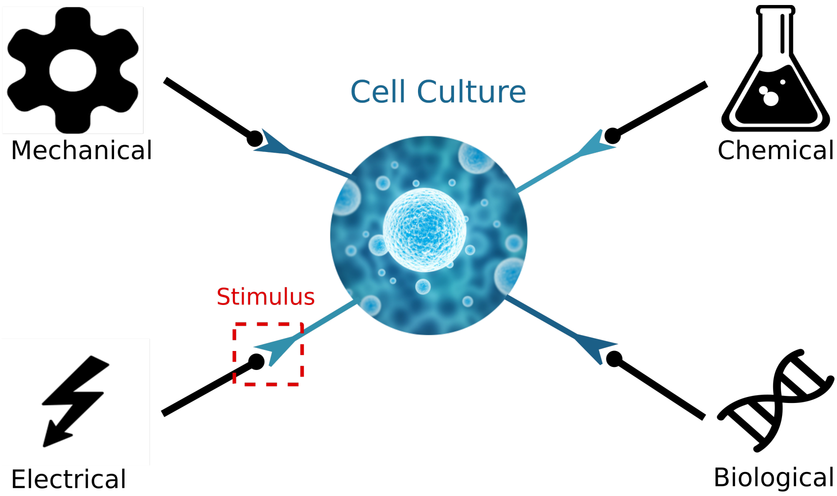

Figure 2.1: Organ-on-Chip concept: An illustration showing the the modular view of Organs-on-Chips comprising a central cell culture surrounded by the physical and chemical cues provided through microengineered structures to better resemble anatomy and physiological conditions.

of having two different type of cells interacting. Moreover, the two additional cavities, separated by the porous membrane, function as microfluidic channels through which air flow, nutrients and bacteria are introduced to simulate the microvasculature and to induce disease conditions.

Another examples of Organs-on-Chips found in literature is the Heart-on-Chip, which mimmics the basic units of the heart. In these devices, a cell culture of either human or animal cardiomyocytes and iPSCs [12–16], is stimulated using mainly mechanical and electrical cues [12–16].

In Figure 2.3, a few examples of Heart-on-Chip concepts are shown. As observed, a variety of cues have been implemented to provide cardiac cells with as close to *in vivo* environmental conditions as possible. To do so, specific suspended microstroctures such as flexible posts or cantilievers (Fig. 2.3a) [14, 15, 17, 18], and customized topographies (Fig. 2.3b) [8, 19] have been developed. Thus, cardiac cells can be aligned or provided with extracellular environments with mechanical properties closer to those of *in vivo* conditions.

Moreover, as seen in the Heart-on-Chip depicted in Fig. 2.4a [12], including microchannels enables to stimulate the cells chemically. This make possible to provide nutrients to the heart cells and emulate the microvasculature to approximate gradients of concentration of certain ions (Ca^+, Na^+), which is key in the contraction mechanisms of the cells [20–22]. On the other side, novel approaches such as the Cytostretch depicted in Figure 2.4b [16, 23], provide the possibility to include both mechanical and electrical cues simultaneously thorough electrodes integrated into the flexible PDMS substrate supporting a culture of iPSC derived cardiomyocytes. The microelectrodes offer an additional variable to either monitor the action potential of the cells or promote their contraction.

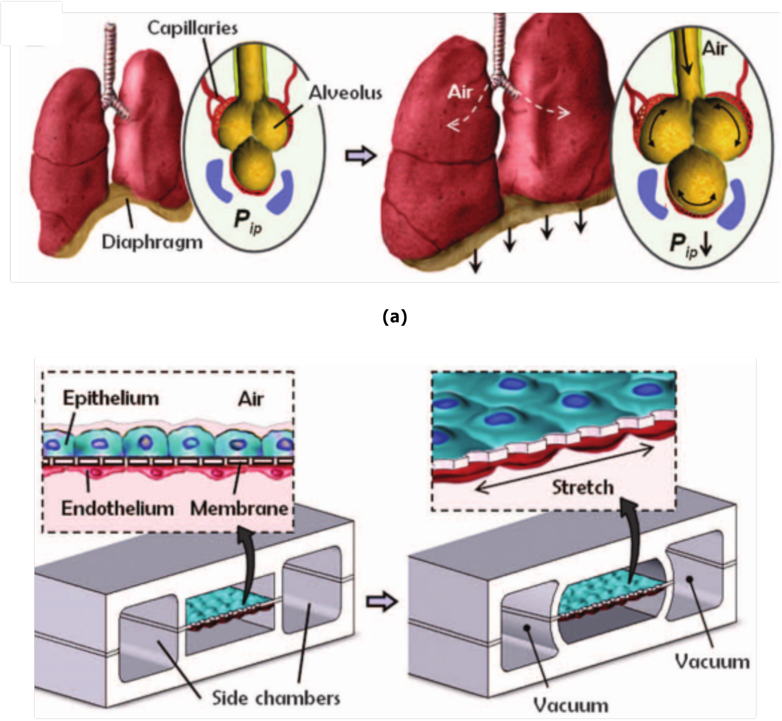

(a)

(b)

Figure 2.2: The first proof of concept of an Organ-on-Chip: The Lung-on-Chip developed at the Wyss Institute for Biological Inspired Engineering. **(a)** The alveolar-capillary interface of the human lung. **(b)** The structure of the microengineered Lung-on-Chip. Image reproduced with permission from [11].

Other devices that have been reported in literature such as gut-on-chip [24, 25], cancer-on-chip [26, 27] and vessel-on-chip [28, 29] are based mainly on microstructures that supply different cell lines with mechanical and biochemical cues such as shear stress controlled by the flow of culturing medium and pressure changes along customized microfluidic structures. As shown in Figure 2.5, such models are based on structures like microchannels, microchambers, valves and artificial interfaces (e.g. porous and non-porous membranes). The gut-on-chip model from Figure 2.5a [24], through microchannels developed in silicon, PDMS and special topography or structured walls, allows to closely replicate the size and alignment of tissues as found in *in vivo* conditions. The cancer-on-chip model (Fig. 2.5b) [27, 30], having two microchannels interfaced trough a porous membranes, permits to recreate the conditions under which cancer metastasis is more likely to happen, with cancer cells migrating through microvasculature to other tissues. The vessel-on-chip (Fig. 2.5c) exploits the highly controlled microstructures given by the microengineered channels with geometry closer to that of the cylindrical vessels in the human body. This gives the opportunity to create a model where the interaction between endothelial cells and blood cells under typical blood flow conditions can be studied [29].

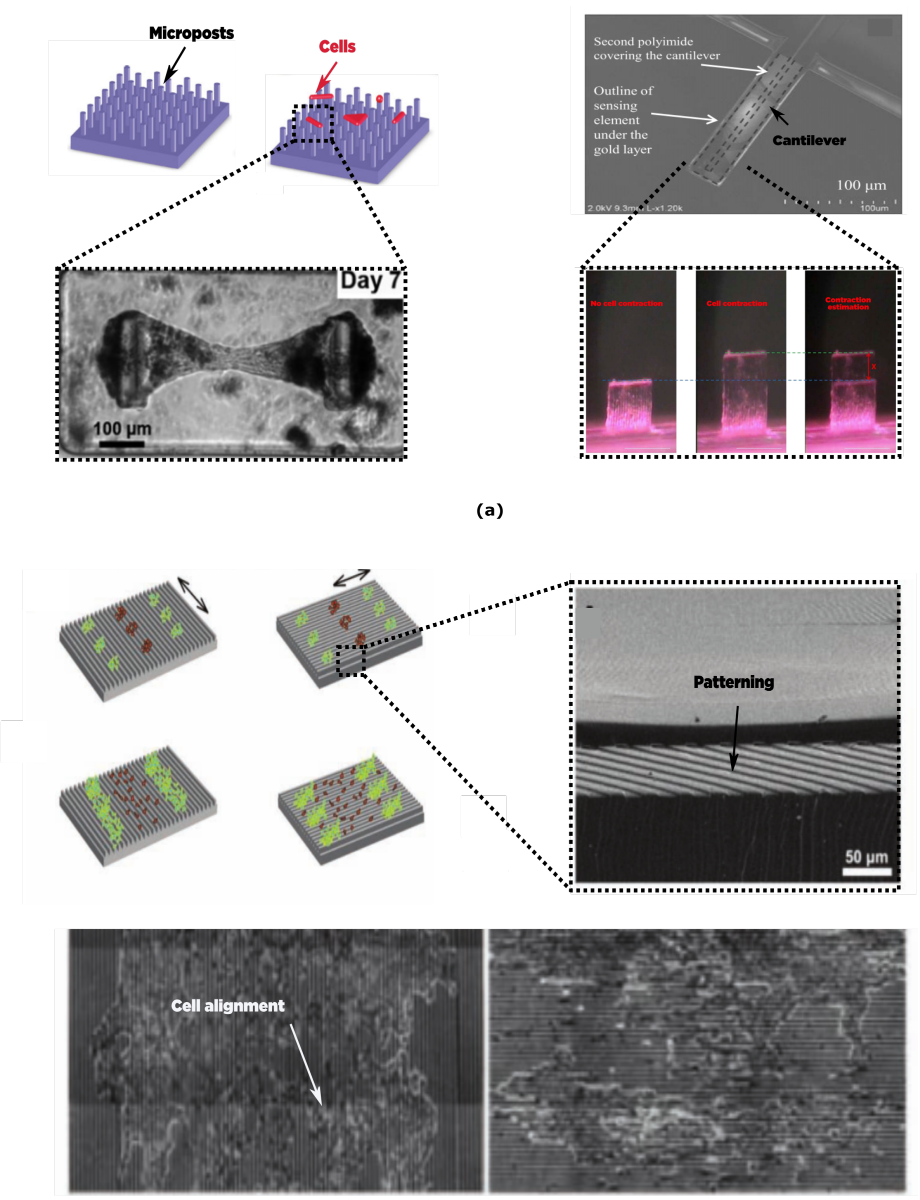

(a)

(b)

Figure 2.3: Examples of Heart-on-Chip devices found in literature and the diverse cues hearts cells can be exposed to be stimulated with closer to *in vivo* conditions. **(a)** Flexible microposts and cantilevers to anchor cardiac cells and evaluate cell contraction. **(b)** Microstructures with custom surface patterning for cell alignment. Images reproduced and adapted with permission from[8, 14, 15, 17–19].

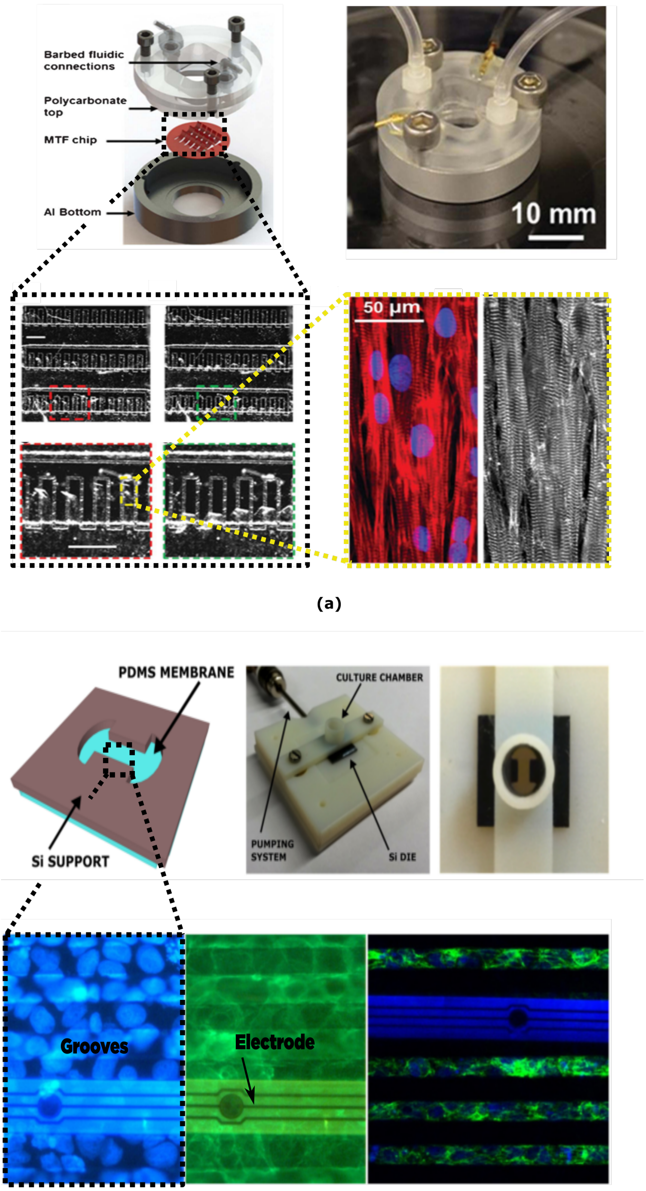

(a)

(b)

Figure 2.4: Examples of Heart-on-Chip devices found in literature and the diverse cues heart cells can be exposed to be stimulated in situations resembling *in vivo* conditions. **(a)** A heart-on-chip with microchannels to include chemical cues such as different ion concentrations and to administer drugs to evaluate efficacy. **(b)** Cytostretch: A microfabricated heart-on-chip based on a flexible PDMS membrane to provide stretching to iPSC derived cardiomyocytes, capable to evaluate their maturation and electrical activity. Images reproduced and adapted with permission from [12, 16, 20–23].

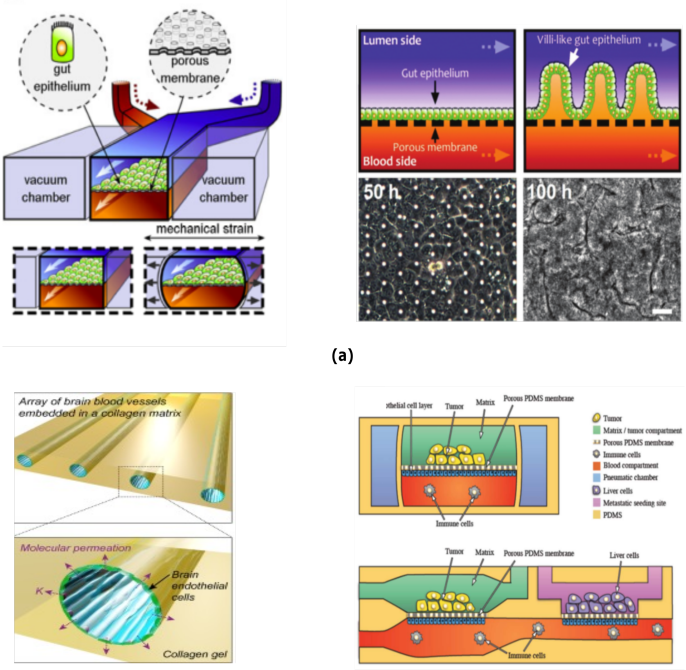

(a)

(b)

(c)

Figure 2.5: Examples of other relevant Organs-on-Chips models. **(a)** A schematic and optical images of the cell experiments of a gut-on-chip for studying drug absorption of compounds by the digestive system. **(b)** A schematic and image of a vessel-on-chip device closely replicating the cylindrical geometry of human microvasculature. **(c)** A schematic of a cancer-on-chip to model and study tumor metastasis. Images reproduced and adapted with permission from [24, 27–29].

Another Organs-on-Chips studied and developed in recent years is the brain-on-chip, namely brain tissue slices and the blood-brain barrier model (Fig. 2.6) [31]. The main goal of such models is to further understand the processes involved in specific units of the nervous system and in particular the electrical and biochemical activities of neurons and their relationship with the surrounding cell environment. Brain-on-chip proofs of concept recently reported [32–36], shown in Figure 2.6a, mainly aim at creating a model to understand the interaction and behaviour of animal brain slices with chemical or electrical signals. By developing microstructures that allow brain tissues to grow in a microenvironment resembling the skull and the surrounding microvasculature and by integrating electrodes that permit the detection and stimulation such tissues, it is possible to better understand the interactions of neurons with other cell types. The blood-brain barrier models are created to simulate the interface between neurons and the microvasculature dedicated to provide them nutrients and oxygen [37–41]. Such interface is often modelled through thin membrane-like microstructures suspended in a way that allows to have two or more different cell types cultured on either sides, making possible to study its barrier function towards external biological and chemical agents (Fig. 2.6b).

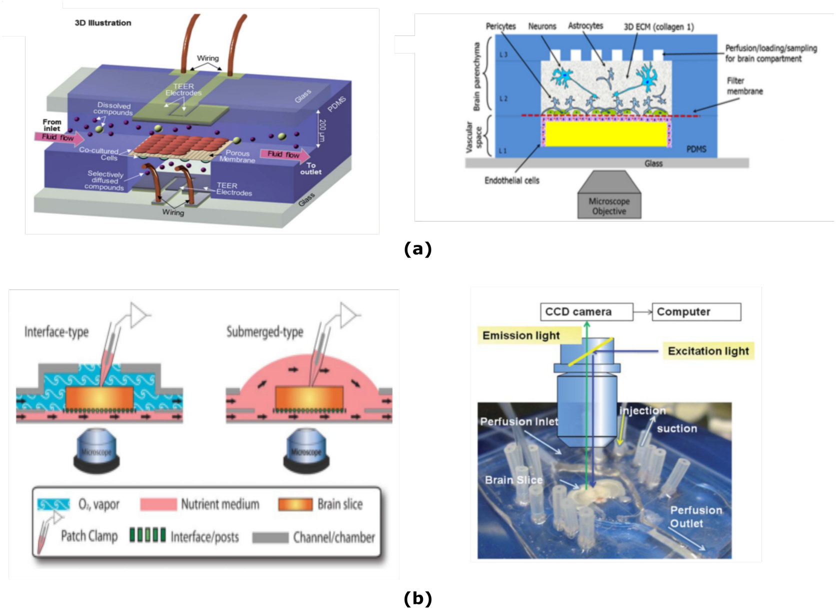

Figure 2.6: Organs-on-Chips specifically developed to study the behavior of brain cells. These, brain-on-chip models study: **(a)** the brain-blood barrier and **(b)** brain slice models to study and characterize the electrical cues from brain cells. Images reproduced and adapted with permission from [32, 34, 35, 38, 39, 42].

2.2. FABRICATION OF ORGANS-ON-CHIPS

From what reported above it is clear that microfluidics has played and plays a major role in OOC, practically enabling such type of devices. Microfluidics makes possible to handle accurately volumes of biological and chemical samples in the range of 100 nl to 100 μl, at low pressures (1Pa-10kPa) and under physiologically relevant flow conditions (1μl/min - 10 ml/min). In the past two decades the capability of manipulating single cells and performing chemical and biological analysys *in situ*, and classifying and mixing of different fluids in a single chip [43–45] has been widely demonstrated. Consequently, most of the practical implementation and development of numerous Organs-on-Chips so far has been possible due to the already available techniques in fabrication and characterizion of microfluidic systems and particularly Lab-on-Chips [45–47]. Most of the examples previously presented, depicted in Figures 2.2 to 2.6, were developed through fabrication processes based on soft-lithography or micromoulding techniques [9, 48].

2.2.1. SOFT-LITHOGRAPHY AND MICRO-MOULDING

The fabrication of Organs-on-Chips normally starts by creating a rigid mould of the desired three-dimensional (3D) microstructures that accurately replicate the organ anatomy. Very often such a rigid substrate is readily available, such as glass or silicon, and its structuring with the required features can be easily and accurately achieved using IC fabrication techniques such as photolithography, dry or wet etching and 3D printing. The features are very often developed either by patterning the silicon and other dielectric materials with conventional wet and dry etching [9, 48, 49] techniques or by using photoresists to realize high aspect ratio structures(e.g. SU8) [17, 50–52]. Once the mould is created, as most of these devices require high mechanical flexibility, a soft material such as an elastomer or thermoplastic is used as the base material for the final structure. This material is added into the mould and cured under very controlled environmental conditions (temperature, pressure, humidity). Once the polymeric material is fully cured, a replica of the negative of the mould is created, which corresponds to the microstructures resembling the organ anatomy. The cured material and final structure is quite often manually detached from the mould. This manual operation requires much care to avoid damaging the device critical features. In Figure 2.7, the main steps involved in the above mentioned fabrication processes are shown.

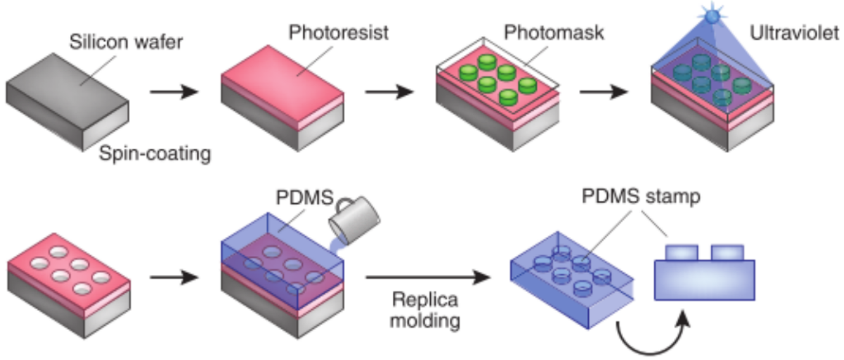

Figure 2.7: The main steps of a soft-lithography or replica moulding process to fabricate Organs-on-Chips. A mould with features replicating the human anatomy under study is created in a silicon wafer. The features are realized with conventional photo-lithography and dry or wet etching techniques. Then, a soft material, normally PDMS, is poured in the mould to create a negative replica that serves as another mould or as part of the final Organ-on-Chip. Images reproduced and adapted with permission from [9].

Fragile and high aspect-ratio microstructures that replicate human anatomy can be quickly developed with soft-lithography. Since the introduction of this technique as a method to realize 3D microstructures in PDMS, it has become the most accessible tool for biologists to create specialized miroenvironments to study cell processes. Most of the microstructures used for Organs-on-Chips reported in literature have relied on soft-lithograhy. As can be seen from few examples shown in Figure 2.8a-c (right column), 3D microstructures such as porous membranes, microchannels and microposts have been successfully developed with fabrication processes (left column) based on this technique. Soft-lithography has significantly contributed to the spreading of the Organ-on-Chip concept among biologists, giving them a tool to quickly create their customized cell culture microenviroments, the so-called rapid prototyping.

2.2.2. 3D-PRINTING

Recently, with the emergence of 3D-printing, many researchers have used this technique both to create moulds for soft-lithography or to directly print the desired structures [28, 53, 54] (Fig. 2.9a). With this technique, it is possible to fabricate macro and micro

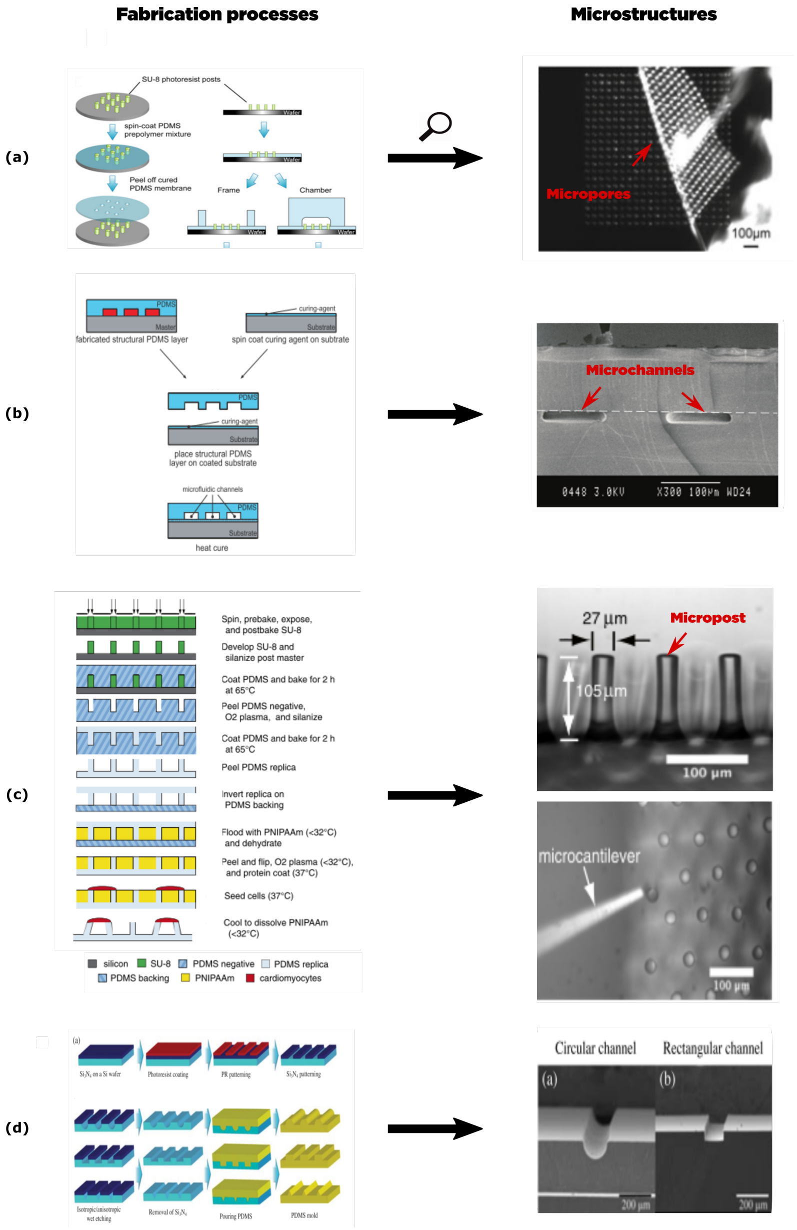

Figure 2.8: Examples of various 3D microstructures (*right*) created by using processes based on soft-lithography (*left*) applied to develop Organs-on-Chips. **(a)** Porous membranes for cell barrier modelling. **(b)** Microchannels for emulating microvasculature and create biochemical gradients. **(c)** Microposts developed for studying mechanical behaviour of heart and smooth muscle cells. **(d)** Different geometries of microchannels for mimicking and study micromusculature. Images reproduced and adapted with permission from [9, 17, 48–52].

scale structures with a variety of materials, inlcluding natural and synthetic biomaterials or combination of them. Structures mimmicking basic units of organs and anatomy such as microvasculature, skin and liver have been reported [55]. As can be seen in Figure 2.9b, cell constructs can be successfully and directly printed within PDMS-based microfluidic devices to develop Organs-on-Chips. Hydrogels and other materials serving as extracellular matrix have been also demonstrated, extending the capabilities on the control to replicate human anatomy [56, 57].

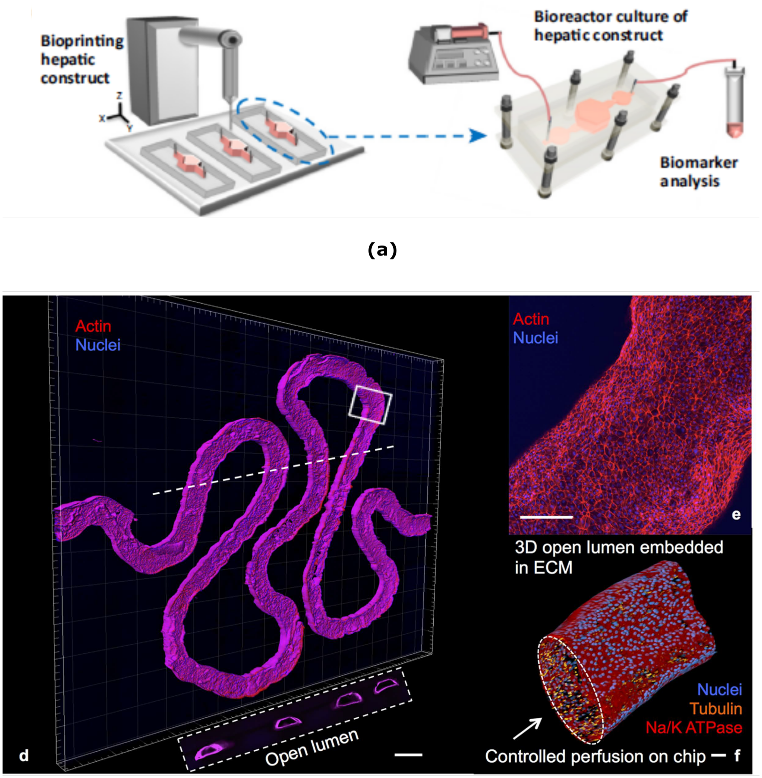

(a)

(b)

Figure 2.9: Some examples of 3D-printing for OOC. **(a)** Images of the procedure to print a 3D renal proximal tubule as an Organ-on-Chip. **(b)** Images showing the fabrication procedure and setup used for cell printing of hepatic spheroids encapsulated in GelMA, an hydrogel used for biomedical applications. Images reproduced and adapted with permission from [54, 56].

However, 3D-printing for OOC is still at an early stage. Further development is required for engineering suitable materials compatible with cell biology, but undoubtedly this technique has a high potential to improve the scalability of OOCs fabrication. Challenges so far known, such as biocompatibility issues of most materials used and their lack of resistance to common solvents used in cell culture (e.g. ethanol), need to be overcome to fully adopt this technique to fabricate OOCs.

2.3. CHARACTERIZATION TECHNIQUES

Organs-on-Chips are envisioned to fully exploit the capabilities and experience gained from recent breakthroughs in technology and cell biology. Generally, when assessing biological questions with OOC devices, the techniques used to acquire data concerning biochemical reaction, biological processes and state of the cells have relied on robust technologies. Optical transduction mechanisms have made available tools suitable to monitor and analyse the morphological and genetic characteristics of different cells and to closely observe complex cellular processes such as migration and differentiation, among others. Microscopy is a particular case of such available tools, with robust techniques such as florescence microscopy, confocal microscopy and two-photon excitation microscopy, which enable to observe biological processes with a high degree of specificity on the variables of interest and offer high resolution imaging.

Lately, more attention has been given to technological advances particularly in microtechnology that can contribute with alternatives in transduction mechanisms of physiological relevant data in cell microenvironments. Recent advances in bio-sensing and actuation present numerous opportunities to expand the number of variables to monitor and provide new mechanisms for creating structures to stimulate cell microenvironments.

A brief description of the most common techniques for data acquisition of relevant biological data in OOCs is here given, focusing mainly on the microscopy techniques used in the biological assessments reported in subsequent chapters of this thesis. Moreover, future techniques potentially enabled by the fabrication processes presented here, are also briefly introduced.

2.3.1. BRIGHT-FIELD AND FLORESCENCE MICROSCOPY

Optical microscopy is the most used technique to acquire data from *in vitro* cell experiments. In cell biology, the health state of cells is commonly assessed through microscopy by observing parameters such as cell size, shape and arrangement [58, 59]. For instance, based on the geometry and size it is possible to evaluate whether some cells or tissues are in healthy conditions based on the characteristics of the structures of the membrane and nuclei, which are readily observable with wavelengths within the visible spectrum. However, when more detailed information is required about cellular structures, the expression of certain genes or physiological processes, the so-called bright field microscopy is not enough. Limited contrast is provided when the size of the microstructures of interest go beyond the optical resolution, namely when aiming at observing molecular structures such as proteins and genes, which are in the range of few nanometres [60].

To circumvent the limitations of brightfield microscopy, flourescence microscopy is a better alternative. This advanced microscopy makes possible to observe cell mechanisms by including flourescent markers to the cell culture, called fluorephores or dyes, that bind to specific cell structures such as genes or proteins, making them visible at specific wavelengths other than the visible range [61]. By exciting the cells or sample of interest using a light source of specific wavelength and optical filters and specialized detectors, photons coming from the florescence of dyes bonded to biological structures of a sample are selectively detected, which renders visible the molecules of interest (Fig. 2.10a). The use of such specific dyes (e.g. lipids, DNA, protein, quantum dots) gives a high degree of selectivity and the capabilities of reaching the nuclei or trespass cellular membranes, given their submicrometer scale (Fig. 2.10b). There are many florescent labels reported in literature and commercially available depending on the molecules of interest to observe. Among them, coumarins, BODIPY dyes, flouresceins are examples of commonly used synthetic fluorescent dies [60, 62]. Among some of the commercially available dyes, Cell Tracker Orange and Green, VE-cadherin, phalloidin, and DAPI (4,6-diamidino-2-phenylindole), can be found. This procedure involving the introduction of the fluorescent dye and acquisition of data is commonly refereed in cell biology as cell staining.

Fluorescence microscopy is vastly used for characterizing cell behavior in Organs-on-Chips, enabling to investigate into aspects such as the formation of cell monolayers by observing biomarkers that characterize cell-to-cell communication and tissue formation [63]. Furthermore, this type of microscopy makes possible to study in detail every part of the cell, specifically the state and functioning of the nuclei and the cellular membrane. In Figure 2.10c-d, different examples of data acquired using both bright-field and fluorescence microscopy in Organs-on-Chips to assess biological experiments, are shown. The different colouring in red, blue and green of the image taken with a fluorescence microscope allows to distinguish the cell morphology, the size and state of the nuclei, the membrane quality and delimit the junction between the cells.

2.3.2. CONFOCAL MICROSCOPY

Complementary to fluorescence microscopy, confocal microscopy is also very often used in cell biology. It allows imaging with higher contrast for specifically selected focal planes. Thus, this type of microscopy allows to create 3D reconstructions using multiple 2D images taken at different distances along the depth of tissues and cells. Confocal microscopy also takes advantage of florescence with the difference that the photons emitted from the samples are purposely and selectively filtered back to avoid interference from regions which are not of particular interest to image [62]. Thus, photons coming from both out-of-focus planes and adjacent spots to the focus point are filtered out, giving a sharper image only of the plane of focus of interest (Fig.2.11a).

For instance, this technique is very useful to understand the mechanisms that involve migration of cells or bacteria through tissues or multiple cell layers (e.g. endothelial/epithelial, vessel/organ) to model the behavior of specific diseases, present in organs such as the lung, the brain and the gut [46, 66, 67].

2.3.3. MICROELECTRONICS AND MEMS

Over the last decade, microelectronics and micro-electromechanical systems (MEMS) have made possible to develop very accurate high speed sensing and stimulating microstructures to better understand cell processes, and thus providing accessible tools to biologists to acquire more relevant data from cell cultures.

Through customized microstructures, capable to selectively detect specific molecules or supply controlled electric currents, it is possible to obtain information such as quality of the cellular membrane, the electrical action potential and assess quantitatively the rigidity and water content, among other parameters characteristic of various cell types [68, 69]. Devices such as microelectrode arrays are a good example of microtechnolo-

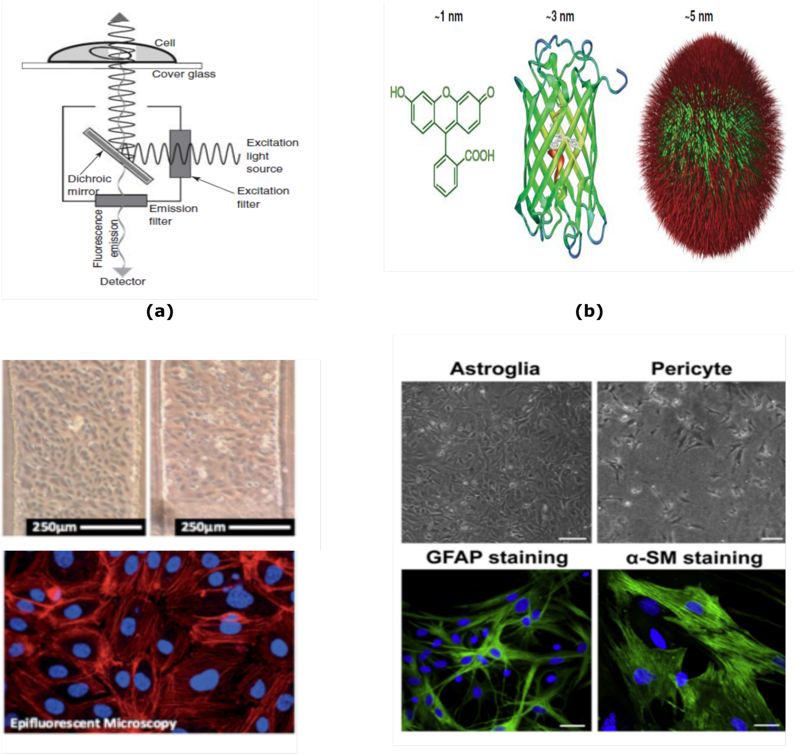

(a) (b)

(c) (d)

Figure 2.10: Florescence microscopy. **(a)** A schematic view of the basic structure of a florescent microscope. Florescence on a modified biological sample is induced by an excitation light and detected back to form an image. **(b)** Typical structure of the molecules and nano-particles used as flourephores or dye. **(c)** Image of an endothelial cell in an Organ-on-Chip taken with both bright field and florescence microscopy. **(d)** Image of Astrogial and Pericites cultured in an Organ-on-Chip taken with both bright field and florescence microscopy. Images reproduced and adapted with permission from [46, 53, 62, 64].

gies commonly used in biology to investigate cell mechanisms. These electrodes are employed to either monitor or stimulate specific cells that exhibit electrical activity (e.g neurons, cardiomyocytes). Figure 2.12a shows a microelectrode array meant to monitor the action potential of cardiomyocites when subjected to chemical stimulation with drug compounds [16, 23, 70].

Another example of such type of structures recently implemented in Organs-on-Chips are electrodes to characterize the quality of growth of tissues or cell monolayers. Vastly used to assess the quality of endothelial cells layers, two or several electrodes measure the electrical resistance between the opposite sides of the cell or tissue layer under study [68]. The electrical resistance measured between such electrodes can be correlated with the condition of the layer. This technique is often referred as transendothelial electrical resistance (TEER) and gives accurate information specifically regarding the quality of the junction between cells. In Figure 2.12b two examples of OOC devices with microstructures for TEER measurements, are shown [39, 68].

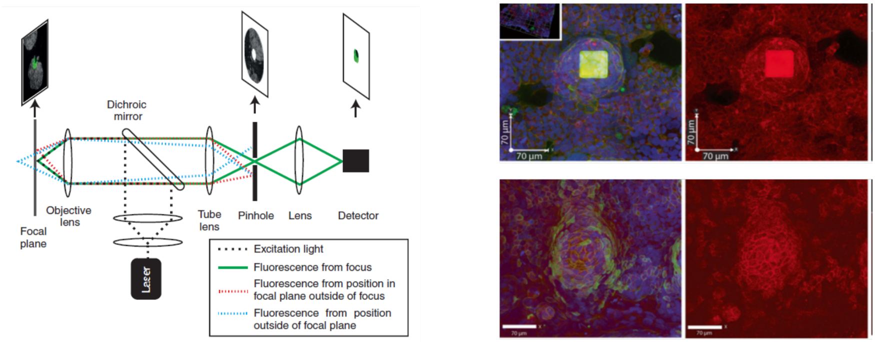

(a) **(b)**

Figure 2.11: Confocal microscopy: A complementary technique to florescent microscopy for higher contrast imaging and 3D reconstructions through 2D image stacking. **(a)** A schematic drawing of the basic structure of a confocal microscope. **(b)** Confocal images taken to investigate gastrointestical epithelial cells cultured on a porous polymer membrane of an Organ-on-Chip. Images reproduced and adapted with permission from [62, 65].

Other examples of electrical measurements are the many Lab-on-Chips devices found in literature, which are capable of dividing, classifying, counting cells, assess the mechanical properties and manipulate cells individually [71]. Moreover, other electrical driven microstructures have been developed to enhance or initiate specific chemical reactions.

2.4. CELL CULTURE IN ORGANS-ON-CHIPS

The accurately defined microstructures in Organ-on-Chip devices not only have to ensure high resemblance of human physiology and anatomy but also create the conditions required in the microenvironment for the cells to grow. This is another important aspect to consider when developing these devices. Once the microenvironment is fabricated, numerous cell types need to be cultured to study the specific biological mechanisms or diseases of interest.

Under *in vivo* conditions cells are surrounded by a web-like structure of molecules, called extracellular matrix (ECM) that provide them with the necessary mechanical and biochemical support (Fig. 2.13a) [72]. The cells in charge of synthesize such complex molecules are the fibroblasts. The extracellular matrix also enables mechanisms that cells use to communicate with the surrounding and support cell division and further specialization processes. Depending on the type of the tissue to form, the composition and structures of the extracellular matrix changes. Thus, recreating such components is an indispensable task when culturing cells *in vitro* and specifically in Organs-on-Chips to make sure the biological assessments are carried out with reliable cells and tissues.

When culturing cells such as endothelial, epithelial, cardiac and cancer cells, it is necessary to provide the ECM and guarantee that the surface chemistry of the material is suitable for the cross-interaction, adhesion and growth of the cells. Very often this is done through a *functionalization* of the surface of the microstructures with high water content substances such as matrigel, collagen or fibronectin [9, 28, 39, 73, 74], which

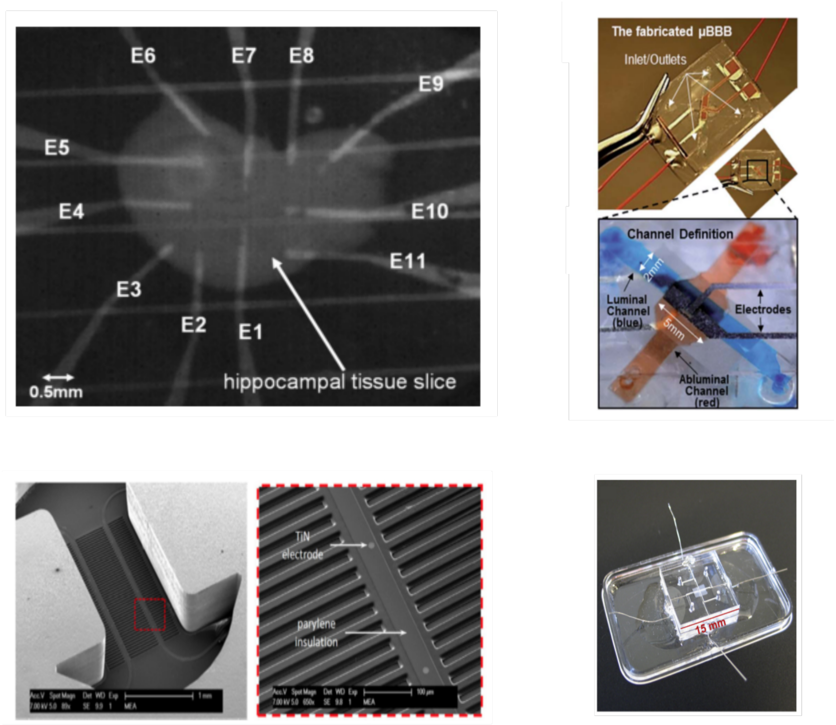

(a) **(b)**

Figure 2.12: Microelectronic and MEMS devices developed for monitoring and stimulation of the cell microenvironment in Organs-on-Chips. **(a)** Example of microelectrode arrays developed for monitoring the action potential of cardiac cells in a rigid substrate (*top*) and in a flexible membrane (*bottom*). **(b)** An Organ-on-Chip with integrated microelectrodes for TEER measurements (*top*) and an adapted PDMS-cased Organ-on-Chip (*bottom*) to include metal electrodes for TEER measurements. Images reproduced and adapted with permission from [16, 23, 68, 70].

properly recreate the ECM. However, in most Organ-on-Chips, there is not a sufficient adhesion between the ECM and the structural material and additional treatment of the microstructures is necessary prior to *funcionalization*. The surface of structures such as microchannels and microposts need to be treated first, as coating such structure with water based solutions might be more difficult due to capillary forces and hydrophobicity of the material, impeding a subsequent conformal coating and uniform cell monolayers. As most Organs-on-Chips are based on polymeric materials such as PDMS or parylene, prior any cell experimentation, these devices require surface treatment to render the surfaces hydrophilic to enable the further *functionalization*. Such treatment is often done either exposing the devices to oxygen plasma or adding chemical agents [75, 76].

Moreover, the growth and viability of a cell or tissue culture depends strongly on the nutrients supplied through the culture medium and the environmental conditions. Very often, molecules and nutrients are supplied to the cell by including so-called growth factors in the medium, which guarantees the right conditions for completing the cellular

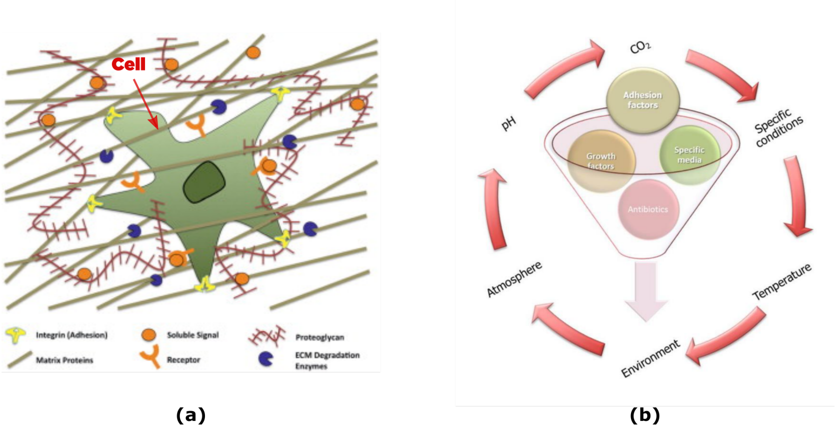

(a) (b)

Figure 2.13: Basic concepts of cell culture. **(a)** The extracellular matrix concept required for mechanical support and cross-interaction. **(b)** Main variables or environmental conditions to be controlled for having viable cell cultures. Images reproduced and adapted with permission from [72, 77].

cycles [77, 78]. Thus, the selection of the right type of medium used is key when culturing different type of cells. Environmental conditions such as pH, temperature, oxygen and carbon dioxide concentration are highly relevant as they are complementary cues that influence cell growth (Fig. 2.13b). Hence, cell culturing is often done in controlled environments or incubators with regulated temperature (37 °C) typical of the human body and a humid environment with physiological carbon dioxide and oxygen concentrations, namely $[CO_2] = 5\%$ and $[O_2] = 20\%$ [79, 80]. In Figure 2.13b, the main variables influencing cell culture are summarized.

2.5. FUTURE CHALLENGES

Organs-on-Chips allow to create cell culture microenvironments that make possible to gather additional and specialized data on cell mechanisms and diseases unavailable when using typical conventional static cell culture. The better understanding of complex cell mechanisms through these devices have been focusing on two interrelated applications: disease models and enhanced *in vitro* screening. In disease modelling, the representation of a specific disease can be created with diverse cell types representative of the basic units of the organ of interest. For instance, in diseases known to affect or manifest trough issues in the interface between different tissues, a proper disease model would consist of microstructures such as porous membrane dividing two different cell cultures wherein it is possible to introduce pathogens, proteins or compounds that might interfere with the proper functioning of such minimal unit. This could refer, for example, to the minimal unit of the lung presented in Figure 2.2 [9] or the blood-brain barrier from Figure 2.6a [38, 39].

In vitro essays could now implement such disease models, having the closest model to the human body in an *in vitro* culture flask, to evaluate the impact certain compounds have on the cell microenvironment, and the suspected adverse or therapeutic effects. However, as highlighted in the previous chapter, the current available devices still lack of certain characteristics and proper cross validation with data collected in clinical essays in order to be established as a robust tool and to be routinely used in pharmaceutical industry. As highlighted in section 2.2, the fabrication methods for most of these devices are hardly adaptable scalable fabrication processes for *in vitro* screening application in drug development. The fabrication processes rely strongly on manual techniques since they were originally developed for rapid prototyping in cell biology research. This manual techniques not only intrinsically limit the features that can be developed, but also are not cost-effective. Few more steps need to be taken to adapt the fabrication processes of Organs-on-Chips to align them with high scale manufacturing and to increase their applicability and validity for drug development.

Recently, efforts towards the use of mature and well known fabrication techniques in the development Organs-on-Chips have been undertaken. Specifically, the possibility of using IC and MEMS microfabrication techniques in developing these devices, has been addressed. Moreover, utilizing IC and MEMS based techniques, the already developed Organs-on-Chips can be complemented with the integration of sensors and actuators, a much needed next step. Bringing fabrication of Organs-on-Chips closer to such well known techniques will allow to have a manufacturable and cost-effective production to implement them as the alternative to in*in vitro* screening essays. The following chapters present several efforts made to address and circumvent some of the issues of soft-lithography for fabrication of Organs-on-Chips. Alternative fabrication processes employing IC and MEMS fabrication techniques, are proposed. Moreover, the fabrication processes are designed to enable the interfacing of existing and novel Organs-on-Chips with microstructures for sensing and actuation.

REFERENCES

[1] N. S. Bhise, J. Ribas, V. Manoharan, Y. S. Zhang, A. Polini, S. Massa, M. R. Dokmeci, and A. Khademhosseini, *Organ-on-a-chip platforms for studying drug delivery systems.* Journal of controlled release : official journal of the Controlled Release Society (2014), 10.1016/j.jconrel.2014.05.004.

[2] F. Lautenschläger and M. Piel, *Microfabricated devices for cell biology: all for one and one for all.* Current opinion in cell biology **25**, 116 (2013).

[3] a. K. Capulli, K. Tian, N. Mehandru, a. Bukhta, S. F. Choudhury, M. Suchyta, and K. K. Parker, *Approaching the in vitro clinical trial: engineering organs on chips.* Lab on a chip **14**, 3181 (2014).

[4] S. Selimović, M. R. Dokmeci, and A. Khademhosseini, *Organs-on-a-chip for drug discovery.* Current opinion in pharmacology **13**, 829 (2013).

[5] C. Y. Chan, P.-H. Huang, F. Guo, X. Ding, V. Kapur, J. D. Mai, P. K. Yuen, and T. J. Huang, *Accelerating drug discovery via organs-on-chips.* Lab on a chip **13**, 4697 (2013).

[6] M. B. Esch, T. L. King, and M. L. Shuler, *The role of body-on-a-chip devices in drug and toxicity studies.* Annual review of biomedical engineering **13**, 55 (2011).

[7] M. N. De Silva, R. Desai, and D. J. Odde, *Micro-patterning of animal cells on PDMS substrates in the presence of serum without use of adhesion inhibitors,* Biomedical Microdevices **6**, 219 (2004).

[8] B. Yuan, Y. Li, D. Wang, Y. Xie, Y. Liu, L. Cui, F. Tu, H. Li, H. Ji, W. Zhang, and X. Jiang, *A general approach for patterning multiple types of cells using holey PDMS membranes and microfluidic channels,* Advanced Functional Materials **20**, 3715 (2010).

[9] D. Huh, H. J. Kim, J. P. Fraser, D. E. Shea, M. Khan, A. Bahinski, G. a. Hamilton, and D. E. Ingber, *Microfabrication of human organs-on-chips.* Nature protocols **8**, 2135 (2013).

[10] S. Halldórsson, E. Lucumi, R. Gómez-Sjöberg, and R. M. Fleming, *Advantages and challenges of microfluidic cell culture in polydimethylsiloxane devices,* Biosensors and Bioelectronics **63**, 218 (2014).

[11] I. D. Huh D, Matthews B, Mammoto A, Montoya-Zavala M, Hsin H, *Reconstituting Organ-Level Lung,* Science **328**, 1662 (2010).

[12] A. Agarwal, J. A. Goss, A. Cho, M. L. McCain, and K. K. Parker, *Microfluidic heart on a chip for higher throughput pharmacological studies.* Lab on a chip **13**, 3599 (2013).

[13] A. Kobuszewska, E. Tomecka, K. Zukowski, E. Jastrzebska, M. Chudy, A. Dybko, P. Renaud, and Z. Brzozka, *Heart-on-a-Chip: An Investigation of the Influence of Static and Perfusion Conditions on Cardiac (H9C2) Cell Proliferation, Morphology, and Alignment,* SLAS Technology **22**, 536 (2017).

[14] A. Gaitas, R. Malhotra, T. Li, T. Herron, and J. Jalife, *A device for rapid and quantitative measurement of cardiac myocyte contractility,* Review of Scientific Instruments **86** (2015), 10.1063/1.4915500.

[15] T. Boudou, W. R. Legant, A. Mu, M. a. Borochin, N. Thavandiran, M. Radisic, P. W. Zandstra, J. a. Epstein, K. B. Margulies, and C. S. Chen, *A Microfabricated Platform to Measure and Manipulate the Mechanics of Engineered Cardiac Microtissues,* Tissue Engineering Part A **18**, 910 (2012).

[16] N. Gaio, B. V. Meer, W. Q. Solano, L. Bergers, A. V. D. Stolpe, C. Mummery, P. M. Sarro, and R. Dekker, *Cytostretch , an Organ-on-Chip Platform,* Journal of Micromachines , 1 (2016).

[17] R. E. Taylor, K. Kim, N. Sun, S. J. Park, J. Y. Sim, G. Fajardo, D. Bernstein, J. C. Wu, and B. L. Pruitt, *Sacrificial layer technique for axial force post assay of immature cardiomyocytes,* Biomedical Microdevices **15**, 171 (2013).

[18] J. You, H. Moon, B. Y. Lee, J. Y. Jin, Z. E. Chang, S. Y. Kim, J. Park, Y. S. Hwang, and J. Kim, *Cardiomyocyte sensor responsive to changes in physical and chemical environments,* Journal of Biomechanics **47**, 400 (2014).

[19] A. W. Feinberg, P. W. Alford, H. Jin, C. M. Ripplinger, A. a. Werdich, S. P. Sheehy, A. Grosberg, and K. K. Parker, *Controlling the contractile strength of engineered cardiac muscle by hierarchal tissue architecture,* Biomaterials **33**, 5732 (2012).

[20] A. Sirker and A. M. Shah, *Biochemistry and physiology of cardiac muscle,* Medicine **38**, 340 (2010).

[21] G. a. Peeters, V. Hlady, J. H. Bridge, and W. H. Barry, *Simultaneous measurement of calcium transients and motion in cultured heart cells.* The American journal of physiology **253**, H1400 (1987).

[22] K. S. McDonald, *The interdependence of Ca2+ activation, sarcomere length, and power output in the heart.* Pflugers Archiv : European journal of physiology **462**, 61 (2011).

[23] S. Khoshfetrat Pakazad, a. Savov, a. van de Stolpe, and R. Dekker, *A novel stretchable micro-electrode array (SMEA) design for directional stretching of cells,* Journal of Micromechanics and Microengineering **24**, 034003 (2014).

[24] H. J. Kim and D. E. Ingber, *Gut-on-a-Chip microenvironment induces human intestinal cells to undergo villus differentiation.* Integrative biology : quantitative biosciences from nano to macro **5**, 1130 (2013).

[25] S. N. Bhatia and D. E. Ingber, *Microfluidic organs-on-chips.* Nature biotechnology **32**, 760 (2014).

[26] X. Ren, D. Levin, and F. Lin, *Cell migration research based on organ-on-chip-related approaches,* Micromachines **8** (2017), 10.3390/mi8110324.

[27] A. van de Stolpe and J. den Toonder, *Workshop meeting report Organs-on-Chips: human disease models.* Lab on a chip **13**, 3449 (2013).

[28] J. A. Kim, H. N. Kim, S. K. Im, S. Chung, J. Y. Kang, and N. Choi, *Collagen-based brain microvasculature model in vitro using three-dimensional printed template,* Biomicrofluidics **9** (2015), 10.1063/1.4917508.

[29] H. Lee, M. Chung, and N. L. Jeon, *Microvasculature: An essential component for organ-on-chip systems,* MRS Bulletin **39**, 51 (2014).

[30] J. den Toonder, *Circulating tumor cells: the Grand Challenge,* Lab on a Chip **11**, 375 (2011).

[31] M. W. van der Helm, A. D. van der Meer, J. C. Eijkel, A. van den Berg, and L. I. Segerink, *Microfluidic organ-on-chip technology for blood-brain barrier research,* Tissue Barriers **4** (2016), 10.1080/21688370.2016.1142493.

[32] Y. T. Tang, J. Kim, H. E. López-Valdés, K. C. Brennan, and Y. S. Ju, *Development and characterization of a microfluidic chamber incorporating fluid ports with active suction for localized chemical stimulation of brain slices,* Lab on a Chip **11**, 2247 (2011).

[33] A. Queval, N. R. Ghattamaneni, C. M. Perrault, R. Gill, M. Mirzaei, R. A. McKinney, and D. Juncker, *Chamber and microfluidic probe for microperfusion of organotypic brain slices,* Lab Chip **10**, 326 (2010).

[34] Y. Huang, J. C. Williams, and S. M. Johnson, *Brain slice on a chip: opportunities and challenges of applying microfluidic technology to intact tissues,* Lab on a Chip **12**, 2103 (2012).

[35] W. E. Svendsen, F. A. Al Atraktchi, T. Bakmand, H. Waagepetersen, and M. Dimaki, *Novel culturing platform for brain slices and neuronal cells,* Proceedings of the Annual International Conference of the IEEE Engineering in Medicine and Biology Society, EMBS **2015-Novem**, 346 (2015).

[36] A. J. Blake, T. M. Pearce, N. S. Rao, S. M. Johnson, and J. C. Williams, *Multilayer PDMS microfluidic chamber for controlling brain slice microenvironment,* Lab on a Chip **7**, 842 (2007), arXiv:NIHMS150003 .

[37] B. Prabhakarpandian, M.-C. Shen, J. B. Nichols, I. R. Mills, M. Sidoryk-Wegrzynowicz, M. Aschner, and K. Pant, *SyM-BBB: a microfluidic blood brain barrier model,* Lab on a Chip **13**, 1093 (2013).

[38] L. M. Griep, F. Wolbers, B. De Wagenaar, P. M. Ter Braak, B. B. Weksler, I. A. Romero, P. O. Couraud, I. Vermes, A. D. Van Der Meer, and A. Van Den Berg, *BBB on CHIP: Microfluidic platform to mechanically and biochemically modulate blood-brain barrier function,* Biomedical Microdevices **15**, 145 (2013).

[39] R. Booth and H. Kim, *Characterization of a microfluidic in vitro model of the blood-brain barrier (μBBB),* Lab on a Chip **12**, 1784 (2012).

[40] H. Cho, J. H. Seo, K. H. K. Wong, Y. Terasaki, J. Park, K. Bong, K. Arai, E. H. Lo, and D. Irimia, *Three-Dimensional Blood-Brain Barrier Model for in vitro Studies of Neurovascular Pathology,* Scientific Reports **5**, 15222 (2015).

[41] A. K. H. Achyuta, A. J. Conway, R. B. Crouse, E. C. Bannister, R. N. Lee, C. P. Katnik, A. A. Behensky, J. Cuevas, and S. S. Sundaram, *A modular approach to create a neurovascular unit-on-a-chip,* Lab Chip **13**, 542 (2013).

[42] J. A. Brown, V. Pensabene, D. A. Markov, V. Allwardt, M. Diana Neely, M. Shi, C. M. Britt, O. S. Hoilett, Q. Yang, B. M. Brewer, P. C. Samson, L. J. McCawley, J. M. May, D. J. Webb, D. Li, A. B. Bowman, R. S. Reiserer, and J. P. Wikswo, *Recreating blood-brain barrier physiology and structure on chip: A novel neurovascular microfluidic bioreactor,* Biomicrofluidics **9** (2015), 10.1063/1.4934713.

[43] X. Mu, W. Zheng, J. Sun, W. Zhang, and X. Jiang, *Microfluidics for manipulating cells.* Small (Weinheim an der Bergstrasse, Germany) **9**, 9 (2013).

[44] K. Ren, J. Zhou, and H. Wu, *Materials for microfluidic chip fabrication.* Accounts of chemical research **46**, 2396 (2013).

[45] G. T. Vladisavljević, N. Khalid, M. a. Neves, T. Kuroiwa, M. Nakajima, K. Uemura, S. Ichikawa, and I. Kobayashi, *Industrial lab-on-a-chip: design, applications and scale-up for drug discovery and delivery.* Advanced drug delivery reviews **65**, 1626 (2013).

[46] F. R. Walter, S. Valkai, A. Kincses, A. Petneházi, T. Czeller, S. Veszelka, P. Ormos, M. A. Deli, and A. Dér, *A versatile lab-on-a-chip tool for modeling biological barriers,* Sensors and Actuators, B: Chemical **222**, 1209 (2016).

[47] D. Kim, X. Wu, A. T. Young, and C. L. Haynes, *Micro fl uidics-Based in Vivo Mimetic Systems for the Study of Cellular Biology,* ACS, American Chemical Society (2015).

[48] Y. Xia and G. M. Whitesides, *Soft lithography,* Annual Review of Material science **28**, 153 (1998), arXiv:1111.6189v1 .

[49] J. S. Choi, Y. Piao, and T. S. Seo, *Fabrication of various cross-sectional shaped polymer microchannels by a simple PDMS mold based stamping method,* Biochip Journal **6**, 240 (2012).

[50] B. H. Jo, L. M. Van Lerberghe, K. M. Motsegood, and D. J. Beebe, *Three-dimensional micro-channel fabrication in polydimethylsiloxane (PDMS) elastomer,* Journal of Microelectromechanical Systems **9**, 76 (2000).

[51] T. Fujii, *PDMS-based microfluidic devices for biomedical applications,* Microelectronic Engineering **61-62**, 907 (2002).

[52] Y. Hongbin, Z. Guangya, C. F. Siong, W. Shouhua, and L. Feiwen, *Novel polydimethylsiloxane (PDMS) based microchannel fabrication method for lab-on-a-chip application,* Sensors and Actuators, B: Chemical **137**, 754 (2009).

[53] C. Szydzik, B. Niego, G. Dalzell, M. Knoerzer, F. Ball, W. S. Nesbitt, R. Medcalf, K. Khoshmanesh, and A. Mitchell, *Fabrication of complex PDMS microfluidic structures and embedded functional substrates by one-step injection moulding,* RSC Adv. **6**, 87988 (2016).

[54] K. A. Homan, D. B. Kolesky, M. A. Skylar-Scott, J. Herrmann, H. Obuobi, A. Moisan, and J. A. Lewis, *Bioprinting of 3D Convoluted Renal Proximal Tubules on Perfusable Chips,* Scientific Reports **6**, 1 (2016).

[55] H.-G. Yi, H. Lee, and D.-W. Cho, *3D Printing of Organs-On-Chips,* Bioengineering **4**, 10 (2017).

[56] S. Knowlton, B. Yenilmez, and S. Tasoglu, *Towards Single-Step Biofabrication of Organs on a Chip via 3D Printing,* Trends in Biotechnology **34**, 685 (2016).

[57] K. Gold, A. K. Gaharwar, and A. Jain, *Emerging trends in multiscale modeling of vascular pathophysiology: Organ-on-a-chip and 3D printing,* Biomaterials (2018), 10.1016/j.biomaterials.2018.07.029.

[58] D. J. Stephens and V. J. Allan, *Light Microscopy Techniques for Live Cell Imaging,* Biological Imaging **82**, 82 (2003).

[59] M. M. Frigault, J. Lacoste, J. L. Swift, and C. M. Brown, *Live-cell microscopy - tips and tools,* Journal of Cell Science **122**, 753 (2009).

[60] O. Wolfbeis, ed., *Fluorescence Spectroscopy in Biology: Advanced Methods and their Applications to Membranes, Proteins, DNA, and Cells (Springer Series on Fluorescence) (v. 3)* (Springer, 2005).

[61] M. J. Sanderson, I. Smith, I. Parker, and M. D. Bootman, *Flourescence Microscopy,* Cold Spring Harb Protocol **2014**, 36 (2016).

[62] U. Kubitscheck, ed., *Fluorescence Microscopy: From Principles to Biological Applications* (Wiley-Blackwell, 2017).

[63] J. S. H. Danial, Y. Aguib, and M. H. Yacoub, *Advanced fluorescence microscopy techniques for the life sciences.* Global cardiology science & practice **2016**, e201616 (2016).

[64] H. Cho, J. H. Seo, K. H. K. Wong, Y. Terasaki, J. Park, K. Bong, K. Arai, E. H. Lo, and D. Irimia, *Three-Dimensional Blood-Brain Barrier Model for in vitro Studies of Neurovascular Pathology,* Scientific Reports **5**, 15222 (2015).

[65] M. B. Esch, J. Yang, C. Yu, J. Yu, J. C. March, and M. L. Shuler, *On chip porous polymer membranes for integration of gastrointestinal tract epithelium with microfluidic ... On chip porous polymer membranes for integration of gastrointestinal tract epithelium with microfluidic,* Biomedical Microdevices (2015), 10.1007/s10544-012-9669-0.

[66] P. Caspers and G. Lucassen, *Automated depth-scanning confocal Raman microspectrometer for rapid in vivo determination of water concentration profiles in human skin,* Journal of Raman … **818**, 813 (2000).

[67] D. Felekis, H. Vogler, G. Mecja, S. Muntwyler, M. S. Sakar, U. Grossniklaus, and B. J. Nelson, *High-throughput analysis of the morphology and mechanics of tip growing cells using a microrobotic platform,* 2014 IEEE/RSJ International Conference on Intelligent Robots and Systems , 3955 (2014).

[68] P. Ertl, D. Sticker, V. Charwat, C. Kasper, and G. Lepperdinger, *Lab-on-a-chip technologies for stem cell analysis.* Trends in biotechnology **32**, 245 (2014).

[69] Y. Yi, J. Park, J. Lim, C. J. Lee, and S.-H. Lee, *Central Nervous System and its Disease Models on a Chip,* Trends in Biotechnology **33**, 762 (2015).

[70] O. Graudejus, Z. Yu, J. Jones, B. Morrison, and S. Wagner, *Characterization of an Elastically Stretchable Microelectrode Array and Its Application to Neural Field Potential Recordings,* Journal of The Electrochemical Society **156**, P85 (2009).

[71] Y. Ghallab and Y. Ismail, *CMOS Based Lab-on-a-Chip: Applications, Challenges and Future Trends,* Circuits and Systems Magazine, IEEE , 27 (2014).

[72] A. D. Theocharis, S. S. Skandalis, C. Gialeli, and N. K. Karamanos, *Extracellular matrix structure,* Advanced Drug Delivery Reviews **97**, 4 (2016).

[73] A. Herland, A. D. Van Der Meer, E. A. FitzGerald, T. E. Park, J. J. Sleeboom, and D. E. Ingber, *Distinct contributions of astrocytes and pericytes to neuroinflammation identified in a 3D human blood-brain barrier on a chip,* PLoS ONE **11**, 1 (2016).

[74] D. Huh, Y.-s. Torisawa, G. a. Hamilton, H. J. Kim, and D. E. Ingber, *Microengineered physiological biomimicry: organs-on-chips.* Lab on a chip **12**, 2156 (2012).

[75] J. D. Wang, E. S. Khafagy, K. Khanafer, S. Takayama, and M. E. Elsayed, *Organization of Endothelial Cells, Pericytes, and Astrocytes into a 3D Microfluidic in Vitro Model of the Blood-Brain Barrier,* Molecular Pharmaceutics **13**, 895 (2016).

[76] A. Herland, A. D. Van Der Meer, E. A. FitzGerald, T. E. Park, J. J. Sleeboom, and D. E. Ingber, *Distinct contributions of astrocytes and pericytes to neuroinflammation identified in a 3D human blood-brain barrier on a chip,* PLoS ONE **11**, 1 (2016).

[77] R.-H. Carlos Omar, T.-G. Saúl Emmanuel, C. Olvera-Sandoval, F. Y. Ramírez-Castillo, A. Loera Muro, F. J. Avelar-Gonzalez, and A. L. Guerrero-Barrera, *Cell Culture: History, Development and Prospects,* International Journal of Current Research and Academic Review **3**, 252 (2015).

[78] R. Freshney, *Culture of Animal Cells: A Manual of Basic Technique and Specialized Applications* (Wiley, 2015).

[79] M. A. Harrison and I. F. Rae, *General Techniques of Cell Culture*, Handbooks in Practical Animal Cell Biology (Cambridge University Press, 1997).

[80] A. Cardinale, *Basic cell culture protocols,* Allergy & Clinical Immunology International - Journal of the World Allergy Organization **17**, 228 (2005).

3

MICROFABRICATED POROUS PDMS MEMBRANES

The contents of this chapter are based on the work published in:

1. W. F.Quirós-Solano, N.Gaio, O. M. J.A. Stassen, Y. B.Arik, C. Silvestri, N.C.A.Van Engeland, A.Van der Meer, R. Passier, C. M. Sahlgren, C.V. C. Bouten, A. van den Berg, R. Dekker and P. M. Sarro. *Microfabricated tuneable and transferable porous PDMS membranes for Organs-on-Chips.* Scientific Reports, 8, 13524 (2018).
2. W.F.Quirós-Solano, N. Gaio, C. Silvestri, Y.B. Arik, O.M.J.A. Stassen, A.D. van der Meer, C.V.C. Bouten, A. van den Berg, R. Dekker and P.M. Sarro. *A novel method to transfer porous PDMS membranes for high throughput Organ-on-Chip and Lab-on-Chip assembly.* 31st IEEE International Conference on Micro Electro Mechanical Systems, 2018.

3.1. INTRODUCTION

As indicated in the previous chapter, Organs-on-Chips (OOCs) generally consist of a 3D PDMS-based microfluidic structure fabricated using soft-lithography [1–3]. These chips comprise a top and bottom thick moulded PDMS substrate and host microfluidic channels that are often interfaced through a porous membrane, as schematically shown in Figure 3.1. Depending on the envisioned application, the membrane functions as co-culture support, artificial barrier or filter [4, 5].

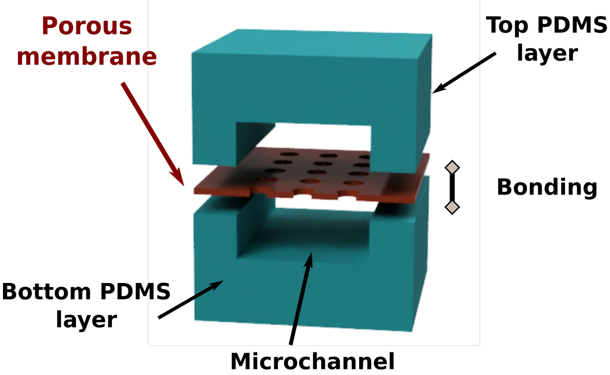

Figure 3.1: Typical OOC structure: A top and bottom PDMS layer hosting microchannels interfaced by a porous membrane.

Commercially available membranes made of materials such as polycarbonate (PC) and Polyethylene terephthalate (PET) have been traditionally used to create such porous interface for PDMS-based OOCs [6–8], as they are easily accessible and known to promote cell adhesion and growth. The porous surface of these materials is generally obtained by a track-etching process, using either chemical etching or ion bombardment [9].

More recently, efforts in tissue engineering have also enabled the use of electrospun materials creating highly porous biomaterials, namely nanofibrous membranes resembling scaffold-like structures [10, 11]. All these materials have been lately used to study cancer metastasis, to recreate organ-capillary interfaces, cell differentiation and proliferation, among others [12–15].

In most applications, membranes are normally required to have micron pore sizes and thicknesses to effectively mimic topography and mechanical conditions of the human body [5]. In some cases the pores position and distribution needs to be precisely defined to have higher control over the variables mostly influencing the mechanism under study. The contact area has been suggested to play an important role when studying notch signalling. For instance, reducing pore size with fixed spacing might affect cell-cell signaling area, with possible effects on cell fate [16]. Cell morphology and adhesion are also suggested to be influenced by the anisotropy of the membrane topology [17–19]. With track etched and electrospun membranes the control over pores positioning is cumbersome and consequently their application in studies investigating the role of surface topology on cell-cell interaction and morphologyis limited. The incomplete transparency, in the case of PC and PET, might also interfere with the optical characterization of cell responses [20].

3.1.1. MICROFABRICATED POROUS MEMBRANES

As an alternative, porous membranes made of parylene [21], SU8 [22] and PDMS [23, 24] have been developed using conventional microfabrication techniques, such as photolithography and dry etching [25, 26]. Unlike the track etching process and electrospun deposition, such techniques allow precise positioning of the pores, providing higher accuracy and local control of the porosity and enabling the fabrication of larger-area membranes in a timely and cost-effective manner. However, including such non-conventional materials in standard microfabrication processes is not trivial and the related technological development is not as far developed as for rigid materials such as silicon, oxides, nitrides and metals. Patterning polymeric materials with features smaller than 5 μm in a reproducible and reliable way is still challenging. Recently, Kim *et al.* optimized the lithography and etching process for parylene, fabricating porous membranes with pore sizes down to 1 μm and porosity up to 40% [21]. Esch *et al.* did a similar work with SU8, reaching minimum features of 8 μm for membranes down to 0.5 μm thick [22].

Despite the outstanding features achieved by the aforementioned literature and the proof of concepts developed using these materials, most membranes are not completely suited for OOCs with specific mechanical requisites, such as low stiffness and elasticity, as required to enable stimulation of cells and tissues through mechanical stretching. Thus, most OOCs rely on PDMS due to its well-known elasticity (ϵ >5%), low stiffness (E<5 MPa) and well known biocompatibility [2–5, 27]. However, patterning such polymer with standard lithography is still difficult due to its surface chemistry and thermomechanical properties [27]. On one side, previous works have focused on improving the patterning of the polymer by tuning the lithographic steps and etching conditions, successfully reducing the minimum feature size down to 4 μm [23, 28]. Nevertheless, the treatment of the surface prior to photoresist (PR) deposition is not sufficient to overcome uniformity issues caused by inactivated regions or topography variations across the substrate. Moreover, the photoresist is prone to crack during baking steps due to the high thermal expansion of PDMS, limiting the minimum feature sizes that can be patterned. Such non-uniformity on the polymer surface during processing causes low reproducibility and limits the maximum patternable area. On the other side, Wang *et al.* achieved 2 μm pore sizes with an alternative solution based on the overlapping of two porous PDMS membranes [24]. Nonetheless, this approach requires the two layers to be processed separately and the quality of the resulting membrane is very dependent on the accuracy of the alignment and the manual procedures needed to overlap both layers.

3.1.2. PDMS POROUS MEMBRANES

Porous PDMS membranes for OOC applications have been mostly developed through replica moulding (Figure 3.2). By using such fabrication method, outstanding concepts of devices such as lung-on-chip and gut-on-chip have been reported [4, 5]. However, membrane characteristics such as minimum pore size, thickness and porosity levels are constrained by this method. As replica moulding relies strongly on time-consuming manual procedures, creating thin porous membranes (<10 μm) with just few micron pore sizes (<5 μm), high porosity and uniform and predefined pore distribution requires extreme caution. Intrinsic issues such as unwanted adhesion of the material with the mould or blockage of the pore can easily compromise the structural stability of the highly fragile microstructures [5]. Additionally, there is always the risk of including batch to batch differences that also affects the yield and scalability of the device manufacturing.

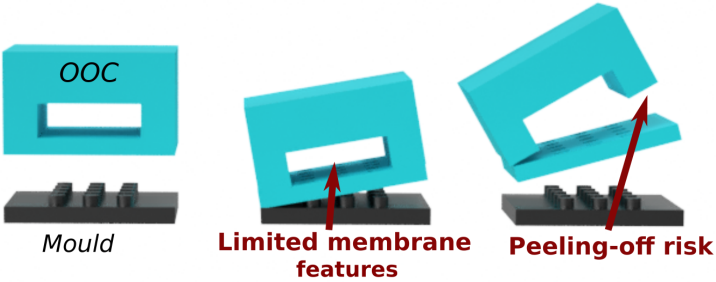

Figure 3.2: The shortcomings of replica molding , the most used available methods for developing and assembling of OOCs with porous PDMS membranes.

3.2. MICROFABRICATED PDMS POROUS MEMBRANES

In this chapter, a novel and reproducible process to fabricate transferable porous PDMS membranes for OOCs using microelectromechanical systems (MEMS) fabrication technologies is presented. Firstly, with this process, a minimum pore feature size smaller than previously reported and a very high porosity can be realized [23, 28, 29]. Secondly, both pore size and porosity can be accurrately and locally tuned. The technology employed also offers a high control on the distribution of the pores across large surface areas. Thirdly, aiming to overcome issues brought by conventional replica moulding for fabricating OOCs and improve their scalability and reproducibility, a sacrificial layer to easily transfer the membranes from the silicon substrate has been included to the process. The process does not need any risky manual handling when defining the critical features of the membrane (pore size, porosity), allowing to fabricate and transfer functional PDMS porous membranes thinner than ever before reported [29]. To confirm their biocompatibility two cell types human umbilical endothelial cells (HUVEC) and MDA-MB-231 (MDA) cells were cultured on the membranes fabricated and transferred with this new process. The experiments with MDA cells focuses on studying morphology and transmigration, while the experiments with HUVECS in migration and barrier function of cell monolayers.

3.2.1. DESIGN AND MICROFABRICATION

Highly porous PDMS membranes were fabricated using conventional IC and MEMS fabrication technology in a cleanroom facility (Class 100, ISO 5). The design parameters considered are pore to pore distance (P-P), pore size (PS) and thickness (t) of the layer, as depicted in Fig. 3.3.

The porosity is defined by as the ratio between the volume of voids to the total vol-

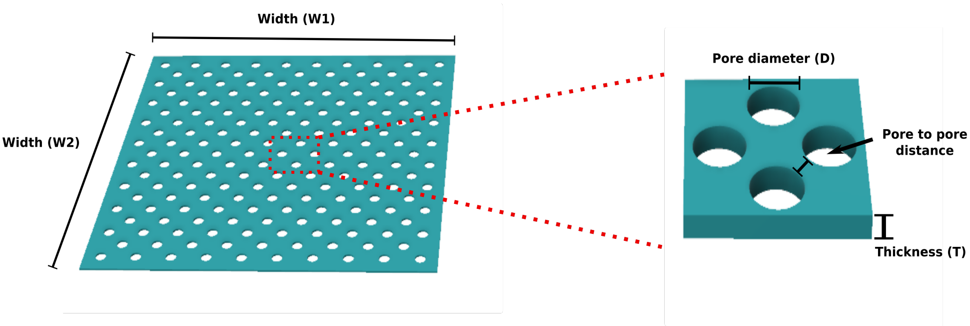

Figure 3.3: Three dimensional sketch of a porous PDMS membrane specifying the adopted terminology: pore size (*PS*), pore to pore distance (*P-P*), membrane thickness (*T*) and membrane area ($W_1 \times W_2$).

ume, as shown in Equation 3.1.

$$Porosity(\%) = \frac{Voidvolume}{Totalvolume} = \frac{VoidsurfaceT}{TotalsurfaceT} = \frac{\pi\left(\frac{PS}{2}\right)^2}{\left(PS + P - P\right)^2} \cdot 100 \tag{3.1}$$

The porosity can be successfully tuned by varying *PS* and *P-P* to accommodate the requirements of the envisioned applications. The mask design for a first set of membranes included the porosities reported in Table 3.1.

Table 3.1: Features and the corresponding porosity of diverse 4μm-thick porous PDMS membranes successfully fabricated and transferred with the process reported.

		Pore to Pore Distance (P-P)			
		$1\,\mu m$	$2\,\mu m$	$3\,\mu m$	$4\,\mu m$
Pore Size (PS)	$2\,\mu m$	35%	19%	12%	8%
	$5\,\mu m$	54%	40%	31%	24%
	$10\,\mu m$	65%	54%	46%	40%

The process, depicted in Fig. 3.4a-e, was developed to achieve high control over the pore size, and porosity by tuning the thermal budget of the lithography process and by including an Aluminum (Al) masking layer to improve both the Photoresist (PR) to PDMS adhesion and the mechanical stability. In fact, the use of an Al mask guarantees a highly uniform PR layer, crucial for achieving small pore sizes.

A sacrificial polymeric layer was initially deposited on a 100 mm-Si wafer (Fig. 3.4a-b). Two different sacrificial layers have been tested in this work: (a) a 3 μm standard PR layer (PR), (b) a 0.5 μm Poly(acrylic acid) (PAA) layer. The photoresist was deposited by spin coating at 2000 rpm for 30 s and baked on a proximity hotplate at 100 °C for 90 s. The PAA sacrificial layer was deposited by spin coating at 4000 rpm for 40 s and baked in a temperature controlled oven at 100 °C for 1 h. Subsequently, a PDMS layer was deposited by two-step spin coating, the first spreading step at 300 rpm and the second step at 6000 rpm (Fig. 3.4c). The spinning time was tuned to achieve the desired layer thickness. Values ranging from 2 to 20 μm can be obtained with spinning times in the 30 to

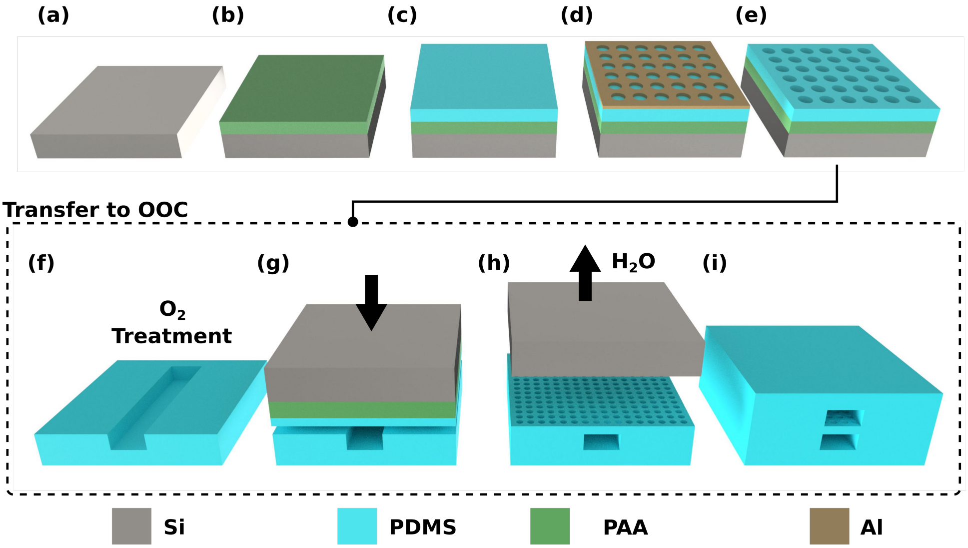

Figure 3.4: Schematic illustration of the microfabrication process (from (a) to (e)) and the transfer (from (f) to (i)) of the porous PDMS membranes to OOCs. **(a-b)** Deposition of the sacrificial and water-soluble poly(acrylic acid) (PAA) layer by spin coating. **(c)** Deposition of the PDMS by spin coating to define the membrane thickness. The layer is then thermally baked. **(d)** Deposition and patterning of the Al masking layer to define the desired pore features (*PS* and *P-P*). **(e)** Dry etching of the Al and the PDMS layers. The Al masking layer is then removed by wet etching, leaving exposed the patterned PDMS surface. **(f)** First step required for transferring the membrane: oxygen plasma treatment on the PDMS membrane and on the bottom surface of the PDMS-based OOCs. **(g)** The porous membranes, carried by the silicon substrate, are placed in contact with the activated surfaces of the OOCs and then kept under a constant pressure to promote mechanical bonding. **(h)** Releasing of the porous membranes by dissolving the sacrificial layer (PR or PPA)in water in an ultrasonic bath. **(i)** Final assembling of the OOC by attaching the top part to complete the microchannel top side.

150 s range. The polymer was cured at 90 °C for 1 h. Then, an Al layer, used as hard mask, was sputtered on the polymer surface (Fig. 3.4d). A 1 μm photoresist layer was deposited and patterned with proximity exposure. Several pore densities were achieved on the same wafer as various arrangement of the holes were included in the mask layout. The Al masking layer is then removed by reactive-ion etching with a Chlorine (Cl^-)-based plasma chemistry. Subsequently, the PDMS is etched by reactive-ion etching (Gases: CH_4:SF_6:O_2:1:2:1, P: 20 mTorr, Reactive Ion Etching (RIE) Bias: 20 W, Inductively Coupled Plasma(ICP) Power: 500W) in an ICP plasma etcher. The etching conditions were optimized to obtain anisotropic etching, so to accurately control shape and size of the pores. Finally, the Al hard mask was removed by wet etching using a buffered solution of acetic acid, nitric acid and hydrofluoric acid (Fig. 3.4e). More details can be found in Appendix B.1.

3.2.2. MEMBRANES CHARACTERIZATION

The developed lithographic process allowed to microfabricate membranes with *PS* from 2.0 ± 0.3 μm to 10 ± 0.3 μm and *P-P* from 1 μm to 4 μm (Fig. 3.5).The minimum *PS*

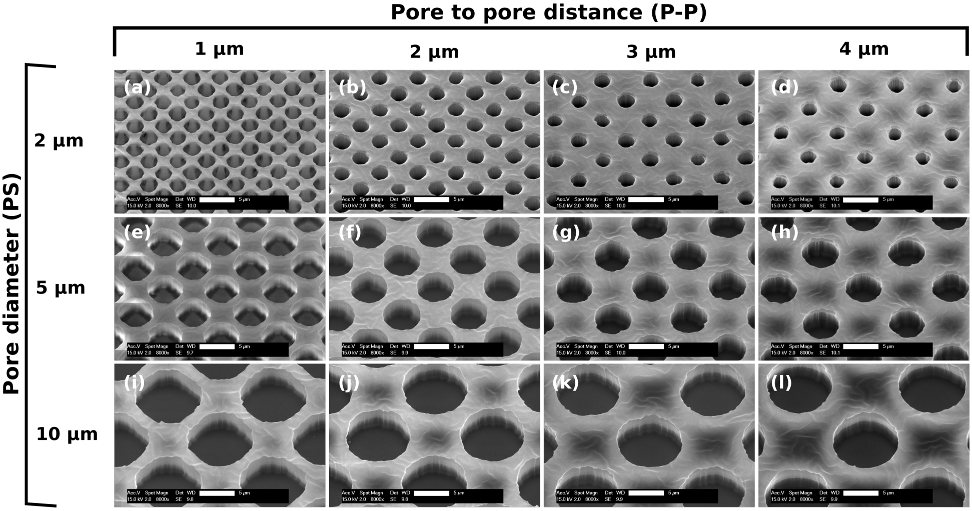

Figure 3.5: SEM images of the different patterned 4 μm-thick porous PDMS layers, with various *P-P* and *PS*, taken at a fixed magnification (8000x) and tilting angle of 26°. Scale bars: 5 μm.

achieved, 2.0 ± 0.3 μm (Fig. 3.5a), is two times smaller than previously reported [24]. Substrates layers without significant structural defects were obtained at wafer level, corresponding to porous surface areas as large as 78 cm^2.

In Fig. 3.5 scanning electron microscopy (SEM) images highlighting the wide range of porosity achieved are shown. In particular, the porosity ranges from 8% to 65%, demonstrating a significantly extended range compared to what reported by others [22–24]. The highest porosity (65%) corresponds to the layers with *PS* = 10 μm and *P-P* = 1 μm (Fig. 3.5i) while the lowest (8%) corresponds to *PS* = 2 μm and *P-P* = 4 μm (Fig. 3.5d). To achieve the various porosities with photolithography, the exposure time was kept constant and the development time was properly tuned. All layers were imaged by SEM with the same magnification (8000x) and tilting angle (26°) to show the same perspective.

Moreover, cross-section images of the layers were obtained during the experiments to determine the complete etch through of the PDMS and to investigate the etched wall profile. An example of those images can be seen in Figure 3.6, corresponding to a membrane with a 5 μm pore size. Membranes with larger than 10 μm pore size can be also defined with this process.

In addition to higher porosities and smaller features sizes, with the current process it was also possible to realize a novel scaffold-like membrane (Fig. 3.7). To the best of our knowledge this is the first time this kind of structure developed in PDMS is reported. The microstructures can be obtained in a partially controlled procedure. In Figure. 3.7d-f SEM images of the scaffolds are shown. A close-up (Fig. 3.7e-f) shows the scaffold-like membranes as a porous membrane with an additional opening. The opening is in the walls that separate one pore (main pore) from the other. This characteristic increases the porosity significantly to values even higher than the one achievable with the single porous layer configuration. For instance, as shown in Fig. 4e, corresponding to a porous

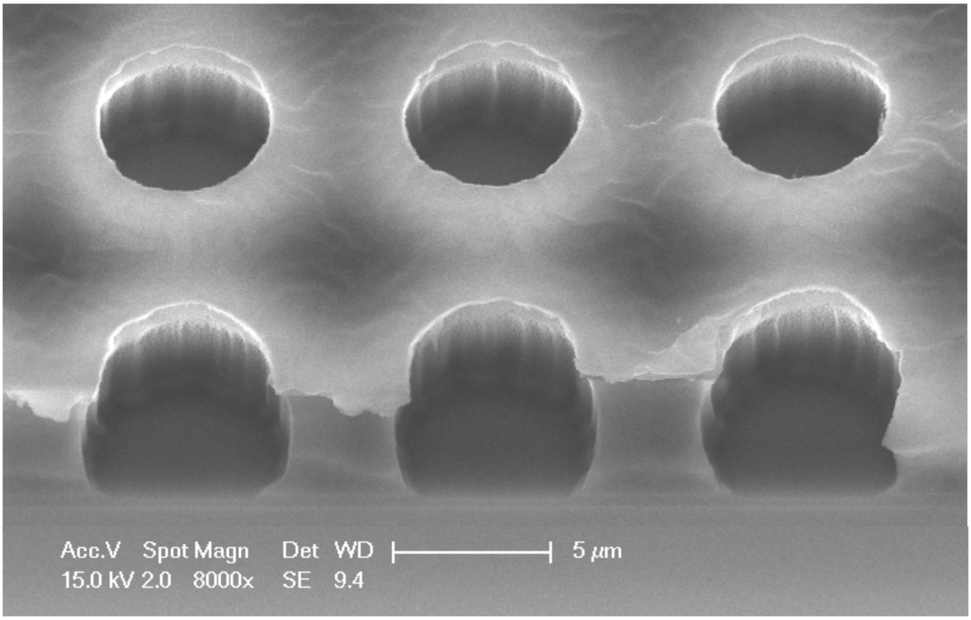

Figure 3.6: Cross-section SEM image of an 8μm-thick and 5 μm pore size PDMS membrane patterned and transferred with the process presented. Scale bars: 5 μm.

size of 8 μm, distance between pores 1 μm and considering a 10 μm-thick PDMS layer, the porosity increases from 62 % to 80 % . To develop the scaffold-like microstructures the geometry and etching conditions need to be tuned to induce the removal of the walls. Experiments showed that the walls are opened easily as the distance between holes is decreased and also varies with the thickness of the PDMS layer. A separation of 1 μm is the optimal distance found to realize the microstructures faster and in a fully controlled manner.

In Figure. 3.7a-c, SEM images taken at three different times (T1-T3), are shown. At the beginning, once the pores are etched through (T0), the walls angle profile is as expected. After the first over etching step ($T1 = 0.2T0$), the walls started to etch and the profile became more irregular and curved towards the wall, which indicates possibly a more isotropic behaviour of the etching process. After the second over etching step ($T2 = 0.35T0$), the walls were perforated through leaving the scaffold-like membranes. The final size of the holes in the wall was observed to be directly proportional to the over etching time, allowing to potentially control the porosity of the microstructures.

Moreover, it was also observed a correlation on the position of the holes of the wall with the over etching time, pore diameter and thickness of the membrane. Given the ratio ($\xi = T/D$), where D is the pore diameter and T the membrane thickness by design, numerous experiments showed that for ratios lower than 1 ($\xi < 1$), the microstructures were realized in a shorter time ($t < T2$) with the hole positioned at a lower height the pore wall, closer to the bottom. In Figure. 3.7e-f, an example of this is shown which corresponds to layers of 4 μm thickness and 10 μm pore size. On the other side, for

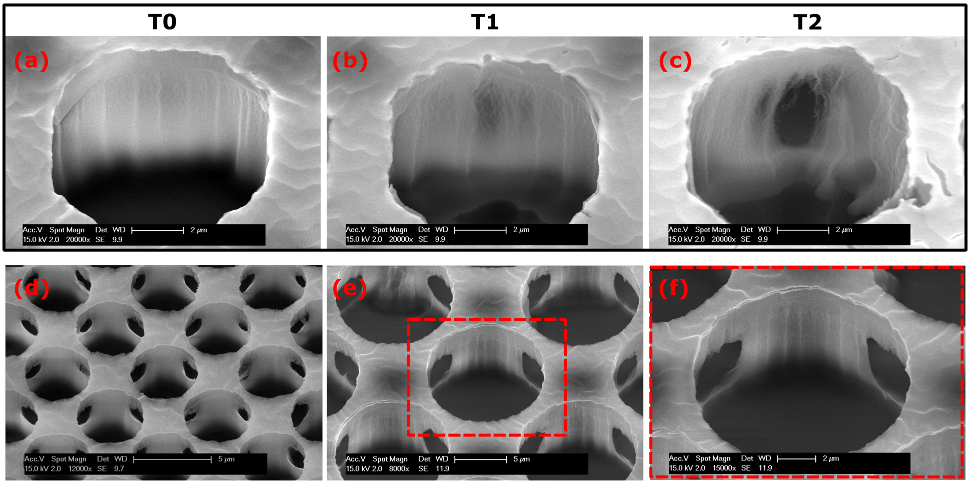

Figure 3.7: PDMS scaffolds realized with the fabrication process proposed. SEM images taken at three different times after having open completely the pores: **(a)** T0, time necessary to open the pores completely. **(b)** T1, over-etch time after opening the pores corresponding to approximately 20% of T0. **(c)** T2, over-etch time after opening the pores corresponding to approximately 35% of T0. Time necessary to realize the scaffold-like structures. **(d-f)** Different SEM images of the final microstructures realized after time T2.

aspect ratios higher than 1 ($\xi > 1$), the wall holes were completely opened in a longer time ($t \geqslant T2$) and positioned close to the center of the pore wall. This is the case for layers of 10 μm thickness and pore sizes between 4-8 μm (Fig. 3.7a-d).

The scaffold-like structures can thus be controlled by finely tuning the size and position during design phase and depending on the level of high porosity required by the application, although further investigation is needed to evaluate the reproducibility and understand other parameters influencing the etching process. The scaffolds-like structures were imaged with same magnification (8000x) and tilting angle of 26° used for the single porous layers.

3.3. SUSPENDED POROUS PDMS MEMBRANES

With the process developed, the membranes can also be suspended. A silicon frame can be created to hold the porous PDMS membranes clamped on its sides thus leaving certain area of the porous PDMS suspended. This area can be accurately defined by introducing a masking layer ($6\ \mu SiO_2$) on the back of the wafer patterned with conventional lithography. The membrane is then released by etching the masked Si from the back of the wafer using a Bosch-based Deep Reactive Ion Etching (DRIE) process. Figure 3.8a-b, shows SEM and optical images of successfully suspended membranes taken from the back and front-side of the silicon frame, respectively.

3.4. TRANSFER OF POROUS PDMS MEMBRANES

The next step towards verifying the functionality of such membranes and its applicability would be their integration into conventional OOC devices. However, to do so, either

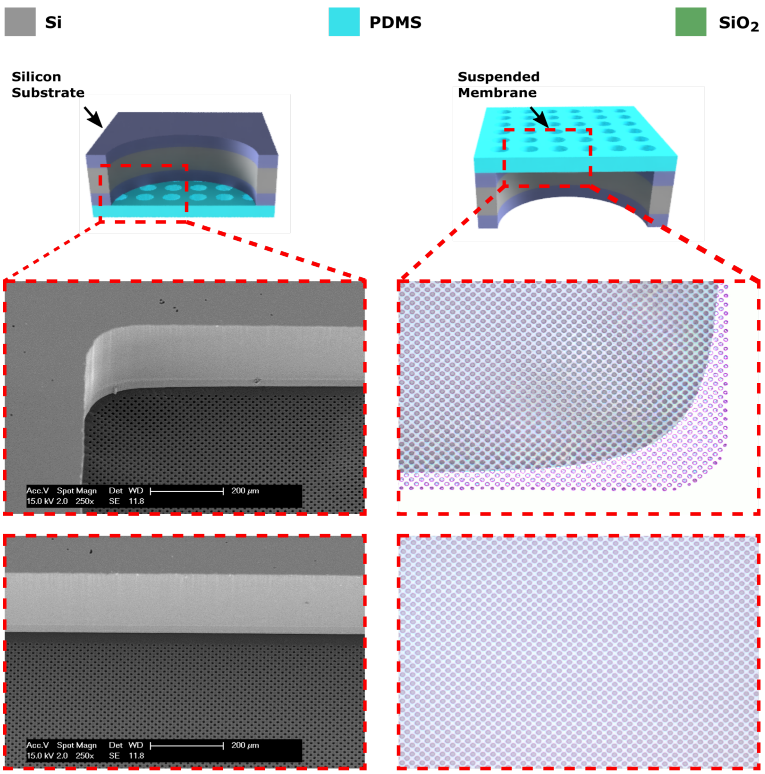

(a) **(b)**

Figure 3.8: Square shaped (5 mm size) suspended porous PDMS membranes (5 μm-thick) released on a silicon frame. **(a)** SEM images taken as seen from the backside of the silicon frame. **(b)** Optical images taken as seen from the front-side of the silicon frame.

a significant change on the way every single OOC is fabricated or a fully manual transfer of the membrane from the silicon substrate to the OOC would be necessary. The extensive literature available on many OOC devices clearly suggests that the adaptation of every single of this devices to the microfabricated porous membranes will not be the most efficient and cost-effective way to make a significant contribution in the way OOC are fabricated. Moreover, attaching the membranes with procedures highly dependent on manual handling, as often done with PET and PC membranes, relies on end-user skills for proper alignment (Fig. 3.9). This manual handling hampers the scalability of the manufacturing and assembling of OOC devices and most likely increases the risk of including batch to batch differences which might compromise the validity of the results.

Thus, in combination with the advanced microfabrication process previously described, a novel method to transfer the tunable porous PDMS membranes was also developed to extend its applicability to most OOCs (Fig.3.4f-i). After defining the features of the porous membranes, it is possible to transfer them to any PDMS-based OOC by using a sacrificial layer. Two materials were investigated and used as sacrificial layer, PR and

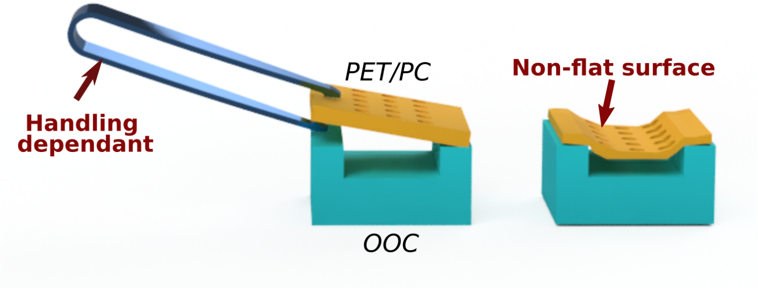

Figure 3.9: The shortcomings of manual attachment, an alternative available for attaching porous materials to OOC devices.

PAA, for the transfer of the microfabricated membranes from the silicon substrate to two different OOCs. Once the porous membrane was patterned as previously described, the silicon substrate was diced with an automatic dicing saw to match the dimensions of the OOC. Subsequently, the device bottom part and the porous layers were treated with oxygen plasma to activate the surface and guarantee their mechanical bonding. The porous layer and the OOC bottom substrate were brought together. A minimum constant force is then applied for 8 hours on the assembly to promote the bonding between the two elements (Fig. 3.4f-g). Finally, the silicon substrate was detached from the PDMS chip (Fig. 3.4h) by submerging the PDMS and silicon assembled chip in either water or acetone using an ultrasonic bath for 10 min, depending on the sacrificial layer used.

Two sacrificial layers were employed to investigate their effect on the biocompatibility and reproducibility of the fabrication process and the transferring method. Photoresist was firstly chosen due to its easy accessibility and well-known controlled deposition techniques. Moreover, it has also been used in previous works to release thin non-porous PDMS membranes [30]. On the other side, PAA is known for its high solubility in water and has previously been demonstrated as suitable sacrificial layer in 2D micromachining to develop sensors and actuators [31].

In initial experiments PR was used as as sacrificial layer as it had already been used and reported to release thin non-porous PDMS membranes [30]. However, bigger PR residues were always observed after transferring (Fig. 3.10a). These residues were detected both inside the microchannels and on the surface of the membranes.

The residues could be cleaned afterwards by increasing the time of submersion in acetone. However, this soaking of the PDMS assembly in acetone caused detachment of the porous membranes. The detachment was often observed in the experiments done with chips with lower PDMS substrate surface area (4 cm^2). Long-time submersion in organic solvents is known to affect the surface of PDMS causing swelling of the layers or its detachment [32]. Consequently, special attention was paid during its cleaning to avoid this problem which might affect the final assembly of the PDMS-based OOC. Moreover, the transfer mechanism using photoresist as sacrificial layer was observed to be highly dependent on manual handling and thus time consuming. The bonded PDMS layers and silicon chip were submerged in methanol and acetone for a long time ($t \geq 15$ min)

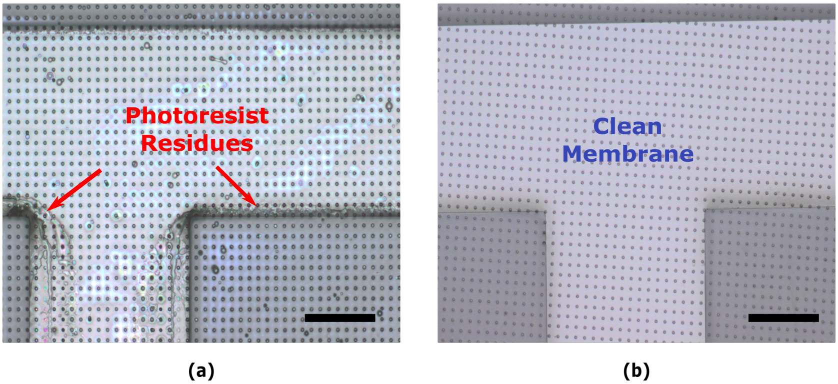

Figure 3.10: Optical images of 4 μm-thick PDMS porous membranes after being transferred to an OOC chip using as sacrificial layer: **(a)** Photoresist, residues are observed on the walls of the microchannel and the porous surface of the membranes and **(b)** PAA, the walls of the microchannels and the porous membranes are clean after release. Scale bars: 200 μm.

to strip the PR sacrificial layer. To accelerate the stripping of the sacrificial PR layer and to release the PDMS assembly from the silicon carrier substrate, an external force was applied. This force was applied manually by slightly bending the OOC to allow access of the stripping solvent. This procedure affects the reproducibility of the transfer method, which suggested the need of using an alternative material.

When using PAA as sacrificial layer, the release of the porous membranes from the silicon carrier is rather straightforward. As depicted in Fig. 3.4h, the PDMS assembly was only submerged in deionized (DI) water in an ultrasonic bath. After 10 min the assembly spontaneously detaches from the silicon substrate. The results demonstrate that PAA guarantees a cleaner surface and no residues inside the microchannel (Fig. 3.10b). The few residues observed in a couple of samples during the fabrication experiments were easily removed in DI water. In Figure 3.11, optical microscope images of transferred membranes (Fig. 3.11b-c), of 8 μm and 4 μm in pore size, are reported for one of the OOC devices used for the biocompatibility assessments, a device previously reported for measuring transepithelial electrical resistance (TEER) to study cellular barrier tightness (Fig. 3.11a) [33].

Numerous transfers for different porosities (Fig. 3.12) and *PS* were successfully performed, achieving a transfer success rate higher than 85%. A transfer process is considered successful when no sagging of the membrane nor PAA residues in the microchannels are observed.

By relying on a bulk carrier substrate compatible with IC and MEMS fabrication techniques, our process guarantees a good reproducibility and flat transferred membranes with minimum pore sizes smaller than those achievable with replica molding. This highly reliable process reduces the need of manual handling as well as the associated risks, allowing also functional membranes thinner than before reported [29] to be successfully transferred at chip level. The method is suitable for automated assembling techniques based on robotics, such as pick-and-place, since for several steps it is only needed to bring two surfaces in close contact.

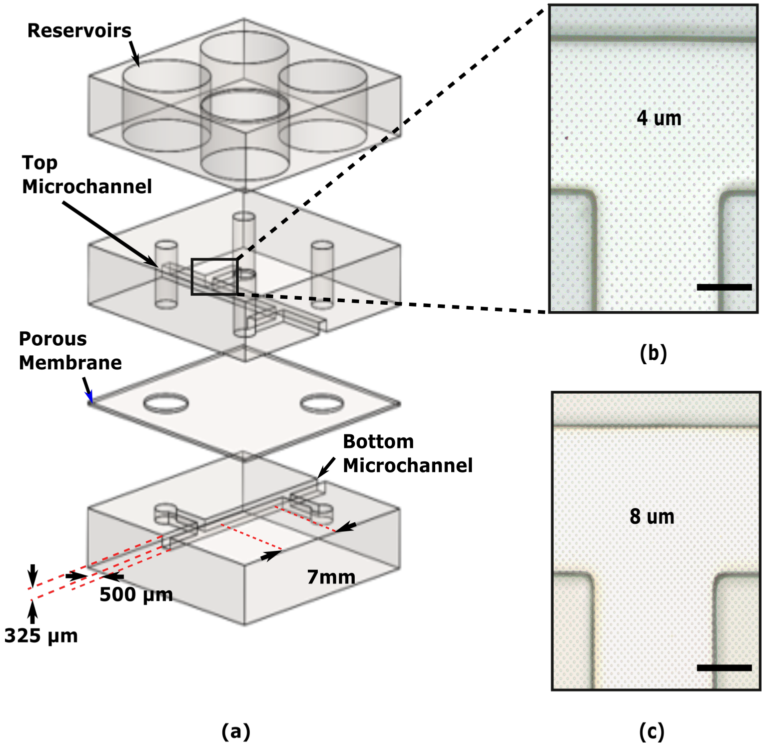

Figure 3.11: The architecture used in the experiments of HUVECs culturing on transferred PDMS membranes. **(a)** Schematic representation of the OOC. A four-layered sandwich consisting of bottom layer with a defined microchannel (500 μm width, 325 μm height, 7 mm in length), porous PDMS membrane with defined pores (8 μm diameter, 4 μm in thickness), top layer with the same channel dimensions as the bottom layer, and PDMS slab with defined reservoirs for media refreshing (5 mm in diameter). **(b)** Close-up of the microchannel area with transferred membrane of 4 μm in pore size. **(c)** Close-up of the microchannel area with transferred membrane of 8 μm in pore size. Scale bars: 100μm.

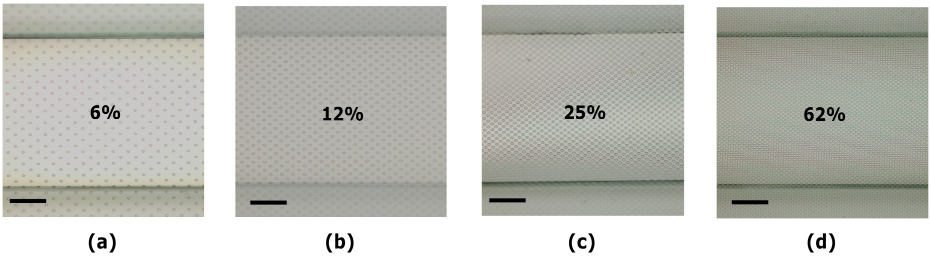

Figure 3.12: Optical images of 8 μm pore size, 4 μm-thick membranes of different porosities transferred to OOCs using a PAA sacrificial layer. Porosity value: **(a)** 6%, **(b)** 12%, **(c)** 25% and **(d)** 62%. Scale bars: 125 μm.

3.5. BIOCOMPATIBILITY ASSESSMENT

To confirm the biocompatibility of porous PDMS membranes two cell types human umbilical endothelial cells (HUVEC) and MDA-MB-231 (MDA) cells, were cultured on porous

PDMS membranes fabricated and transferred with the method described in previous sections. Once the transfer of the PDMS membranes is completed, prior to cell seeding in one of the microchannels, the surface of the microchannel is functionalized to promote adhesion and growth of the cells as well as of the proper extracellular matrix the cells need. Subsequently, cells have to be incubated for a determined time depending on the cell line and the cell mechanisms to study.

The following subsections present in detail the procedures followed to culture and assess the viability of (HUVEC) and MDA-MB-231 (MDA) cell cultures on two different OOC devices with the porous membranes fabricated and transferred with our process.

3.5.1. HUVEC CULTURING ON THE POROUS MEMBRANES

In Figure 3.13a, a complete OOC device after transferring the membranes and prior to HUVEC cell seeding is shown. In this specific case, a chip with a 25% porosity membrane is used. As clearly shown in Figure 3.13b, flat and clean membranes were successfully transferred.

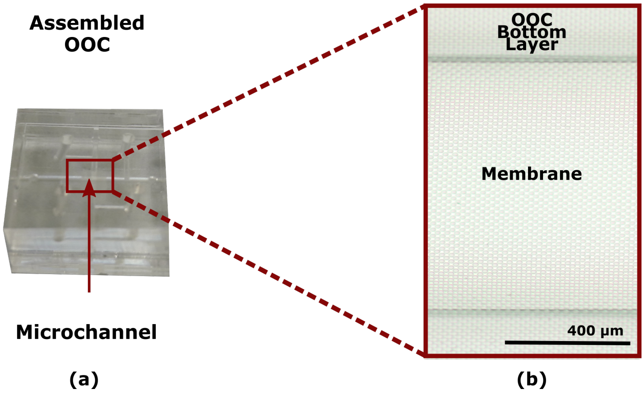

Figure 3.13: Optical images of: **(a)** the fully assembled OOC device; **(b)** a close-up of the microchannel area with the transferred porous membrane. Scale bar: 400 μm.

SURFACE FUNCTIONALIZATION AND CELL SEEDING

The surfaces of the microchannels were functionalized with (3-Aminopropyl)triethoxysilane (APTES) and glutaraldehyde. First, chips were subjected to air plasma (50 W) for 40 s (Cute, Femto Science). Afterwards 3% (v/v) APTES mixed in ultrapure H_2O (ELGA) was added into the channels and incubated at room temperature (RT) for 5 min. Following APTES coating, the chips were rinsed thoroughly with 100% ethanol, and incubated for 5 min to eliminate the remaining APTES. Then 10% glutaraldehyde was added and the chips were incubated for 5 min at RT. This was followed by thorough rinsing with distilled H_2O and drying overnight at 60 °C.

Prior to cell seeding, the microfluidic chips were rinsed with Phosphate-buffered saline (PBS) and coated with 0.1 mg mL^{-1} collagen I for 30 min at 37 °C. After coating, channels were flushed with cell medium to remove non-bound collagen. First, HUVEC were obtained from a confluent flask using 0.05% Trypsin-EDTA suspended in fresh Endothelial Growth MEdia (EGM-2) at 2x10^6 or 5x10^6 cells mL^{-1} density and pipetted into the top channel of a assembled OOC. Cells were attached by incubating the chips for 30 min under static culture conditions. After that, non-attached cells were washed away by flushing the microchannels with fresh EGM-2. A droplet of EGM-2 was left on the reservoirs to prevent drying. Cells were kept in static culture conditions and medium in the channels was refreshed twice daily by pipetting fresh EGM-2 into the channels.

HUVEC were cultured with EGM-2 in t175 culture flasks, coated with 0.1mg mL^{-1} collagen I. The cells were incubated at 37 °C in humidified air with 5% CO_2. When cells had grown to confluent monolayers, they were either used for control experiments.

CELL CHARACTERIZATION

As part of the characterization of cell viability, cell migration experiments of HUVEC seeded on the OOC of Figure. 3.13 were carried out. Cells were cultured on 8 ± 0.3 μm pore size membranes with 25% porosity. Initially seeded only on the top channel of the device, HUVEC were seen to show active mechanisms of migration through the membrane to the bottom channel of the device (Fig. 3.14). Cells formed cell-cell junctions as it can be seen from the adherens junctions in the VE-Cadherin stainings (Fig. 3.14b, bottom), which also indicates a healthy population with a well-established cellular barrier formation.

The cell migration was confirmed to be not induced by the seeding but governed by the cell behavior. Cell staining performed after 2 hours of seeding did not show cells under the membrane whereas, after 18 hours, cells were seen in the bottom channel, as illustrated in Figure 3.15.

In addition to the cell migration, the barrier function of endothelial monolayers was briefly examined based on fluorescent dye diffusion, analogous to a technique that is extensively used in ophthalmology to assess barrier integrity of blood vessels. Barrier integrity was visualized by tracking fluorescein diffusion (Fluorescein sodium salt; 0.3 kDa, ex/em: 460/515). Devices were cultured for at least 2 days prior to experimentation. Afterwards, 15 μg mL^{-1} fluorescein diluted in endothelial basal medium (EBM-2, with 2% FBS and 1% P/S) was added to one of the inlets of the HUVEC microchannel. This was followed by mounting devices on EVOS FL Cell Imaging System (Life Technologies) taking sequential images with 10 s intervals for 10 min.

The same OOC shown in Figure 3.13a, was used for such experiments. Dye diffusion starts within 30 s from the supply of the dye to the upper channel of an empty device. On the contrary, the device containing a monolayer of HUVEC exhibited no dye diffusion to the bottom channel, which demonstrates the formation of a well-established endothelial barrier on the PDMS membranes, despite the high porosity and large pore size. Quantification of fluorescent intensity indicates that the values were significantly higher for membranes without cells, as 140 times higher fluorescent intensity in empty devices was found. The fluorescent images are shown in Figure 3.16, illustrating the behaviour above described.

3.5.2. MDA-MB-231 CELL CULTURES

Using an OOC based upon the lung-on-a-chip architecture [34], MDA cells were cultured in two parallel microchannels separated by a transferred porous PDMS membrane to in-

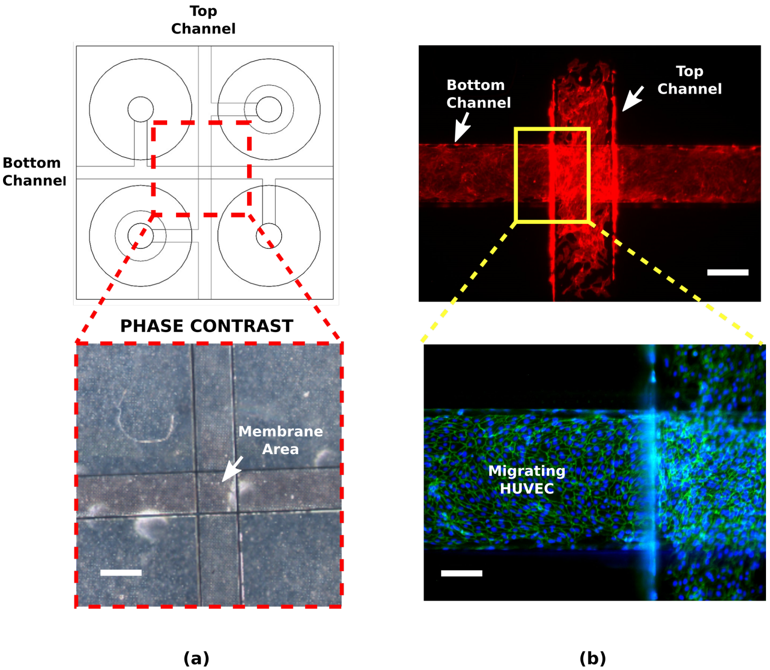

Figure 3.14: Porous PDMS membranes provide support for cell culturing. **(a)** A top view schematic of the OOC chip with a Phase contrast image of the membrane area, which is transparent giving visibility to the PDMS different layers. **(b)** Initially seeded to the top channel, cell migrated to the adjacent channel upon prolonged culturing. Staining of cell-cell junction proteins (B-bottom) indicates a healthy barrier formation by the cells. Red: phalloidin, cytoskeleton; green: VE-Cadherin, adherens junctions; blue: DAPI, nuclei. Scale bars: 100 μm.

vestigate transmigration (Fig. 3.17). Membranes were fabricated with either 2.0 ± 0.3 μm (Type A), 3.0 ± 0.3 μm (Type B) or 10.0 ± 0.3 μm (Type C) pore size (*PS*), with fixed porosity (40%) to investigate whether cell transmigration occurs when using such artificial barrier.

SURFACE FUNCTIONALIZATION AND MDA CULTURING

MDA cells were cultured on porous PDMS membranes transferred to an OOC where the membrane served as interface separating the top and bottom microchannel. MDA-MB-231 cells (MDA) were maintained in MDA-medium (RPMI, 10% FBS, 100 U/mL Penicillin/Streptomycin) at 37 °C in humidified air with a 5% CO_2 concentration. For all OOC experiments with MDA, the OOCs with parallel culture microchannels were first sterilized with 70% ethanol, washed with phosphate PBS and coated with fibronectin and again washed with PBS. To test permissiveness of the porous membranes to cell transmigration, cells were seeded at a density of $5\text{x}10^4$ cells cm^{-2} on the membrane in the bottom channel. After seeding, the cells were starved overnight by loading the OOC with serum free medium. To induce migration, a difference of 50 ng mL^{-1} of Epidermal growth factor (EGF) was established between the top microchannel inlet and the bottom channel inlet, and cells were cultured for 24 hours.

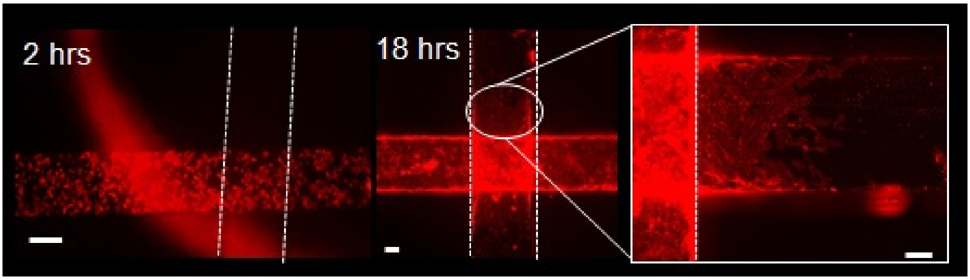

Figure 3.15: Cell seeding procedure did not result in cells passing through the membrane. Cell staining was performed after 2 and 18 hours following seeding. At 2 hours after seeding (left), no cells were observed under the membrane whereas after 18 hours (middle), cells can be seen in the adjacent channel (right, inset). Scale bar: 50 μm.

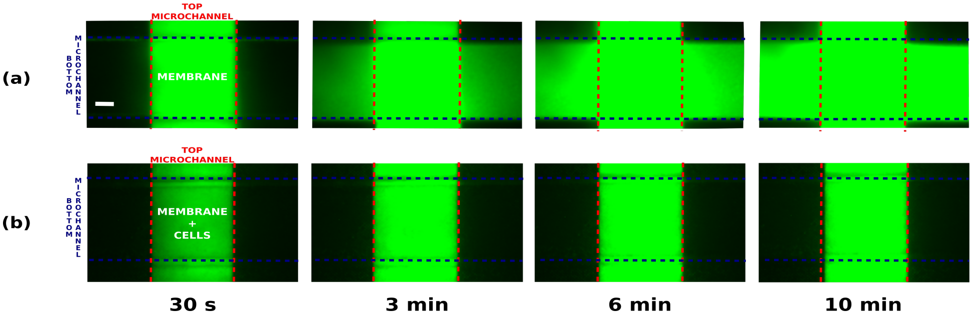

Figure 3.16: Barrier function assessment using fluorescein angiography in the OOC device with transferred PDMS membranes with and without HUVEC Cells. Following fluorescein (0.3 kDa) administration to the top microchannel (vertical lane, red lines), diffusion of fluorescein to the bottom channel (horizontal lane, blue lines) was visualized by taking sequential images for 10 min for an OOC device. **(a)** Empty microchannel, diffusion of florescent dye started after 30 s. **(b)** A microchannel with HUVEC monolayer, diffusion of fluorescent dye not observed after 10 min. Scale bar: 100 μm.

To test cell exchange across the porous PDMS membrane due to migration, cells were loaded with CellTracker Orange or CellTracker Green, and seeded at a density of 5x10^4 cells cm^{-2} in the bottom or the top microchannel respectively. After 24 hours the devices were imaged with a Zeiss LSM510 META NLO, using a long-distance objective (LD Achroplan).

To study cell interaction with the porous surface of the PDMS membranes, they were transferred and subsequently coated with fibronectin. MDA cells were seeded at a density of 1x10^4 cells cm^{-2} and fixed with 4% paraformaldehyde (PFA) the following day. Cells were permeabilized and blocked with NET-Gel (50 mM Tris, pH7.5, 150 mM NaCl, 0.1% v/v Nonidet P40, 1 mM EDTA, 0.25% w/v Gelatin), and subsequently stained with phalloidin-alexa-488 and 4‘,6-diamidino-2phenylindole (DAPI) and imaged with an epifluorescent microscope (Zeiss Axiovert 200M).

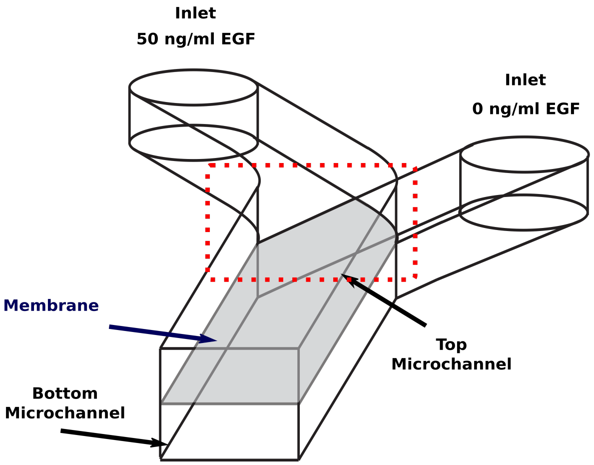

Figure 3.17: MDA cell transmigration through porous PDMS membrane transferred to a OOC. Schematic of the OOC used for EGF driven migration, showing the inlets for top and bottom microchannel (400 μm width, 100 μm height) where EGF is added. Cells were seeded at the bottom side of the membrane, serum starved overnight and exposed to a gradient of EGF towards the top channel.

CELL CHARACTERIZATION

MDA cells were cultured on the bottom side of the membrane and attracted with EGF supplied from the top side (Fig. 3.18a). Cells were also cultured in a device with a non-permeable membrane as reference sample and no cell migration was observed. Type A and Type B membranes allowed for processes of cells probing the top inlet (Fig. 3.18b-c), but no migration into the top inlet was observed. Type C membranes allowed for transmigration and cells migrating towards the EGF gradient (Fig. 3.18d).

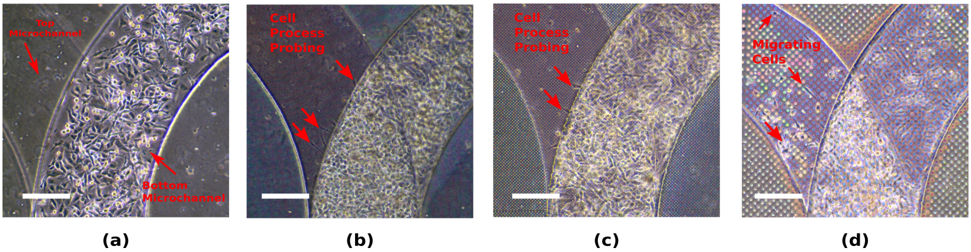

(a) (b) (c) (d)

Figure 3.18: MDA cell transmigration through porous PDMS membrane transferred to a OOC. Cells were seeded at the bottom side of the membrane, serum starved overnight and exposed to a gradient of EGF towards the top channel, separated with either with a **(a)** nonporous; **(b)** 2.0 ± 0.3 μm pore size (Type A); **(c)** 3.0 ± 0.3 μm pore size (Type B) and **(d)** 10.0 ± 0.3 μm pore size (Type C) membrane. Arrows indicate cells **(e)** or cellular processes (c, d) probing in the channels. Scale bar: 50 μm.

To further confirm this transmigration across the membranes, MDA cells were labelled with different florescent colors and then seeded on either side of a membrane to evaluate exchange between the two sides after 24 hours. In the case of Type C membranes, some cells were seen to migrate completely through the membrane, whereas for

Type B membranes only sporadic protruding through the membrane was observed. This can be seen in Figure 3.19a-c and Figure 3.19g-i, respectively.

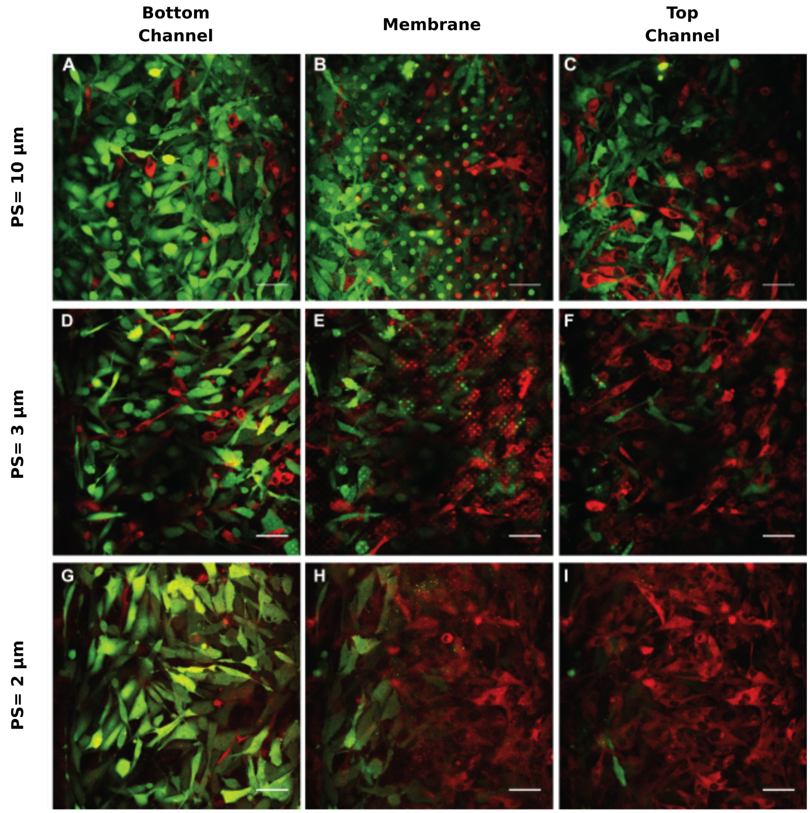

Figure 3.19: CellTracker Orange (red) and CellTracker Green labelled MDA-cells were seeded on either side of the membrane in a parallel channel OOC. Using confocal imaging focussing on either the surface of the membrane (B,E,H), top membrane plane (Orange cells seeded; C,F,I) or the bottom membrane plane (Green cells seeded, A,D,G). The cells remained at their side of seeding in the case of 1.8 m pore size (G-I) membranes. In the case of 3.2 m pores infrequent protrusions could be seen probing towards the opposite side of the membrane (Arrow, D-F). In the case of 10 m pores, cells could be identified that had most of their cell body at the opposing side of the membrane, indicating transmigration (Arrows, A-C). Scale bar: 50 μm.

Additionally, to briefly investigate the effect of the different pore sizes of the microfabricated membranes on cell morphology, MDA cells were also cultured on membranes transferred onto a flat PDMS substrate. In the case of Type A and Type B pores, cells grow on top of the membrane and can probe into the pores, as demonstrated by polymerized actin condensation at the pores (Fig. 3.20a-b). On membranes with Type C pores, cells can deposit their nucleus entirely into the pore and extend the rest of the cell body towards a neighbouring pore (Fig. 3.20c). Although descriptive, another remarkable difference is the effect on the shape of cells, with the cells following the grid of the pores, especially in the case of the Type B and the Type C pore membranes. This leads to rectangular or even linear shapes, whereas the Type A pores leave more freedom in cell morphology.

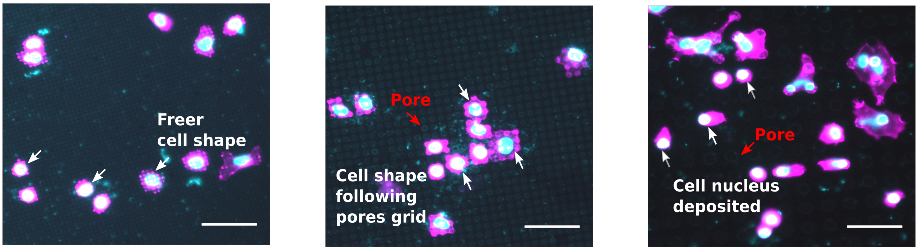

(a) **(b)** **(c)**

Figure 3.20: MDA interaction with porous PDMS surface. Cell and nuclear morphology was imaged on PDMS porous membranes transferred to a PDMS substrate. Pore size of the PDMS membranes **(a)** 2.0 ± 0.3 μm (Type A) **(b)** 3.0 ± 0.3 μm (Type B) and **(c)** 10.0 ± 0.3 μm (Type C). Scale bar: 50 μm.

3.5.3. VASCULAR INTERSTITIAL CELLS

Similarly, to demonstrate the viability of co-culturing, porous membranes were transferred and both HUVECs and VICs were co-cultured in the same device as of Figure 3.17. VICs were cultured on the bottom microchannel, and similarly as the previous experiments; HUVECs were cultured on the top channel . The porous membranes create an artificial interface between both cell types. In Figure 3.21, a florescence microscopy image obtained through confocal microscope show the cells on both sides of the porous membranes seeded in the corresponding microchannels.

Both, the HUVECs and VICs in contact with the membranes showed healthy morphology, demonstrating once again the validity of the method to develop and transfer biocompatible PDMS porous membranes in OOC.

3.6. DISCUSSION AND CONCLUSIONS

In the fabrication process of the porous PDMS membranes, the thermal budget is the most critical factor to be controlled during the lithography steps to achieve the reported minimum features. The temperature was kept lower than 90 °C to both prevent cracking of the photoresist due to thermal expansion mismatch, and avoid high degassing of the polymeric layers. Smaller features (PS<2 μm) could not be achieved without affecting the shape, uniformity and distribution of the pores during development steps of the photolithographic process.

Numerous experiments were performed to determine the optimal procedure to transfer clean and flat microfabricated porous membranes to the OOCs. Using PAA as sacrificial layer guarantees a higher reproducibility and no detachment, rupture or sagging of the membrane. Its high solubility in water makes the transfer easier and more reliable than with other sacrificial layers. When using photoresist, residues were always present which can be largely removed with a longer rinsing in methanol and acetone. However, this unavoidably causing unwanted detachment of membranes in sporadic areas.

The process here presented can be easily adapted to bigger wafer sizes, further increasing the final porous membrane area. However, additional tuning of the lithography might be required to successfully achieve the features reported under such new con-

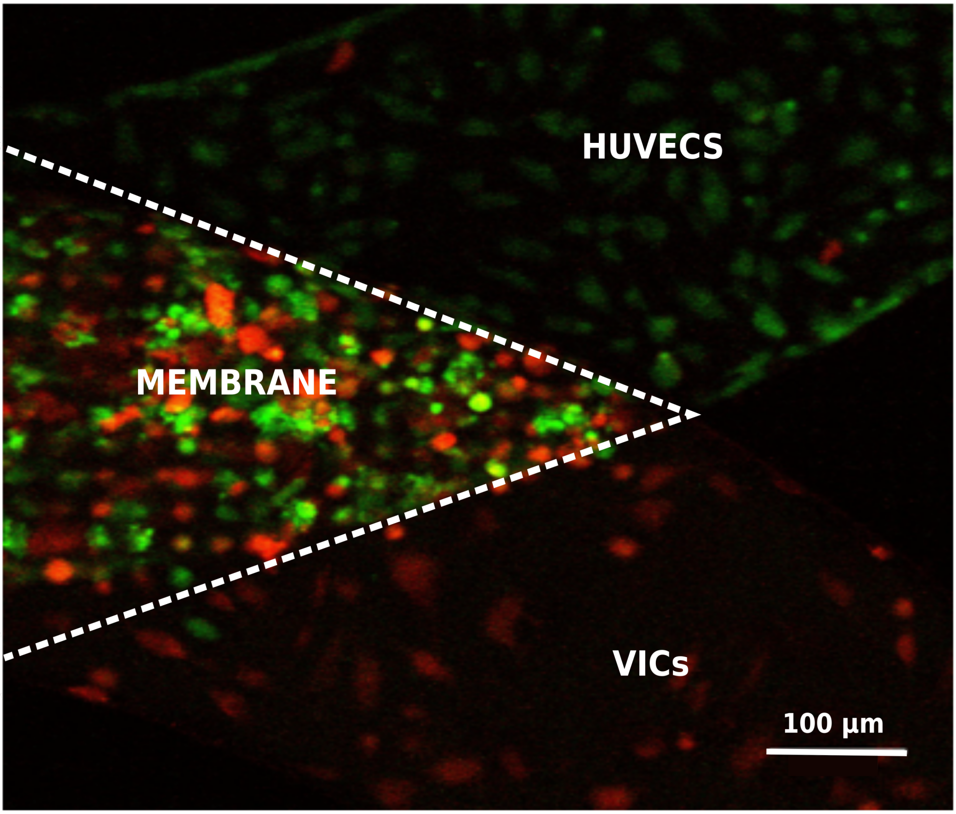

Figure 3.21: Fluorescence confocal images of the cells cultured on a membrane transferred to a OOC device. Scale bar: 100 μm.

ditions. Unlike other works [2], the process allows to fabricate and transfer numerous PDMS porous membranes in one day (24 h). For example, considering an average-sized OOC (3 cm × 3 cm), by processing 5 silicon substrates (10 cm diameter) in parallel and considering the success rate reported, up to 85 membranes can be fabricated and transferred. The process, based on scalable fabrication techniques, proposes an alternative that allows to increase the yield when fabricating traditional PDMS-based OOCs. However, this process is not completely feasible for rapid and low-cost prototyping, as its implementation requires specialized facilities more suitable for higher scale manufacturing.

The biocompatibility and viability of cell cultures on the membranes transferred to OOC devices was proven by culturing two different cell lines: HUVEC and MDA cells. Here, MDA cells showed healthy morphology depending on pore size. The applicability of the membranes with such cell cultures was assessed through experiments on cell transmigration, demonstrating the ability for complete cell transmigration through 10 μm pores only, with migration restriction for 3 μm and 2 μm pore size, as well as a profound effect on cell morphology based upon the membrane topology. The results showed the pore size and porosity have a direct influence both on the transmigration of MDA cells and its morphology. Moreover, we confirmed the barrier formed by a healthy monolayer of HUVEC as indicated by expression of cell-cell junction proteins (i.e. VE-Cadherin) on porous PDMS membranes. In addition, these membranes allowed for cell migration, as well as providing low resistance against diffusion of fluorescent dye. Thus, our study demonstrates the potential of using porous PDMS membranes in studies investigating the underlying mechanisms of cell migration and changes in barrier integrity.

REFERENCES

[1] Y. Xia and G. M. Whitesides, *Soft lithography,* Annual Review of Material science **28**, 153 (1998), arXiv:1111.6189v1 .

[2] D. Huh, Y.-s. Torisawa, G. a. Hamilton, H. J. Kim, and D. E. Ingber, *Microengineered physiological biomimicry: organs-on-chips.* Lab on a chip **12**, 2156 (2012).

[3] a. K. Capulli, K. Tian, N. Mehandru, a. Bukhta, S. F. Choudhury, M. Suchyta, and K. K. Parker, *Approaching the in vitro clinical trial: engineering organs on chips.* Lab on a chip **14**, 3181 (2014).

[4] D. Huh, G. a. Hamilton, and D. E. Ingber, *From 3D cell culture to organs-on-chips.* Trends in cell biology **21**, 745 (2011).

[5] D. Huh, H. J. Kim, J. P. Fraser, D. E. Shea, M. Khan, A. Bahinski, G. a. Hamilton, and D. E. Ingber, *Microfabrication of human organs-on-chips.* Nature protocols **8**, 2135 (2013).

[6] R. Booth and H. Kim, *Characterization of a microfluidic in vitro model of the blood-brain barrier (μBBB),* Lab on a Chip **12**, 1784 (2012).

[7] A. K. H. Achyuta, A. J. Conway, R. B. Crouse, E. C. Bannister, R. N. Lee, C. P. Katnik, A. A. Behensky, J. Cuevas, and S. S. Sundaram, *A modular approach to create a neurovascular unit-on-a-chip,* Lab Chip **13**, 542 (2013).

[8] L. M. Griep, F. Wolbers, B. De Wagenaar, P. M. Ter Braak, B. B. Weksler, I. A. Romero, P. O. Couraud, I. Vermes, A. D. Van Der Meer, and A. Van Den Berg, *BBB on CHIP: Microfluidic platform to mechanically and biochemically modulate blood-brain barrier function,* Biomedical Microdevices **15**, 145 (2013).

[9] P. Apel, *Track etching technique in membrane technology,* Radiation Measurements **34**, 559 (2001).

[10] K. I. Budhwani, V. Thomas, and P. Sethu, *Lab-on-a-brane: Nanofibrous polymer membranes to recreate organ-capillary interfaces,* Journal of Micromechanics and Microengineering **26** (2016), 10.1088/0960-1317/26/3/035013.

[11] S. M. Giannitelli, M. Costantini, F. Basoli, M. Trombetta, and A. Rainer, *Electrospinning and microfluidics: An integrated approach for tissue engineering and cancer,* in *Electrofluidodynamic Technologies (EFDTs) for Biomaterials and Medical Devices: Principles and Advances* (Elsevier Ltd, 2018) pp. 139–155.

[12] H. Eslami Amirabadi, S. SahebAli, J. P. Frimat, R. Luttge, and J. M. den Toonder, *A novel method to understand tumor cell invasion: integrating extracellular matrix mimicking layers in microfluidic chips by selective curing,* Biomedical Microdevices **19** (2017), 10.1007/s10544-017-0234-8.

[13] P. Wallin, C. Zandén, B. Carlberg, N. Hellström Erkenstam, J. Liu, and J. Gold, *A method to integrate patterned electrospun fibers with microfluidic systems to generate complex microenvironments for cell culture applications,* Biomicrofluidics **6**, 1 (2012).

[14] M. Teng, Y. Li, S. T. Yang, and D. A. Kniss, *Effects of pore size in 3-D fibrous matrix on human trophoblast tissue development,* Biotechnology and Bioengineering **70**, 606 (2000).

[15] Y. Takahashi and Y. Tabata, *Effect of the fiber diameter and porosity of non-woven PET fabrics on the osteogenic differentiation of mesenchymal stem cells,* Journal of Biomaterials Science, Polymer Edition **15**, 41 (2004).

[16] O. Shaya, U. Binshtok, M. Hersch, D. Rivkin, S. Weinreb, L. Amir-Zilberstein, B. Khamaisi, O. Oppenheim, R. A. Desai, R. J. Goodyear, G. P. Richardson, C. S. Chen, and D. Sprinzak, *Cell-Cell Contact Area Affects Notch Signaling and Notch-Dependent Patterning,* Developmental Cell **40**, 505 (2017).

[17] A. Mitra, S. Venkatachalapathy, P. Ratna, Y. Wang, D. S. Jokhun, and G. V. Shivashankar, *Cell geometry dictates TNFα-induced genome response,* Proceedings of the National Academy of Sciences **114**, E3882 (2017).

[18] N. W. Karuri, *Biological length scale topography enhances cell-substratum adhesion of human corneal epithelial cells,* Journal of Cell Science **117**, 3153 (2004), arXiv:NIHMS150003 .

[19] A. Teixeira, G. McKie, J. Foley, P. Bertics, P. Nealey, and C. Murphy, *The effect of environmental factors on the response of human corneal epithelial cells to nanoscale substrate topography,* Biomaterials **27**, 3945 (2006), arXiv:15334406 .

[20] V. Pensabene, L. Costa, A. Y. Terekhov, J. S. Gnecco, J. P. Wikswo, and W. H. Hofmeister, *Ultrathin Polymer Membranes with Patterned, Micrometric Pores for Organs-on-Chips,* ACS Applied Materials and Interfaces **8**, 22629 (2016).

[21] M. Y. Kim, D. J. Li, L. K. Pham, B. G. Wong, and E. E. Hui, *Microfabrication of high-resolution porous membranes for cell culture,* Journal of Membrane Science **452**, 460 (2014).

[22] M. B. Esch, J. Yang, C. Yu, J. Yu, J. C. March, and M. L. Shuler, *On chip porous polymer membranes for integration of gastrointestinal tract epithelium with microfluidic ... On chip porous polymer membranes for integration of gastrointestinal tract epithelium with microfluidic,* Biomed. Microdevices (2015), 10.1007/s10544-012-9669-0.

[23] W. Chen, R. H. W. Lam, and J. Fu, *Photolithographic surface micromachining of polydimethylsiloxane (PDMS),* Lab on a Chip **12**, 391 (2012).

[24] H. Wei, B.-h. Chueh, H. Wu, E. W. Hall, C.-w. Li, R. Schirhagl, J.-m. Lin, and R. N. Zare, *Particle sorting using a porous membrane in a microfluidic device* , Lab on a Chip , 238 (2011).

[25] J. Garra, T. Long, J. Currie, T. Schneider, R. White, and M. Paranjape, *Dry etching of polydimethylsiloxane for microfluidic systems,* Journal of Vacuum Science & Technology A: Vacuum, Surfaces, and Films **20**, 975 (2002).

[26] S. J. Hwang, D. J. Oh, P. G. Jung, S. M. Lee, J. S. Go, J. H. Kim, K. Y. Hwang, and J. S. Ko, *Dry etching of polydimethylsiloxane using microwave plasma,* Journal of Micromechanics and Microengineering **19**, 095010 (10pp) (2009).

[27] E. Berthier, E. W. K. Young, and D. Beebe, *Engineers are from PDMS-land, Biologists are from Polystyrenia,* Lab on a Chip **12**, 1224 (2012).

[28] X. Fan, C. Jia, J. Yang, G. Li, H. Mao, Q. Jin, and J. Zhao, *A microfluidic chip integrated with a high-density PDMS-based mi- crofiltration membrane for rapid isolation and detection of circulating tumor cells,* Biosensors and Bioelectronics **71**, 380 (2015).

[29] J. M. Karlsson, T. Haraldsson, C. F. Carlborg, J. Hansson, A. Russom, and W. Van Der Wijngaart, *Fabrication and transfer of fragile 3D PDMS microstructures,* Journal of Micromechanics and Microengineering **22**, 085009 (9pp) (2012).

[30] E. Kang, J. Ryoo, G. S. Jeong, Y. Y. Choi, S. M. Jeong, J. Ju, S. Chung, S. Takayama, and S.-h. Lee, *Nanomembranes,* Advanced Materials , 2167 (2013).

[31] V. Linder, B. D. Gates, D. Ryan, B. A. Parviz, and G. M. Whitesides, *Water-soluble sacrificial layers for surface micromachining,* Small **1**, 730 (2005).

[32] J. N. Lee, C. Park, and G. M. Whitesides, *Solvent Compatibility of Poly(dimethylsiloxane)-Based Microfluidic Devices,* Analytical Chemistry **75**, 6544 (2003).

[33] M. W. van der Helm, M. Odijk, J. P. Frimat, A. D. van der Meer, J. C. T. Eijkel, A. van den Berg, and L. I. Segerink, *Direct quantification of transendothelial electrical resistance in organs-on-chips,* Biosensors and Bioelectronics **85**, 924 (2016).

[34] D. Huh, B. Matthews, A. Mammoto, M. Montoya-Zavala, H. Hsin, and D. Ingber, *Reconstituting Organ-Level Lung,* Science , 1662 (2010).

4

SILICON/POLYMER-BASED ORGAN-ON-CHIP DEVICE

4.1. INTRODUCTION

The state-of-the-art in Organ-on-Chip (Chapter 2) still shows how this interdisciplinary field depends highly on devices developed through manual handling-based fabrication processes. In spite of numerous efforts , there still are several key features of this traditionally fabricated devices that could largely benefit by using microfabrication techniques [1–5]. Among such features, microfluidic structures such as microchannels are fundamental in such application, as they can help to recreate the microvasculature of the human body providing the cell cultures with better mechanical and biochemical stimulation, e.g. perfusion to the cell culture and mechanical stimulation through controlled shear stress [6–8]. Development in microfluidics and particularly in the Lab-on-Chip field over the last two decades, have made the realization of numerous and outstanding proofs of concept possible [9–12]. However, such solutions keep relying on soft-lithography and glass processing, making them only convenient for rapid prototyping for basic research but not for its highly envisioned use in the drug development pipeline.

This chapter, in line with previous efforts (Chapter 2), proposes a monolithically microfabricated device for its application as an Organ-on-Chip for disease modelling and *in vitro* testing. Here, the technical aspects of its development are detailed, namely design, fabrication, characterization and some of the first steps taken for biological validation. The device is presented as an alternative to replace conventionally developed OOCs preserving their traditional capabilities and introducing potential additional features. To do so, the advantages and opportunities given by the mature IC and MEMS fabrication techniques and microfluidics are exploit. Moreover, the device is developed to benefit from these fabrication techniques to facilitate the further inclusion of monitoring and stimulation trough the integration of sensors and actuators [11, 13–18], envisioning an alternative paradigm of Organ-on-Chip devices fully interfaced with state-on-the-art microelectronics capabilities. In order to demonstrate the functionality of the device mechanically and hydraulically, a single channel device was fabricated and fully characterized including an initial validation by culturing endothelial cells (HUVECs) in the microchannel and cardiomyocytes in the silicon cavity.

4.2. MONOLITHICALLY FABRICATED ORGAN-ON-CHIP DEVICE

The proposed device comprises a monolithically fabricated chip with embedded microfluidics in a thick and flexible polymeric membrane. The materials used and its tunable design gives a high versatility that enable different microenvironments for cell culturing. A variety of signals might be supplied (e.g perfusion, oxygenation and mechanical stress) to cells cultured within the device. These characteristics make the device ideal as an OOC for disease modeling and *in vitro* drug testing. A 3D sketch of the device is shown in figure 4.1.

As depicted in 4.1a-b, the device consists of a modular chip with embedded porous membranes and microfluidic channels. The microfluidic features enables perfusion to a cell microenvironment cultured on either inside the microchannel or the open cavity. The features of the porous membranes can be tuned as required for the envisioned application, as demonstrated in Chapter 3. Both microstructures, microchannels and porous layers, make possible to mimmick a minimal organ unit with microvasculature

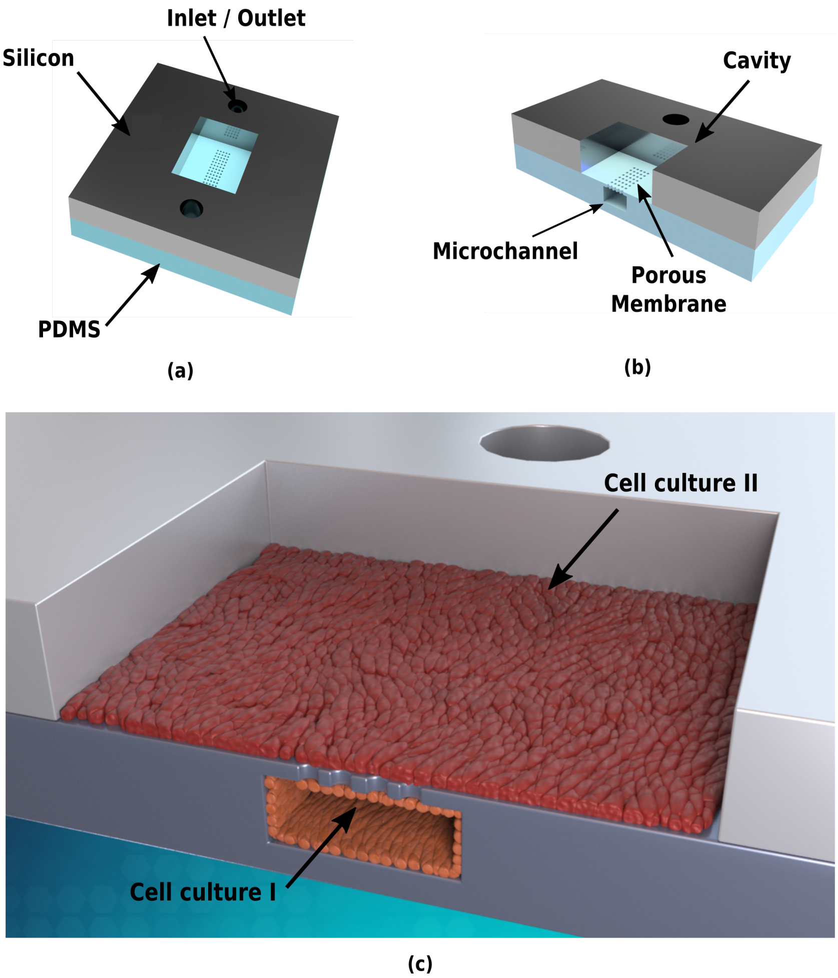

Figure 4.1: A 3D sketch of **(a)** The microfabricated device for OOC application: Microfluidic inlets and outlets available in the silicon substrate are highlighted. **(b)** Cross section of the device, showing the embedded microchannels and porous membranes on the PDMS thick layer. **(c)** The potential use of the device for culturing more than one cell line, cells cultured inside the microchannel (light orange) and cells on the top silicon cavity (red) [19]

for cell perfusion. Figure 4.1c illustrates how the device can be used to provide a microenvironment for more than one cell culture. The configuration and cell lines possible to culture on the functional parts of the chip can vary according to the minimal organ unit necessary to model. For instance, endothelial cells can be used as *Cell culture I* while cardiomyocytes as *Cell culture II* to develop the minimal unit of a heart (heart-on-chip) to study the cross-interaction between these two cell lines in fundamental biology experiments or cardiotoxicity assessment of new drug candidates [20–25].

4.3. DEVICE DESIGN

The microfabricated OOC has been designed to provide the highest versatility to stimulate and possibly monitor diverse cell microenvironments cultured in the microchannel and cavity. The design along with the fabrication techniques employed allows to have more than one cavity or microchannel implemented to accommodate the requirements of the models envisioned.

In order to further illustrate the design methodology followed to develop the device, this section presents the procedure to define the dimensions of the microchannels, silicon cavity and membrane size based on theoretical concepts of fluid flow, continuum mechanics and the envisioned biological microenvironments to model.

4.3.1. MICROFLUIDICS DESIGN

The design here reported corresponds to the particular case of a device with one microchannel. However, the same methodology is applicable for a design requiring a microfluidic circuitry of relatively higher complexity.

The dimensions of the microchannels are defined based on theoretical background supported in the equations governing the behaviour of fluid flow [26, 27]. Briefly, the behaviour of any fluid flow can be described by a set of equations known as the Navier-Stokes equations. These field equations, shown in 4.1 and 4.2, are obtained when applying Newton′s Law to a differential volume (Figure 4.2a) using an Eulerian description of the motion [28].

$$\rho\Big(\partial_t \mathbf{v} + \big(\mathbf{v}\cdot\nabla\big)\mathbf{v}\Big) = -\nabla p + \eta\nabla^2\mathbf{v} + \rho\mathbf{g} + \rho_{el}\mathbf{E} \tag{4.1}$$

$$\nabla\cdot\mathbf{v}(\mathbf{r}, t) = 0 \tag{4.2}$$

Where in Navier-Stokes equations $\mathbf{v}$ is the flow velocity field, ρ the fluid density, p the pressure difference, $\mathbf{g}$ the gravity and $\mathbf{E}$ the electric field.

Given the typical small scales (characteristic lengths) in microfluidics and particularly in the envisioned applications of the device developed, the viscous effects are expected to dominate over gravity effects on the the behaviour of the fluid. Thus, the fluid velocities expected would be low (characteristic flow velocity) and turbulence mostly absent. Under these conditions and static operation, the non-linear terms of the equations can be negligible and with further boundary conditions and specific channel geometry and dimensions, the velocity field can be analitically obtained [28].

The device is envisioned to be used with conventional pressure-driven pumping systems, thus the problem can be particularly reduced to the case of a constant pressure gradient (Δp) driving the flow along a microchannel with rectangular cross section (4.2). This simplifies further the system of equations. As shown in the Cartesian coordinate system, imposing the no slip boundary condition for the walls and the pressure gradient, the Navier-Stokes equations can be reduced to Equation 4.3 and Equation 4.4 for a rectangular microfluidic channel.

$$[\partial_y^2 + \partial_z^2]\mathbf{v}_x(y, z) = -\frac{\Delta p}{\eta L}, \text{ for } (y, z)\varepsilon\zeta \tag{4.3}$$

$$\mathbf{v}_x(y,z) = 0, \text{ for } (y,z)\varepsilon\partial\zeta \tag{4.4}$$

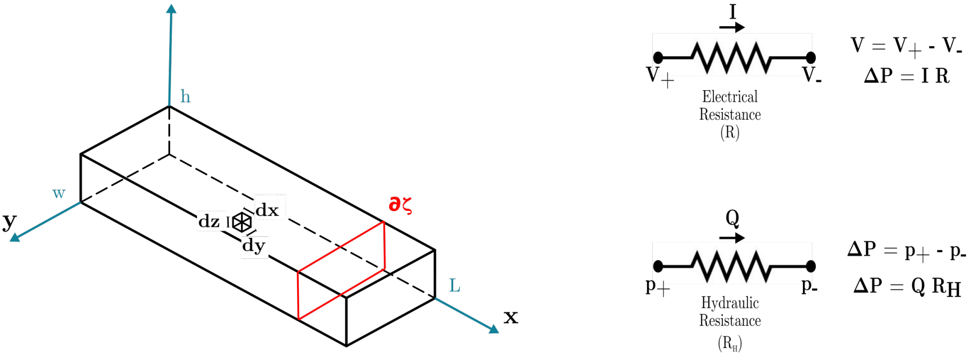

(a) **(b)**

Figure 4.2: **(a)** A 3D sketch of a microfludic channel with cross section under a constant pressure gradient and a no-slip boundary conditions. A fluid volume differential is also shown and the corresponding dimensions that define the microchannel; L: Length, W:Width, h:height. **(b)** A sketch illustrating the analogy between electric circuits and hydraulics and the equivalent hydraulic circuit of a simple microchannel as a resistive element.

FLOW VELOCITY

With a simplified set of equations, the velocity field can be solved for to fully understand the fluid flow behaviour. The influence of the geometrical features of the microchannels with the required cross-sectional area can be observed when this field is obtained. The system of equations, Equation 4.3 and Equation 4.4, are then solved considering the pressure and wall boundary conditions. Few approximations are necessary for solving the system as a finite rectangular channel is considered. (See further mathematical solution in Appendix A.1 [28].

$$\mathbf{v}_x(y,z) = \frac{4h^2\Delta p}{\pi^3\eta L}\sum_{n,odd}^{\infty}\frac{1}{n^n}\left[1-\frac{cosh\left(n\pi\frac{y}{h}\right)}{cosh\left(n\pi\frac{w}{2h}\right)}\right]sin\left(n\pi\frac{z}{h}\right) \tag{4.5}$$

FLOWRATE

In this case, it is of special interest to know the mathematical expression describing the relationship between the flow rate and pressure as a function of the microchannel dimensions, as these variables are directly accessible to the user of the device through the external fluidic circuitry. Thus, the expression considering the cross-sectional area of the rectangular channel(Figure 4.2a), with length L width w and height h, is given in Equation 4.6 and Equation 4.7 [26–28].

$$Q = \iint_V \mathbf{v}_x(y,z)\cdot dy\,dz = 2\int_0^{\frac{1}{2}w} dy\int_0^h \mathbf{v}_x(y,z)\,dz \tag{4.6}$$

$$Q = \frac{h^3 w \Delta p}{12 \eta L}\left[1 - \sum_{n,odd}^{\infty} \frac{1}{n^5} \frac{192}{\pi^5} \frac{h}{w} tanh\left(n\pi \frac{w}{2h}\right)\right] \tag{4.7}$$

For the special case in which the width of the micro channel is considerably greater that the height (w≫h), Equation 4.7 can be approximated as (See detail in Appendix A.2)

$$Q = \frac{h^3 w \Delta p}{12 \eta L}\left[1 - 0.630 \frac{h}{w}\right] \tag{4.8}$$

HYDRAULIC RESISTANCE

From Equation 4.8, it can be observed that for a constant pressure gradient or given the conditions of steady-state and pressure driven fluid flow through the rectangular channel, the flow rate (Q) is proportional to such gradient, the characteristics of the fluid and the dimensions of the channel (η,w, L, h). This can be seen in analogy with electric circuits, namely, as given by the electrical resistance of a material being dependent on the dimensions of the conductor and the properties of the material (Figure 4.2b). In microfluidics, this simplifies the fluid flow problems to the known Hagen-Poiseuille law [26, 28, 29], as given in Equation 4.9:

$$\Delta p = R_{hyd} Q = \frac{12 \eta L}{w h^3 \left[1 - 0.630 \frac{h}{w}\right]} Q \tag{4.9}$$

Hence, the hydraulic resistance R_{hyd} for a rectangular and finite microchannel of the device can be calculated as

$$R_{hyd} = \frac{12 \eta L}{w h^3 \left[1 - 0.630 \frac{h}{w}\right]} \tag{4.10}$$

where $[R_{hyd}] = \frac{Pa \cdot s}{m^3} = \frac{Kg}{m^4 s}$.

Figure 4.2b illustrates how the design of microfluidic networks can be reduced to equivalent hydraulic circuits in analogy with electric circuits. Other hydraulic variables such as the pressure drop (voltage drop) and compliance (capacitance) can be represented in analogy, as found in literature [29].

SHEAR STRESS

Once the relation between pressure drop and flowrate in the microchannel is understood, another variable of high interest for the envisioned application can be studied, namely the sheer stress. Shear stress is highly relevant for OOC applications as it is well-known to highly influence and determine the behaviour of cells e.g in endothelial and neuron cells [30–33]. Using the relations previously presented, the shear stress, expected to be experienced by the walls of a microchannel, can be obtained from Newton law of viscosity [26, 29], as given in Equation 4.11.

$$\tau = -\eta \frac{du}{dz} \tag{4.11}$$

Thus considering Equation 4.8 and the rectangular cross section of the microchannel, one can approximate the shear stress as function of the average flowrate:

$$\tau = \frac{6\eta Q}{wh^2} \tag{4.12}$$

Considering the theoretical bases reported above and potential limitations imposed by the fabrication process, an initial constraint towards the final design was established by fixing one dimension, namely the height (h=90 μm) of the microchannel. With this, the expected fluid dynamics of the device could be previously established and understood for different values of width (W) and length (L)before finalizing the layout. This was done always guaranteeing the use of reasonable ranges that allow to keep valid the assumptions of no turbulence and stationary flow behaviour.

In figure 4.3a-b, several curves corresponding to the flowrate and shear rate as function of the pressure gradient obtained trough the previous corresponding theoretical derivations for a few microchannel dimensions, are depicted. In Figure 4.3a, four cases of microchannels with different lengths are plotted for a defined width (w=400 μm) to visualize the variation of the flow rate in a fixed feasible pressure range (3 kPa). Figure 4.3b shows the corresponding shear stress expected at the walls for a channel with a fixed length (L=1800 μm) and different values for the width. These curves help in the design process to visualize and consider the effect of the final length and width of the microchannel on the total hydraulic resistance of the system and thus the pressure necessary to achieve the envisioned shear rates.

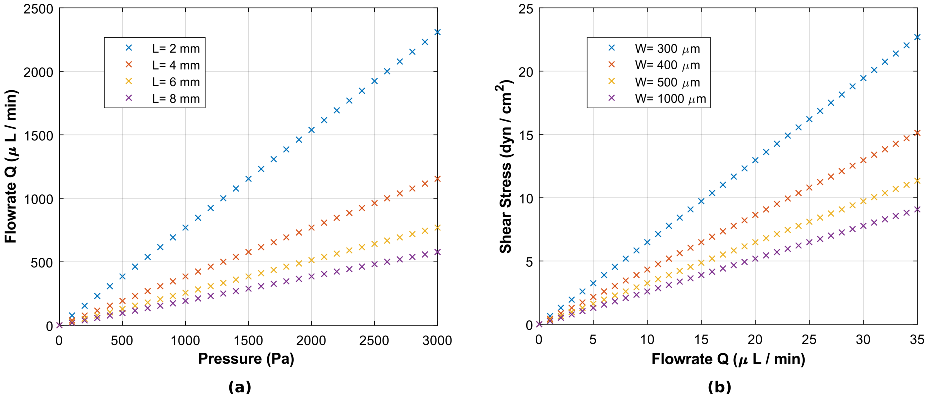

Figure 4.3: **(a)** Graph showing the relation between flowrate (Q) and pressure in four different microchannels with rectangular cross-section for four different values of channel length (L). **(b)** Graph showing the relation between shear stress and flowrate (Q) in four different microchannels with rectangular cross-section for four different values of channel width (W) for a fixed channel length (L).

Hence, the final design parameters aimed at minimizing as much as possible the hydraulic resistance while keeping the sheer stress under physiologically relevant ranges (1-6 dyn/cm^2) for pressure ranges of pressure-driven pumping systems [30–33]. Accordingly, the final values of width, length and height of the microchannels of the device were defined.

4.3.2. STRUCTURAL DESIGN

Besides the specifications for the microfluidic channel embedded in the thick polymeric layer, the entire chip, silicon cavity and, inlet and outlet ports were dimensioned according to the envisioned application and specially tuned for the initial biological validation.

CHIP SIZE AND MICROFLUIDIC PORTS

Among the design criteria determinant for the final dimensions of the device, its usability and compatibility with external hydraulic circuitry was considered. This is key to enable an entire system with high versatility and flexibility for most OOC applications. Thus, the possibility of interfacing the microfluidic channels with the silicon substrate was highly important to enable its hydraulic operation and its use with most pressure-driven and peristaltic pumping systems, commercially available adaptors and tubing for microfluidics [29, 34]. Such possibility was mainly enabled by the fabrication process developed, as through Deep Reactive Ion Etching (DRIE) it is possible to implement holes and cavities to access the microchannels located in the thick polymeric layer on the front side of the silicon chip.

In Figure 4.4a, a sketch illustrates the fluidic connection created between the microchannel and the silicon substrate for making the microenvironment accessible to external flow. The diameter of the cavities (D) acting as inlet and outlet ports was closely matched to the width of the microchannels($D = W = 400\ \mu$m), to minimize pressure drops given by changes in flow velocity.

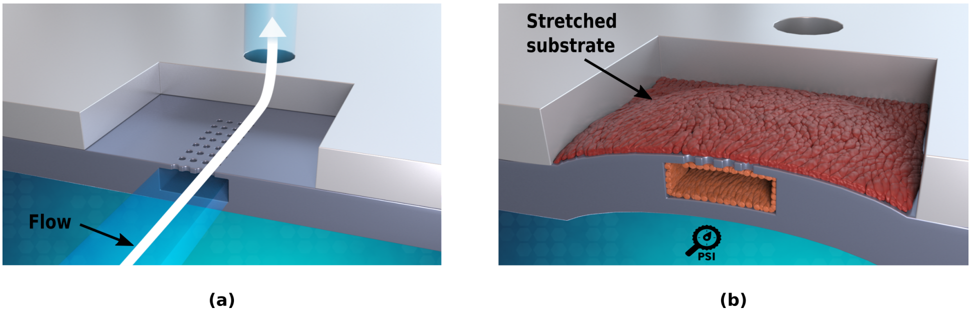

Figure 4.4: **(a)** A 3D sketch of the chip illustrating the microfluidic connection between the microchannel and the silicon substrate enabled by the fabrication method used. **(b)** A 3D sketch of the chip designed and specifically the silicon cavity that enables the allocation of a cell microenvironment and the releasing of the entire polymeric layer for mechanical stretching using pneumatic actuation.

Related to the above mentioned criteria, an additional constraint was introduced, i.e. the reduction of the device size, in the interest of producing a larger, and thus statistically more significant, number of devices per wafer, making possible to evaluate the yield of the fabrication process. Establishing a trade-off between mechanical stability of the device during the fabrication and manufacturability capabilities and given the envisioned first compatibility validation essays, a square die size of 1 cm by 1 cm was defined.

SILICON CAVITY

Likewise, by exploiting the capabilities enabled by the fabrication process, the chip was designed to accommodate more than one cell culture or co-culture. This was done by providing the device with a silicon cavity which is open and externally accessible (Fig. 4.4a). This makes possible having the two different cell cultures, in the cavity and inside the microchannel, potentially interfacing if necessary through the porous membrane. The ability to easily tune the size of such cavity contributes to adapt quickly the cell microenvironment to the required volumes for the cell medium and its continuous refreshing [35, 36].

Considering the die size defined (1 cm x 1 cm), the cavity dimensions and shape (square) were also defined defined in relation to the desired displacement of the membranes when strectched through pneumatic actuation (0 - 50 kPa). As Figure 4.4b illustrates, the cell culture in the silicon cavity might be stretched trough a pneumatic actuation system that can be coupled on the back of the device, as demonstraed in literature [14, 37]. Through this displacement, for instance, strain can be supplied to stem cells to assist the differentiation into cells normally found in tissues subjected to such a physical cue, such as in heart-on-chip or gut-on-chip as previously reported [14, 37–39]. The properties of the material used and specially the fabrication process employed gives a high versatility to the device in such matter.

Considering the equation relating the pressure and maximum displacement of a square membrane of side l, as

$$P = \frac{E}{(1-\nu)}\frac{t^3}{l^4}d\left[\frac{1}{12\alpha(1+\nu)} + C\frac{d^2}{t^2}\right] \tag{4.13}$$

Where t is the thickness of the membrane, E the Youngs Modulus of the material, ν the Poissons ratio, d the maximum displacement of the membrane, and $C = 21.62(1.41 - 0.292\nu)$ and $\alpha = 1.2610^{-3}$ constants suggested by literature [40–42]. Thus, the expected displacement for a pressure range of 1-50 kPa can be obtained for square membranes of different sizes, as depicted in figure 4.5a.

Moreover, with values obtained from Eq. 4.13, considering the deformation of the membrane to have a semicircular profile, and its final length (l_{final}) after deformation, the strain (s) was obtained as

$$s = \frac{l_{final} - l}{l} \tag{4.14}$$

Where (l_{final}) is given by

$$l_{final} = \frac{(l/2)^2 + d^2}{d} arcsin\left(\frac{ld}{(l/2)^2 + d^2}\right) \tag{4.15}$$

Thus, the expected strain for the same pressure range obtained is also depicted in Figure 4.5b.

Establishing a trade-off that maximizes all the mechanical and manufacturability capabilities of the device and given the envisioned applications, the cavity was created with a square shape dimensions of 3 mm by 3 mm. The dimensions also allow to maximize the volume and accessibility for cell seeding procedures and refreshing the medium to maintain the cell cultures viable. The envisioned displacements of the flexible polymeric substrate with such a design would give up to 13 % of strain for a pressure range (50 kPa) available in commeercial pneumatic pumps [43].

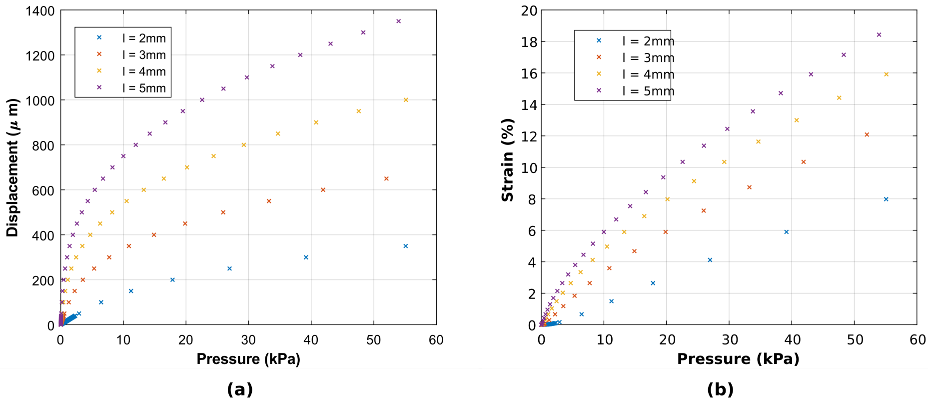

(a) **(b)**

Figure 4.5: **(a)** Displacement and **(b)** strain on squared-shape PDMS ($E = 1.2MPa$ and $v = 0.499$) membranes of a fixed thickness (200 μm) and different size (l) pneumatically actuated with pressure in the range of 1-50 kPa.

4.4. DEVICE MODELLING AND SIMULATION

A preliminary verification trough numerical simulations was done as part of the design process to explore the performance of the device in terms of fluid dynamics and mechanical stability. The microfluidic channels and the silicon chip with the dimensions defined in sections 4.3.1 and 4.3.2 were modelled and the corresponding solution to the set of equations obtained using the FEM-based software Comsol Multiphysics®. The modelling implemented was defined so that the corresponding set of equations to be computationally solved and the boundary conditions match the considerations taken of when deriving the analytical model.

4.4.1. FLUID FLOW

In the fluid flow investigations of the microchannels of the OOC device, a modelling module specifically made for solving the Navier-Stokes equations under steady state conditions was used. As a steady pressure-driven is meant to be used in practical experiments, time transient effects were not studied, reducing the system of equations to the same described by theory (Equations 4.3 and 4.4). With this set of equations establishing the proper mathematical model, the boundary conditions along with the material properties were considered. Water is employed as the fluid of interest, which appears in the set of equations through the variable of viscosity at 20 °C ($\eta = 1x10^{-3} Pa \cdot s$). Furthermore, the fluid behaviour was evaluated for different pressures using the inlet and outlet ports on the silicon chip as the fluid supply. A boundary condition of constant pressure along the extremes of the microchannels is introduced by including an inlet and outlet pressure in the corresponding surfaces. Such conditions are to be considered equivalent to the pressure difference (Δp) in Eqs 4.3-4.9).

In figure 4.6a, a schematic drawing with the boundary conditions established for the fluid flow, is shown. Inlet and outlet are under a constant pressure stimulus and the walls of the micro channels with a no-slip condition. Such non-slip condition properly defines constraint of zero velocity of the fluid at the walls, confining the fluid according to the structural dimensions of the microchannels [26, 28]. This conditions satisfies Equation 4.4.

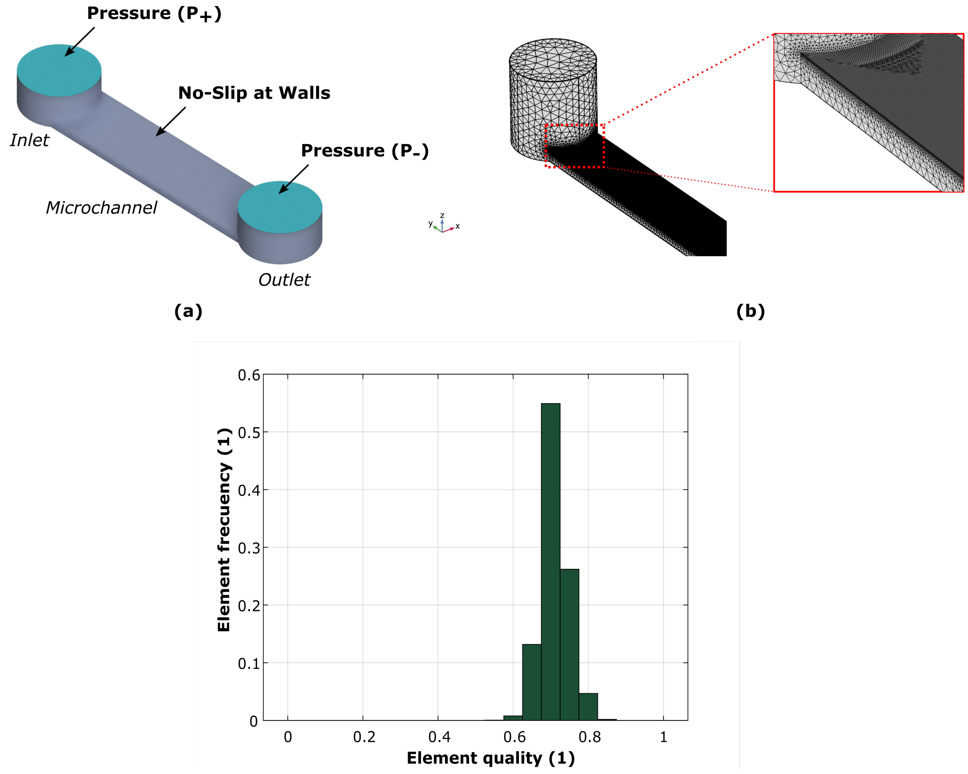

(a) **(b)**

(c)

Figure 4.6: **(a)** Boundary conditions for the fluid flow model of the microchannel. Pressure difference established in the inlet (P_+) and outlet (P_-). No-slip condition on the boundaries corresponding to the walls of the microchannels. **(b)** Geometry of the microchannel meshed with Comsol Multiphysics®. **(c)** The corresponding Histogram on the quality of meshing of the geometry for solving the fluid velocity field.

The geometry was then meshed with a highly dense (3.5 million elements) and average quality (≈ 0.7) mesh (Fig. 4.6b-c), providing the simulation environment with the sectioned elements of the microchannel to solve for the set of equations of the model proposed. The computation was then carried out obtaining the velocity field of each of the elements that integrate such meshed geometry.

For a pressure difference in the range of 2 kPa applied at the inlet and outlet of the device, a 3D sketch of the velocity field along cross sectional planes in the micro channel, is shown in Fig. 4.7a. The corresponding flowrates computed for a pressure difference range of 3kPa are shown in the curve of Fig. 4.7b. The theoretical curve based on the approximated equation is added for comparison. The approximation slightly deviates from the simulation results. Such difference might be given by not considering the effects of the sharp edges and corners close to the inlet and outlet of the silicon chip.

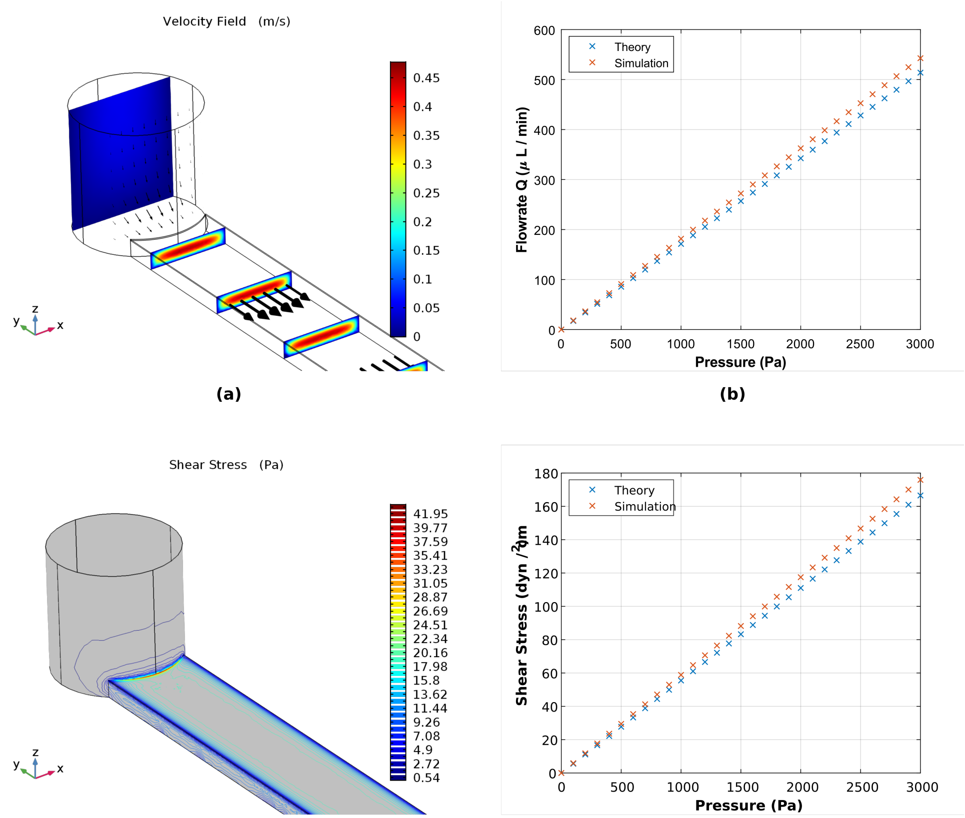

(a) **(b)**

(c) **(d)**

Figure 4.7: **(a)** Flow velocity field in four different cross sectional planes (*xz*) located along the microchannel length. A pressure difference of 2 kPa was applied to the specific case shown to induce the flow and illustrate the velocity field distribution. **(b)** The corresponding curve of the flowrates calculated for different pressures in the 0-3 kPa pressure range. **(c)** Shear stress calculated at the surface of the microchannel. A pressure difference of 2 kPa was applied to the specific case shown. **(d)** The corresponding curve of the shear stress obtained for different pressures in the 0-3 kPa pressure range.

Next, the shear stress was also investigated and specially on the surfaces of the channels, where according to theory the highest shear stress is to be found as a higher velocity gradient concentrates near to the walls. In such regions cells are expected to be located after cell culturing and subjected to such surface forces. The distribution of the shear stress along a microchannel for 2 kPa pressure difference is shown in Fig. 4.7c, while Figure 4.7d displays the shear stress as function of the pressure difference for a range of 3 kPa. This illustrates the convenience of using the dimensions defined for the microchannel, making posssible to supply the shear stress ranges suggested in literature for endothelial cells [30–33] at low pressures.

4.4.2. MECHANICAL BEHAVIOUR

Regarding, the mechanic behaviour of the thick polymeric layer embedding the microchannels, the modelling was done based on non-linear equations of solid mechanics. The non-linearity of the model is included to better approximate real behaviour by considering non-elastic properties of the polymeric material [44]. Hence in the model, the material properties were introduced throguh a stress-strain curve to include such non-linearity based on data reported in literature [44, 45]. Such relation is reproduced in Figure 4.8c. Furthermore, the Poisson ratio and Young Moduli values of 0.49 and 1.2 MPa, respectively, were introduced according to experimental data reported in literature [44–46].

The boundary conditions established for the model were determined based on the envisioned use of the device for mechanical stretching of cells cultured in the silicon cavity, such conditions can be observed in Figure 4.8a. A boundary condition of zero displacement was established on the parts not meant to experienced external forces, namely the walls of the device and silicon cavity. On the other side, a boundary force was established on the surface of the polymeric material meant to be stimulated by an external pneumatic pressure source.

Similarly to previous numerical model, the geometry was then meshed with dense (1.5 million elements) and average quality (≈ 0.65) meshing (Fig. 4.8b,d), providing the simulation environment with the sectioned elements of the microchannel to solve for the set of equations of the mechanical model. Once the model, meshing and boundary conditions were established, the computation was carried out for solving the displacement field of each of the elements of the geometry representing the device. In Figure 4.9a, the expected behaviour of the membrane displacement under stretching for different pneumatic actuation pressures, is shown. In figure 4.9b, a field is also depicted illustrating the superficial strain on the membranes comprising the area of the cavity meant for cell culturing.

As Figure 4.9 suggests, the design might allow mechanical stimulation of cell cultures given the flexibility of the membrane, which can be applied to stimulate cells as in *in vivo* conditions of certain physiological system in the human body (e.g. heart, gut, lungs). One of the biggest promises and currently under research is the effect mechanical stretching can induce or support on the specialization of iPSC-derived cardiomyocytes. Several groups are investigating this effect and recent results indicate that such mechanical cue could indeed enhance the maturation of such type of cells when subjected to a systematic and continuous stretching for a determined period of time [47–50].

4.5. DEVICE MICROFABRICATION

The fabrication of the device presented has been designed to follow a conventional top-down microfabrication process using numerous techniques of IC and MEMS technologies such as chemical vapor deposition, spin coating, wet and dry RIE etching, DRIE, among others [51, 52]. The high versatility of the device is mostly enabled by the use of these techniques, inherently suited for large scale fabrication and integration of sensing and stimulation [53, 54]. In Figure 4.10, the main steps of the process are shown.

The fabrication process is based on a last-polymer approach [14]. Initially, silicon oxide (SiO_2) is deposited on the front and back of a 100 mm-Si wafer by Plasma Enhanced

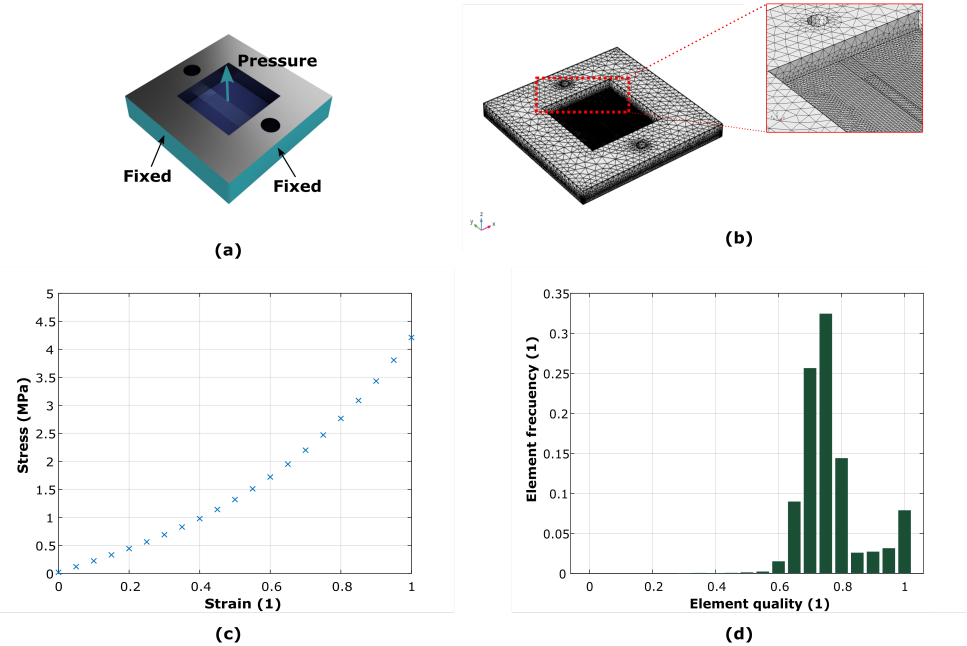

Figure 4.8: **(a)** Boundary conditions for the mechanical modelling of the device with non-linearity conditions on the material under mechanical stretching meant for mechanical stimulation of cells culture on the silicon cavity. The interior walls of the silicon cavity and the hold substrate are fixed through a zero velocity boundary conditions. The pneumatic stretching is provided to the model trough a boundary force conditions corresponding to a range of pressures available in most pneumatic pumping systems. **(b)** Geometry of the chip meshed with Comsol Multuphysics®. **(c)** Stress-strain curved used to include the non-linear effects of the polymeric material embedding the micro channels. The curve is based on data reported in literature [44]. **(d)** The corresponding Histogram on the quality of meshing of the geometry for solving the displacement and strain fields.

Chemical Vapour Deposition (PECVD). A 1 μm-thick PECVD SiO_2 is deposited on the front side of the wafer (Fig. 4.10a). A 6 μm-thick SiO_2 is used for the back as masking layer and patterned with conventional lithography and dry etching, defining the square corresponding to the silicon cavity for cell culture and the inlet and outlet ports of the microfluidic channel (Fig. 4.10b). Subsequently, a first Polydimethilsiloxane (PDMS) layer is deposited by two-step spin coating, the first spreading step at 300 rpm and the second step at 6000 rpm (Fig. 4.10c). The spinning time was tuned to achieve the desired layer thickness [55]. A layer of 8 μm was determined as optimal for the first prototypes and achieve the features sizes needed. The PDMS is cured at 90 °C for 1 h.

Then, an aluminium (Al) layer, used as hard mask is sputtered on the PDMS surface(Fig. 4.10d). As previously seen for the porous membranes, by including such a Al layer, the lithography process is optimized and mechanical and uniformity issues introduced by thermal coefficient mismatch and surface topography are prevented. The layer is was deposited and patterned with proximity exposure as described in the process of the porous membranes. Depending on the application such patterning can be used to defined porous interfaces to mimic biological barriers and to enable the fluid

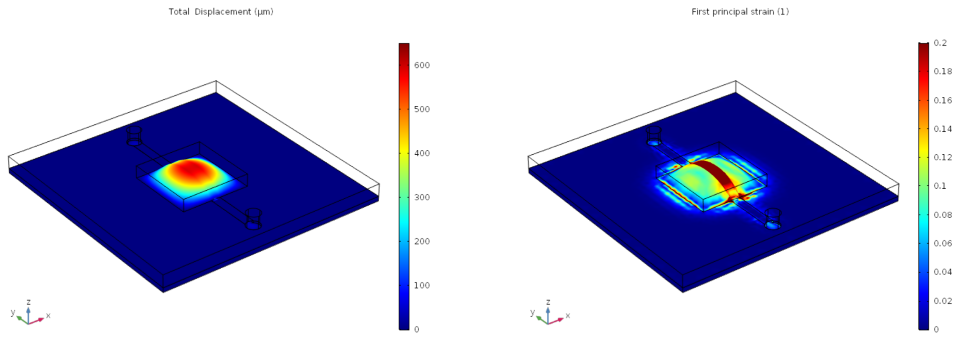

(a) **(b)**

Figure 4.9: **(a)** Displacement field obtained for the device after computation and solving the non-linear equations to study the mechanical behaviour of the polymeric material under pneumatic actuation. The pressure applied as boundary force in this particular case correspond to 5 kPa. **(b)** Strain field on the surface of the polymeric material on the bottom of the silicon cavity of the device meant for cell culturing. The pressure applied as boundary force in this particular case correspond to 5 kPa.

connection of the inlet and outlet cavities in the silicon with the microchannel or the silicon cavity, depending on the envisioned OOC application. The PDMS is etched by reactive-ion etching (RIE) (Gases: CH_4, SF_6, O_2, P: 20 mTorr, RIE Bias: 20 W, ICP Power: 500W) in an ICP plasma etcher [56–58]. The etching conditions were optimized to obtain anisotropic etching, so to accurately control shape and size of the pores, inlet and outlet. A sacrificial layer (PAA or PR) is deposited on the first patterned PDMS layer. The baking conditions were tuned to avoid as much as possible the mechanical rupture or high degassing as now a thick layer ($> 50\mu$m) is necessary to realize the structures with high aspect ratio. Such structures correspond to the height (h) of the microchannel. Layers between 20 μm and 200 μm were deposited and patterned with a high degree of control. For preliminary tests of the OOC device, a 90 μm thick layer was used to define the height of the microchannel according to the design criteria previously detailed and simulation validation (Section 4.3.1). The Al hard mask is removed by wet etching using a buffered solution (PES) of acetic acid, nitric acid and hydrofluoric acid (Fig. 4.10e)

Subsequently, a second PDMS layer is deposited with a thickness of approximately 200 μ by a one-step spin coating at 300 rpm (Fig. 4.10f). Adhesion issues were not present after this step since the bonding force ($\simeq 670kPa$) has been demonstrated to be high between cured PDMS and uncured PDMS [59–61].

Subsequently, the silicon substrate is etched from the backside by Deep Reactive Ion Etching (DRIE) using a Bosh-based process [51], allowing to open the silicon cavity for cell culture and the microfluidic inlets and outlets in the silicon substrate. The oxide stop layer initially deposited on the front side is removed by wet etching (Fig. 4.10g). Finally, the sacrificial and Al layer used to define structurally the microchannels is removed or dissolved using an optimized wet etching process employing PES and Dimethyl sulfoxide (DMSO), with a subsequent thorough rinsing in water to remove any possible residue.

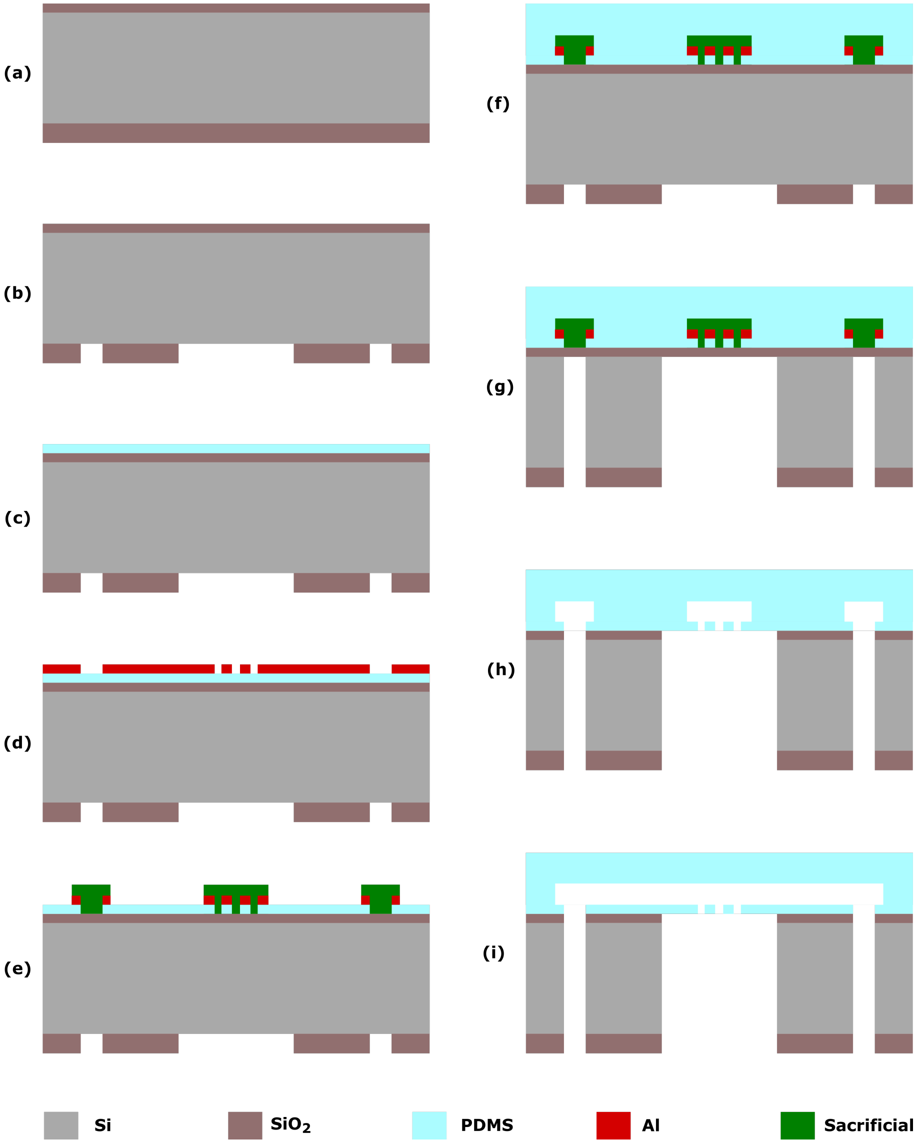

Figure 4.10: Main steps of the fabrication process of the fully micro fabricated Organ-on-CHip device. **(a)** Deposition of oxide on front and back. **(b)** Patterning of the oxide on the back for defining the membrane opening or culture macro chamber size. **(c)** Deposition of first layer of PDMS. **(d)** Deposition of masking layer to define porous membrane, inlet and outlet or additional microfluidic ports. **(e)** Dry etching of the PDMS layer, deposition and patterning of sacrificial layer and removal of Al. **(f)** Deposition of second PDMS layer (thicker). **(g)** Etching of the silicon substrate from the back to open inlet and outlet. **(h)** Removal of the sacrificial layer and Al through wet etching (releasing of the channels). **(i)** Removal of the sacrificial layer seen from a different perspective [19].

4.6. DEVICE CHARACTERIZATION

Several experiments were carried out to verify and characterize the mechanical stability of the microstructures and the response of the device under similar operating conditions of the envisioned OCC application. These was done by inspecting the features of the device trough optical and scanning electronic microscopy (SEM) and by coupling the device to an hydraulic circuit and a pneumatic system for validating the fluid flow characteristics and the stretching capabilities.

4.6.1. OPTICAL AND SEM MICROSCOPY

The structural features of the microchannel and the chip were inspected with optical and electron microscopy (SEM) during and after the fabrication process. The microchannels were shown to be fully open and the porous interfacing with the microchamber as well. Special attention was paid to make sure that both inlet and outlet of the microfluidic system were completely accessible and open.

Figure 4.11 shows several images taken in different areas (Fig.4.11a) of the device inspected during and after fabrication. Figure 4.11b shows a top view and close up illustrating the two types of materials comprising the device; the silicon substrate and the suspended polymeric layer with embedded microchannels. In Figure 4.11b, a zoom out of the device shows a top view of the inlet/outlet port in correct alignment to the microchannel. In Figure 4.11c, optical images show the porous surface meant to interface the micro channel and the silicon cavity.

In Figure 4.12, SEM images show the cross section of the microchannels embedded in the thick PDMS layer after stripping the sacrificial layer and etching the silicon cavity. Once the sacrificial layer is removed, and silicon cavity and inlet and outlet ports etched through by DRIE, the device was carefully diced to inspect its cross section and measure the final features realized, especially for the microchannel (Fig. 4.12i-ii). Several images were taken with different view angles (Fig. 4.12a-c), demonstrating the successful fabrication of the features as established by the design. The device shown in the second column was manually cut to inspect further the inside of the micro channel. By doing so, it was possible to evaluate and confirm the successful complete removal the sacrificial layer, without any residue left.

4.6.2. MICROFLUIDIC PERFORMANCE

The interface between the rigid substrate (silicon) and the microchannels enables the microfluidic connection of the device with the exterior. However, the device can not be directly used with commercially available microfluidics and cell culturing tools. The small size of the complete device and its micro-scale features are not the adequate for its manually handling and fluidic coupling to perform fluid performance characterization and cell culturing. Hence, an external coupling module was developed to make accessible the microchannels and the silicon cavity. The module has been also designed to allocate the right amount of medium for feeding and refresh the cell culture. As can be seen in the sketch of Figures 4.13a, the chip is sandwiched between two custom made substrates (*top and bottom*) guaranteeing the sealing of the inlet, outlet and the silicon cavity. Thus, enabling fluidic connection to external hydraulic circuitry components through generic microfluidic ports. Figure 4.13b show images of the actual module.

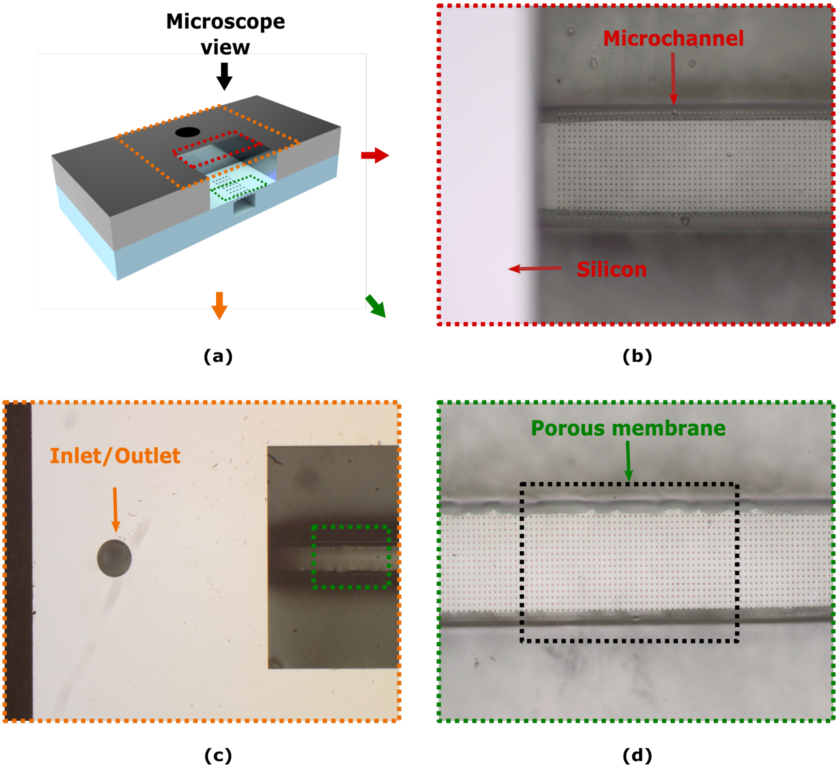

Figure 4.11: **(a)** Different perspectives for the optical inspection of the microfabricated device for OOC applications. **(b)** Top view of one section of the device (red dashed line) illustrating the two types of substrates comprising the microfabricated device. **(c)** Top view of half the device illustrating the etched through cavity designed as inlet and outlet ports for accessing the microchannel embedded in the polymeric thick substrate. **(d)** A zoom in on the silicon cavity to inspect the microchannel and the porous surface meant to interface cell microenvironments.

In Figure 4.14a, the schematic of the hydraulic connection made with the help of the interface developed to investigate and verify the fluid behaviour is depicted. The microfabricated OOC chip was coupled to a flow source and a flow-rate sensor with the possibility of having a closed loop on either the flowrate or pressure applied to the inlet of the device. The corresponding equivalent hydraulic circuit is given in Figure 4.14b and a picture of the whole measurement set-up is shown in Figure 4.14c.

Once the the hydraulic circuitry was confirmed to operate leak-free, the behaviour of the fluid flow in the device was characterized to determine the flowrate and shear stress. The flowrate-pressure curve was first obtained for the hydraulic circuit comprising the tubing and the interface module using an element with a known hydraulic resistance. Then, the device was added and its flowrate-pressure relation obtained indirectly considering the equivalent circuit. In Figure 4.15a, the indirectly obtained experimental data along with theoretical and simulation calculations are plotted. The device allow to have wide range of flowrate values (up to 400 $\mu L/min$) for a pressure range of 3 kPa.

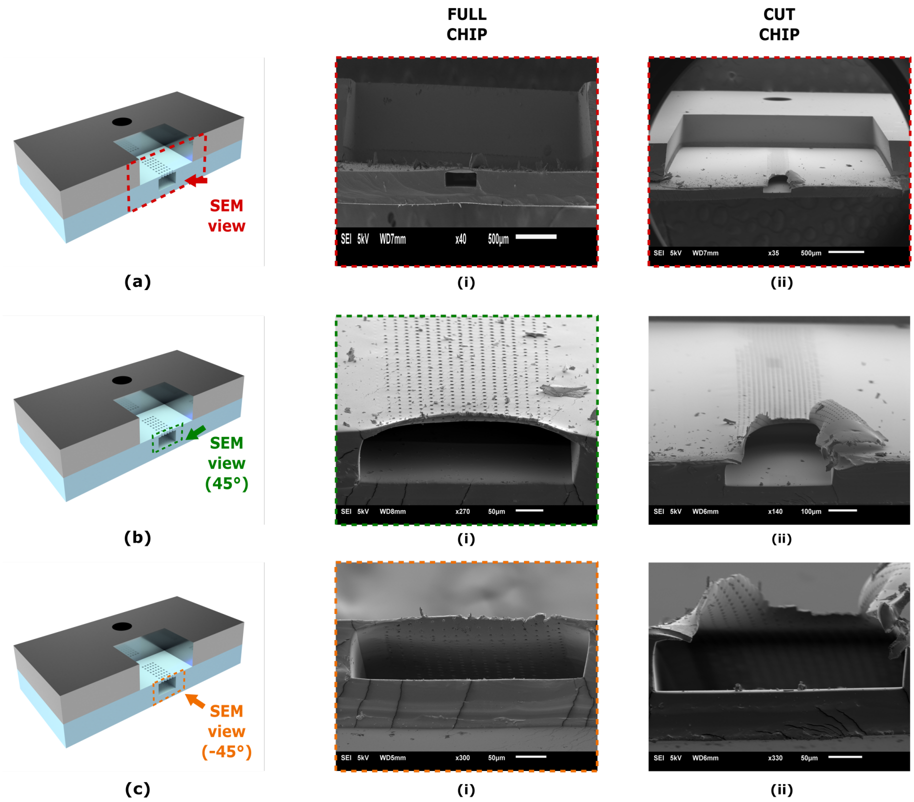

Figure 4.12: **(a)** SEM images of half devices for inspecting cross section. Two samples are shown: **(i)** whole device and **(ii)** manually cut device to investigate the inside of the microchannel. **(b)** SEM images of cross sections for samples tilted 45° upward: **(i)** whole device and **(ii)** manually cut device. **(c)** SEM images of cross sections for samples tilted 45° downward: **(i)** whole device and **(ii)** a manually cut device.

The experimental sheer rate is also shown in Figure 4.15b together with the calculated theoretical value and obtained through simulation. For the same pressure range the shear stress covers a wide range of values (0 - 140 dyn/cm^2). However, for the envisioned application the operational pressure range necessary is below 500 Pa, and the corresponding shear stress is below 20 dyn/cm^2. Thus, the device designed and the sealing interface along with commercially available pressure-driven pumping systems provide a system potentially able to supply a wide range of shear stresses to cells cultured inside the microchannels for supplying physiologically relevant stimulation.

4.6.3. MECHANICAL PERFORMANCE

To validate the mechanical stimulation to the cell micro environment, especially for cell cultures in the silicon cavity, a preliminary test for the stretching of the flexible material was carried out. The test was also done by applying pressure on the back of the device trough a pneumatic pressure pumping system.

To do such test, a special interface designed for coupling the device to the pumping

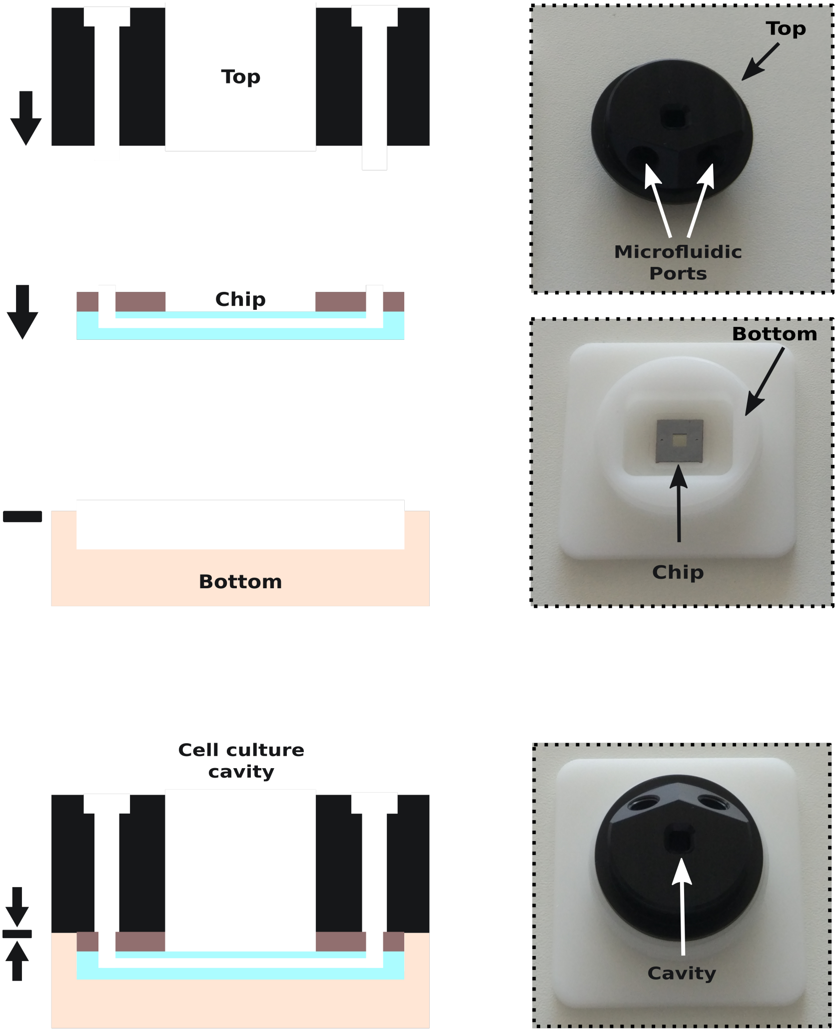

(a) **(b)**

Figure 4.13: **(a)** A sketch of the module used to interface the inlet and outlet ports of the device with external hydraulic circuitry components. A two-part module is used to sandwich the device for proper sealing and enable cell culturing in the silicon cavity. **(b)** Images of the actual module enabling microfluidic connection and cell culture in the fabricated device.

system was used. By actuating through a pneumatic pump it is possible to stimulate mechanically a flexible polymeric substrate [14]. The mechanical stimulus can thus be translated as strain at the surface of the material. For the microfabricated device, the strain can be approximated based on the maximum displacement of the center of the suspended thick polymeric layer.

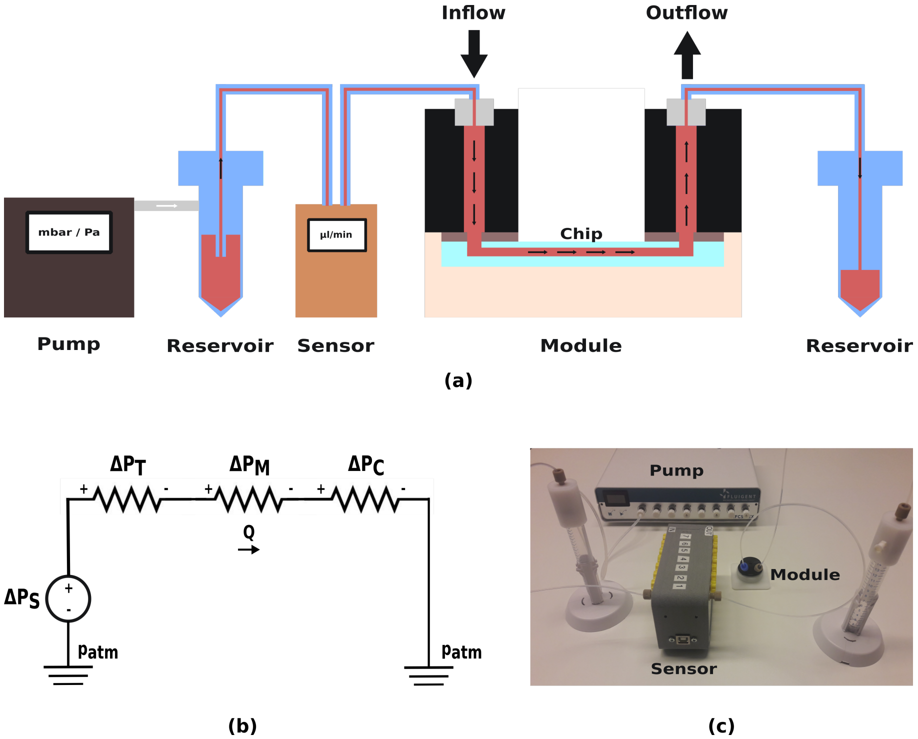

Figure 4.14: **(a)** A schematic drawing of the connection for the microfabricated OOC device to the hydraulic circuitry through the module designed. **(b)** Equivalent hydraulic circuit of the measurement set-up used for characterization of the flow behaviour. The pressure drop of the tubing (P_T), the module (P_M) and the microfabricated device (P_C) are shown, corresponding to their respective hydraulic resistance. **(c)** An image of the entire measurement set-up.

In Figure 4.16a-b, a schematic and a picture of the set-up used to determine experimentally the displacement of the suspended polymeric membrane under pneumatic actuation, is shown. The pneumatic actuation was set to sweep the pressure in the rage of 1-20kPa and the maximum displacement on the suspended layer measured optically based on the change of the focal point of the image. In Figure 4.16c, the values for displacement in relation to the pressured applied are shown. The profile of displacement on the membrane allocating the microfluidic channels is close to what is expected according to the design selected and the validation obtained previously from simulations.

In Figure 4.16d, the experimental data obtained indirectly on the strain is shown. This can be related trough the equations given in section 4.3.2 to estimate the approximate strain expected to be supplied to any cell culture in the silicon cavity. The displacement and strain curves shows the capability of the device to provide mechanical stimulation to cell cultured in the surface of the polymeric layer allocated in the silicon cavity. The strain provided (0 - 10 %) is within the range suggested by literature as physiological relevant in applications such as heart cells maturation [48–50].

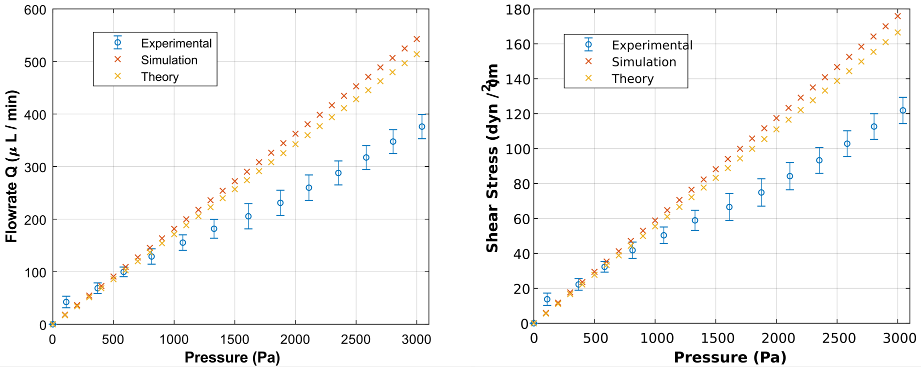

(a) **(b)**

Figure 4.15: **(a)** Flowrate-Pressure response and **(b)** Shear stress-Pressure response of the microfabricated device for OOC applications. The theoretical (Red) and modelled (Yellow) data are included for comparison with the experimental data (Blue).

4.7. HUVEC AND CARDIOMYOCYTES CULTURING

After investigating and characterizing the fluidic performance of the microfabricated device, an initial biological validation was conducted aiming at assesing the biocompatibility of the device to culture cells in the microchannels and the silicon cavity. To do so, two different cell types were used, human umbilical vein endothelial cells (HUVECs) and cardiomyocytes (CM). The initial results presented comprehend the first stage towards implementing OOC models using the microfabricated device for hear-on-chip including structures replicating microvasculature.

To culture cells inside the microchannel, the devices are treated prior starting the cell culturing procedure to remove any residue and possible sources of infection. To do so, the device is properly sterilized and treated by using ethanol and UV light, respectively. Subsequently, the surface of the microchannel is funcionalized to promote the adhesion of the endothelial cells to the walls, top and bottom of the microstructures. Prior to cell seeding, the coating or material for promoting the cell growth and layer formation is added. Either Fibronectin or Collagen can be used for such a purpose [62, 63]. Here, fibronectin was used and baked at low temperature (37 °C) for two hours to enhance the formation of a ECM-like structure.

The devices are then rinsed thoroughly to eliminate the remaining adhesion promoter and proceed with the seeding of the cells. HUVEC are obtained from a confluent flask and spin down for determining the cell density to culture inside the microchannel. A density of approximately 20x10^{6}cells/mL^{-1} was used and the cells pipetted into the device. Cells were attached by incubating the chips overnight at 37 °C with 5% CO$_2$. After that, non-attached cells were washed away by flushing the microchannels with fresh EGM-2 [21, 64]. The silicon cavity was filled with EGM-2 to prevent drying. Medium in both microchannels was refreshed twice daily by pipetting fresh EGM-2. In Figure 4.17c, bright field optical images show endothelial cells grown in the microchannel of the device. The corresponding staining for florescence imaging was done to investigate the

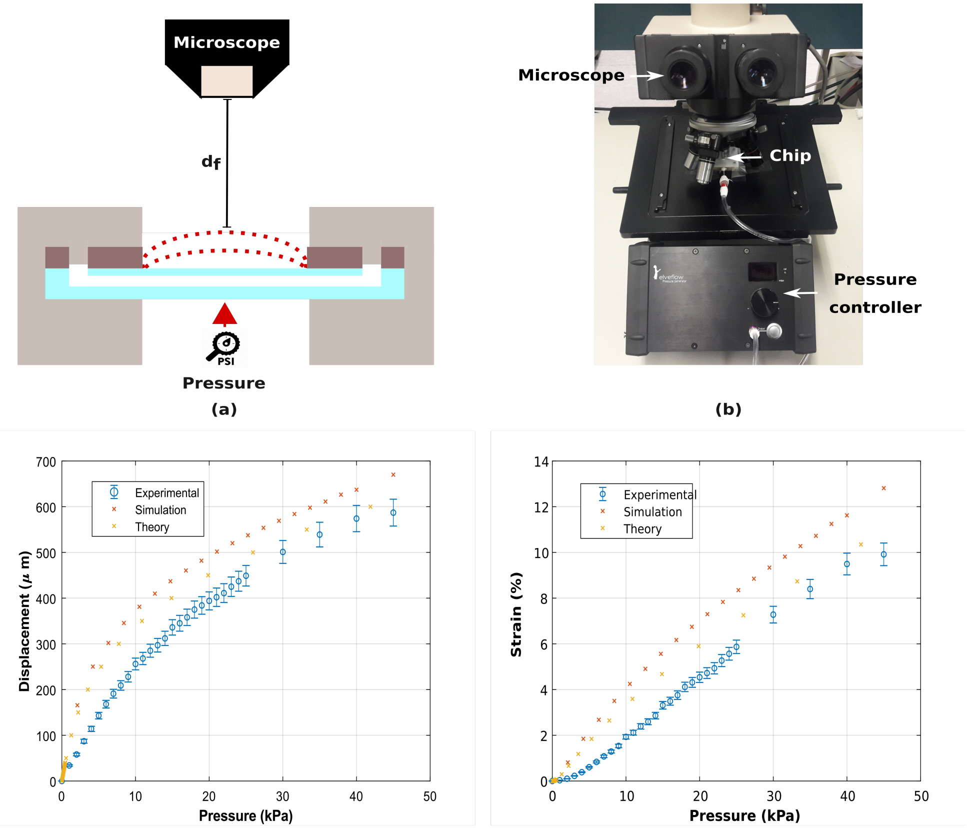

(c) (d)

Figure 4.16: **(a)** A schematic drawing of the set-up used to estimate the displacement of the thick polymeric layer of the microfabricated device for OOC applications. **(b)** Optical image of the actual set-up and pneumatic pumping system used to actuate the polymeric layer. **(c)** Displacement in the center of the suspended polymeric layers measured optically for different pressures set through the pumping system. **(d)** Estimation of the strain of the suspended polymeric layer based on the displacement measurements.

physiological state of the cells and confirm layer formation. Figure 4.17e shows a florescent image confirming healthy morphology of the cells and the tendency of the cells towards a monolayer formation.

As shown in the bright field and florescence image in Figure 4.17d-f, cardiomyocytes were also cultured on the device. The culturing of the cardiomyocytes was done specifically in the silicon cavity of the microfabricated OOC device. The devices were sterilized with ethanol previous to its adhesion coating and seeding of the cells. The thick suspended polymeric layer inside the silicon cavity was then coated with fibronectin. Upon cell seeding, density of approximately $10x10^6$cells/mL^{-1} was used and the cells pipetted in the silicon cavity and incubated at 37 °C with 5% CO_2 for seven days. The cell culture was refreshed on day 2 and 4 with 0.2 ml with medium. The cells presented the morphology expected and physiologically active as calcium flow activity was observed.

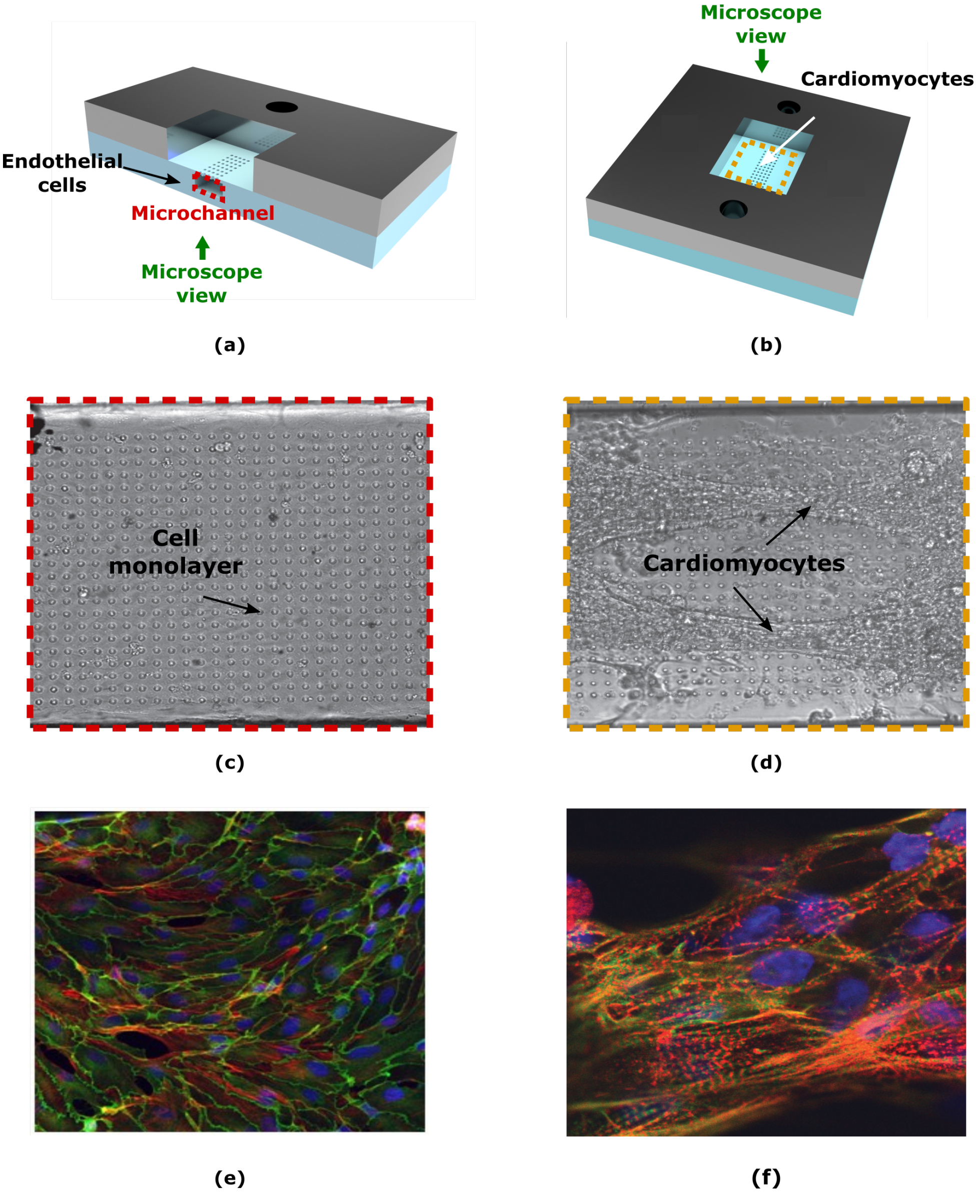

Figure 4.17: **(a-b)** A sketch of the device to illustrate the perspective of the images taken for cells cultured inside the microchannel and the silicon cavity, respectively. **(c-d)** Bright field optical images of HUVEC cells and cardiomyocytes cultured inside the microchannel and the silicon cavity, respectively. **(e-f)** Florescent optical images of HUVEC cells and cardiomyocytes cultured inside the channel and in the silicon cavity, respectively.

4.8. DISCUSSION AND CONCLUSIONS

The microfabricated device presented here has been developed envisioning a variety of Organ-on-Chip applications. The specific design of the microchannels is meant to enable the possibility of having microstructures for perfusion. This closer mimicking of the microvasculture will contribute to investigate further biological mechanisms and diseases using in *in vitro* models with higher physiological relevance and higher manufacturability capabilities.

The silicon cavity allows to interface potential microvasculature with a complementary cell culture with the advantage of having such cavity open and easily accessible to the user, unlike most OOCs reported in literature, which normally are composed of two or more close compartments only accessible through inlets and outlets. At the same time, this also allows the culturing of not only cell layers but also tissues, which normally are bigger than the limited sized compartments reported in literature [9, 65]. The size of the cavity is not limited as it is open to the environment, making possible to allocate for instance, tissue slices and organoids. Very often these tissues and cell aggregates are used to carry out studies investigating brain activity, muscular diseases and cancer [66–69]. Normally, such biological formations have dimensions with thickness up to 2000 μm and length up to 5000 μm, which would not be possible to implement with most devices with limited height, a consequence of compartmentalization enabled by glass technologies and soft lithography process. In Figure 4.18, a 3D sketch helps to illustrate several OOC models that might be developed with the microfabricated device involving the recreation of a barrier, co-culture and the possibility of including a perfusion replicating microvasculature.

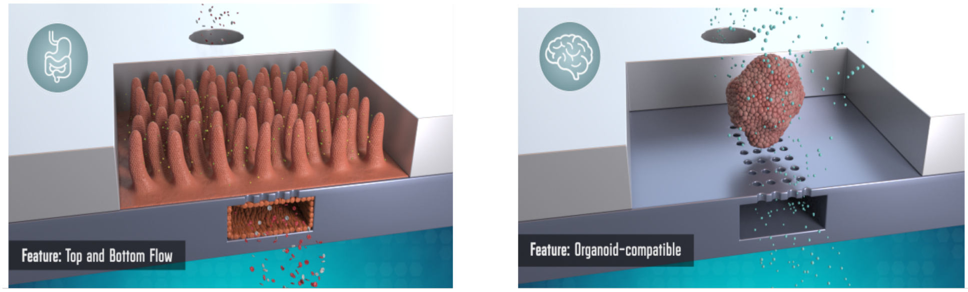

(a) (b)

Figure 4.18: A sketch showing the versatility of the microfabricated device for OOC applications in enabling different potential disease models. **(a)** An organoid for brain cells study cultured in the silicon cavity of the microfabricated device with the microchannels enabling the introduction of perfusion for replicating microvasculature and **(b)** A cancer-on-chip model comprising a tumor tissue slice taken from a patient and maintained in the silicon cavity of the device and continuously perfused through the microchannel.

The interface developed to connect the chip to external hydraulic circuitry is easy to use and compatible with standard microfluidic connectors and tubing, which facilitates the adoption of the whole system for research and commercial applications. However, further work is necessary to enable its use in the drug development pipeline, such as validation with other cell lines and demonstrating the advantages over other devices.

REFERENCES

[1] K. I. Budhwani, V. Thomas, and P. Sethu, *Lab-on-a-brane: Nanofibrous polymer membranes to recreate organ-capillary interfaces,* Journal of Micromechanics and Microengineering **26** (2016), 10.1088/0960-1317/26/3/035013.

[2] J. S. Choi, Y. Piao, and T. S. Seo, *Fabrication of various cross-sectional shaped polymer microchannels by a simple PDMS mold based stamping method,* Biochip Journal **6**, 240 (2012).

[3] V. Pensabene, L. Costa, A. Y. Terekhov, J. S. Gnecco, J. P. Wikswo, and W. H. Hofmeister, *Ultrathin Polymer Membranes with Patterned, Micrometric Pores for Organs-on-Chips,* ACS Applied Materials and Interfaces **8**, 22629 (2016).

[4] D. M. Ornoff, Y. Wang, and N. L. Allbritton, *Characterization of freestanding photoresist films for biological and MEMS applications,* Journal of Micromechanics and Microengineering **23**, 025009 (2013).

[5] K. Ryu and C. Liu, *Precision patterning of PDMS thin films: a new fabrication method and its applications,* Micro Total Analysis Systems 2002 , 1 (2002).

[6] A. Queval, N. R. Ghattamaneni, C. M. Perrault, R. Gill, M. Mirzaei, R. A. McKinney, and D. Juncker, *Chamber and microfluidic probe for microperfusion of organotypic brain slices,* Lab Chip **10**, 326 (2010).

[7] D. Kim, X. Wu, A. T. Young, and C. L. Haynes, *Microfluidics-Based in Vivo Mimetic Systems for the Study of Cellular Biology,* Accounts of Chemical Research (2015).

[8] T. Das and S. Chakraborty, *Perspective: Flicking with flow: Can microfluidics revolutionize the cancer research?* Biomicrofluidics **7**, 11811 (2013).

[9] S. N. Bhatia and D. E. Ingber, *Microfluidic organs-on-chips.* Nature biotechnology **32**, 760 (2014).

[10] J. A. Brown, V. Pensabene, D. A. Markov, V. Allwardt, M. Diana Neely, M. Shi, C. M. Britt, O. S. Hoilett, Q. Yang, B. M. Brewer, P. C. Samson, L. J. McCawley, J. M. May, D. J. Webb, D. Li, A. B. Bowman, R. S. Reiserer, and J. P. Wikswo, *Recreating blood-brain barrier physiology and structure on chip: A novel neurovascular microfluidic bioreactor,* Biomicrofluidics **9** (2015), 10.1063/1.4934713.

[11] A. K. H. Achyuta, A. J. Conway, R. B. Crouse, E. C. Bannister, R. N. Lee, C. P. Katnik, A. A. Behensky, J. Cuevas, and S. S. Sundaram, *A modular approach to create a neurovascular unit-on-a-chip,* Lab Chip **13**, 542 (2013).

[12] B. Jiang, W. Zheng, W. Zhang, and X. Jiang, *Organs on microfluidic chips: A mini review,* Science China Chemistry **57**, 356 (2013).

[13] Y. Ghallab and Y. Ismail, *CMOS Based Lab-on-a-Chip: Applications, Challenges and Future Trends,* Circuits and Systems Magazine, IEEE , 27 (2014).

[14] S. Khoshfetrat Pakazad, a. Savov, a. van de Stolpe, and R. Dekker, *A novel stretchable micro-electrode array (SMEA) design for directional stretching of cells,* Journal of Micromechanics and Microengineering **24**, 034003 (2014).

[15] A. Gaitas, R. Malhotra, T. Li, T. Herron, and J. Jalife, *A device for rapid and quantitative measurement of cardiac myocyte contractility,* Review of Scientific Instruments **86** (2015), 10.1063/1.4915500.

[16] P. Ertl, D. Sticker, V. Charwat, C. Kasper, and G. Lepperdinger, *Lab-on-a-chip technologies for stem cell analysis.* Trends in biotechnology **32**, 245 (2014).

[17] Q. Hamid, C. Wang, Y. Zhao, J. Snyder, and W. Sun, *A three-dimensional cell-laden microfluidic chip for in vitro drug metabolism detection.* Biofabrication **6**, 025008 (2014).

[18] N. Gaio, C. Silvestri, B. Van Meer, S. Vollebregt, C. L. Mummery, and R. Dekker, *Fabrication and Characterization of an Upside-Down Carbon Nanotube Microelectrode Array,* IEEE Sensors Journal **16**, 8685 (2016).

[19] N. Gaio and W. Quiros Solano, *Versatile 3D Stretchable Micro-Environment for Organ-on-Chip Devices Fabricated with Standard Silicon Technology,* (2017).

[20] A. Kobuszewska, E. Tomecka, K. Zukowski, E. Jastrzebska, M. Chudy, A. Dybko, P. Renaud, and Z. Brzozka, *Heart-on-a-Chip: An Investigation of the Influence of Static and Perfusion Conditions on Cardiac (H9C2) Cell Proliferation, Morphology, and Alignment,* SLAS Technology **22**, 536 (2017).

[21] E. Giacomelli, M. Bellin, L. Sala, B. J. V. Meer, L. G. J. Tertoolen, V. V. Orlova, and C. L. Mummery, *Three-dimensional cardiac microtissues composed of cardiomyocytes and endothelial cells co-differentiated from human pluripotent stem cells,* Human Development , 1008 (2017).

[22] T. Iwamiya, K. Matsuura, S. Masuda, T. Shimizu, and T. Okano, *Cardiac fi broblast-derived VCAM-1 enhances cardiomyocyte proliferation for fabrication of bioengineered cardiac tissue,* Regenerative Therapy **4**, 92 (2016).

[23] Y. K. Kurokawa and S. C. George, *Tissue engineering the cardiac microenvironment : Multicellular microphysiological systems for drug screening ,* Advanced Drug Delivery Reviews **96**, 225 (2016).

[24] Y. S. Zhang, J. Aleman, A. Arneri, S. Bersini, S. R. Shin, M. R. Dokmeci, A. Khademhosseini, and S. Arabia, *HHS Public Access,* Biomedical Materials **10** (2016), 10.1088/1748-6041/10/3/034006.From.

[25] V. Talman and R. Kivelä, *Cardiomyocyte Endothelial Cell Interactions in Cardiac Remodeling and Regeneration,* Frontiers in Cardiovascular Medicine **5**, 1 (2018).

[26] F. White, *Fluid Mechanics (Mcgraw-hill Series in Mechanical Engineering)* (McGraw-Hill Science/Engineering/Math, 2010).

[27] Y. Nakayama, *Introduction to Fluid Mechanics* (Butterworth-Heinemann, 1999).

[28] H. Bruss, *Microscale Acoustofluidics* (Royal Society of Chemistry, 2014).

[29] K. W. Oh, K. Lee, and E. P. Furlani, *Design of pressure-driven microfluidic networks using electric circuit analogy,* Lab Chip , 515 (2012).

[30] D. A. Chistiakov, A. N. Orekhov, and Y. V. Bobryshev, *Effects of shear stress on endothelial cells: go with the flow,* Acta Physiologica **219**, 382 (2017).

[31] H. S. Shin, *Shear Stress Effect on Transfection of Neurons Cultured in Microfluidic Devices,* Journal of Nanoscience and Nanotechnology **9**, 7330 (2009).

[32] R. Booth and H. Kim, *Characterization of a microfluidic in vitro model of the blood-brain barrier (μBBB),* Lab on a Chip **12**, 1784 (2012).

[33] B. Prabhakarpandian, M.-C. Shen, J. B. Nichols, I. R. Mills, M. Sidoryk-Wegrzynowicz, M. Aschner, and K. Pant, *SyM-BBB: a microfluidic blood brain barrier model,* Lab on a Chip **13**, 1093 (2013).

[34] Y. Temiz, R. D. Lovchik, G. V. Kaigala, and E. Delamarche, *Microelectronic Engineering Lab-on-a-chip devices : How to close and plug the lab ?* MICROELECTRONIC ENGINEERING **132**, 156 (2015).

[35] Y. Yoshimura, T. Kikuiri, and T. Hasegawa, *How much medium do you use for cell culture ? Medium volume influences mineralization and osteoclastogenesis in vitro,* Molecular Medicine Reports **i**, 429 (2017).

[36] A. Haque, P. Gheib, Y. Gao, E. Foster, K. J. Son, J. You, G. Stybayeva, D. Patel, and A. Revzin, *Cell biology is different in small volumes : endogenous signals shape phenotype of primary hepatocytes cultured in microfluidic channels,* Scientific Reports , 1 (2016).

[37] N. Gaio, B. V. Meer, W. Q. Solano, L. Bergers, A. V. D. Stolpe, C. Mummery, P. M. Sarro, and R. Dekker, *Cytostretch , an Organ-on-Chip Platform,* Micromachines , 1 (2016).

[38] H. J. Kim and D. E. Ingber, *Gut-on-a-Chip microenvironment induces human intestinal cells to undergo villus differentiation.* Integrative biology : quantitative biosciences from nano to macro **5**, 1130 (2013).

[39] P. Linder, J. Trzewik, M. Rüffer, G. M. Artmann, I. Digel, R. Kurz, a. Rothermel, a. Robitzki, and a. Temiz Artmann, *Contractile tension and beating rates of self-exciting monolayers and 3D-tissue constructs of neonatal rat cardiomyocytes,* Medical and Biological Engineering and Computing **48**, 59 (2010).

[40] A. Chouaf, C. Malhaire, M. L. Berre, M. Dupeux, F. Pourroy, and D. Barbier, *Stress analysis at singular points of micromachined silicon membranes* (Elsevier Science, 2000) pp. 109–115.

[41] V. A. Gridchin, V. V. Grichenko, and V. M. Lubimsky, *Square-Membrane Deflection and Stress : Identifying the Validity Range of a Calculation Procedure,* Rusian Microelectronics **34**, 210 (2005).

[42] S. Timoshenko and S. Woinowsky-Krieger, *Theory of Plates and Shells, (Engineering Societies Monographs)* (McGraw-Hill College, 1959).

[43] J. De Jong, R. G. Lammertink, and M. Wessling, *Membranes and microfluidics: A review,* Lab on a Chip **6**, 1125 (2006).

[44] T. K. Kim, J. K. Kim, and O. C. Jeong, *Microelectronic Engineering Measurement of nonlinear mechanical properties of PDMS elastomer,* Microelectronic Engineering **88**, 1982 (2011).

[45] I. D. Johnston, D. K. McCluskey, C. K. L. Tan, and M. C. Tracey, *Mechanical characterization of bulk Sylgard 184 for microfluidics and microengineering,* Journal of Micromechanics and Microengineering **24**, 035017 (2014).

[46] F. Schneider, J. Draheim, R. Kamberger, and U. Wallrabe, *Physical Process and material properties of polydimethylsiloxane (PDMS) for Optical MEMS,* Sensors and Actuators A **151**, 95 (2009).

[47] R. R. Besser, M. Ishahak, V. Mayo, D. Carbonero, and I. Claure, *Engineered Microenvironments for Maturation of Stem Cell Derived Cardiac Myocytes,* Theranostics **8** (2018), 10.7150/thno.19441.

[48] T. Matsuda, K. Takahashi, T. Nariai, T. Ito, T. Takatani, Y. Fujio, and J. Azuma, *N-cadherin-mediated cell adhesion determines the plasticity for cell alignment in response to mechanical stretch in cultured cardiomyocytes,* Biochemical and Biophysical Research Communications **326**, 228 (2005).

[49] S. Dhein, A. Schreiber, S. Steinbach, D. Apel, A. Salameh, F. Schlegel, M. Kostelka, P. M. Dohmen, and F. Wilhelm, *Mechanical control of cell biology . Effects of cyclic mechanical stretch on cardiomyocyte cellular organization,* Progress in Biophysics and Molecular Biology **115**, 93 (2014).

[50] I. Banerjee, K. Carrion, R. Serrano, J. Dyo, R. Sasik, S. Lund, E. Willems, S. Aceves, R. Meili, M. Mercola, J. Chen, A. Zambon, G. Hardiman, T. A. Doherty, S. Lange, C. Juan, and V. Nigam, *Cyclic stretch of embryonic cardiomyocytes increases proliferation , growth , and expression while repressing Tgf- β signaling,* Journal of Molecular and Cellular Cardiology **79**, 133 (2015).

[51] M. J. Madou, *Fundamentals of Microfabrication: The Science of Miniaturization, Second Edition* (CRC Press, 2002).

[52] S. C. (Ed.), *Microfluidics and Microfabrication* (Springer, 2009).

[53] A. van de Stolpe and J. den Toonder, *Workshop meeting report Organs-on-Chips: human disease models.* Lab on a chip **13**, 3449 (2013).

[54] T. Betancourt and L. Brannon-peppas, *Micro- and nanofabrication methods in nanotechnological medical and pharmaceutical devices,* International Journal of Nanomedicine , 483 (2006).

[55] J. H. Koschwanez, R. H. Carlson, and D. R. Meldrum, *Thin PDMS films using long spin times or tert-butyl alcohol as a solvent,* PLoS ONE **4** (2009).

[56] J. Garra, T. Long, J. Currie, T. Schneider, R. White, and M. Paranjape, *Dry etching of polydimethylsiloxane for microfluidic systems,* Journal of Vacuum Science & Technology A: Vacuum, Surfaces, and Films **20**, 975 (2002).

[57] S. R. Oh, *Thick single-layer positive photoresist mold and poly(dimethylsiloxane) (PDMS) dry etching for the fabrication of a glassPDMSglass microfluidic device,* Journal of Micromechanics and Microengineering **18**, 115025 (2008).

[58] W. Chen, R. H. W. Lam, and J. Fu, *Photolithographic surface micromachining of polydimethylsiloxane (PDMS),* (2012).

[59] B. Samel, M. K. Chowdhury, and G. Stemme, *The fabrication of microfluidic structures by means of full-wafer adhesive bonding using a poly(dimethylsiloxane) catalyst,* Journal of Micromechanics and Microengineering **17**, 1710 (2007).

[60] H. Wu, B. Huang, and R. N. Zare, *Construction of microfluidic chips using polydimethylsiloxane for adhesive bonding.* Lab on a chip **5**, 1393 (2005).

[61] R. Sivakumarasamy, K. Nishiguchi, a. Fujiwara, D. Vuillaume, and N. Clement, *A simple and inexpensive technique for PDMS/silicon chip alignment with sub-[small mu]m precision,* Analytical Methods **6**, 97 (2014).

[62] E. Colombo, F. Calcaterra, M. Cappelletti, D. Mavilio, and S. Della, *Comparison of Fibronectin and Collagen in Supporting the Isolation and Expansion of Endothelial Progenitor Cells from Human Adult Peripheral Blood,* PLOS One **8** (2013), 10.1371/journal.pone.0066734.

[63] Y. P. Petrov, L. V. Kukhareva, and T. A. Krylova, *The Effect of Type I Collagen and Fibronectin on the Morphology of Human Mesenchymal Stromal Cells in Culture,* Cell and Tissue Biology **7**, 545 (2013).

[64] V. V. Orlova, Y. Drabsch, C. Freund, S. Petrus-reurer, F. E. V. D. Hil, S. Muenthaisong, P. Dijke, and C. L. Mummery, *Functionality of Endothelial Cells and Pericytes From Human Pluripotent Stem Cells Demonstrated in Cultured Vascular Plexus and Zebrafish Xenografts,* Arterioscler Thromb Vasc Biol , 177 (2013).

[65] I. D. Huh D, Matthews B, Mammoto A, Montoya-Zavala M, Hsin H, *Reconstituting Organ-Level Lung,* Science **328**, 1662 (2010).

[66] A. S. Monzel, L. M. Smits, K. Hemmer, S. Hachi, E. L. Moreno, I. Boussaad, E. Berger, T. V. Wuellen, J. Jarazo, J. Walter, I. Bru, R. M. T. Fleming, S. Bolognin, and J. C. Schwamborn, *Derivation of Human Midbrain-Specific Organoids from Neuroepithelial Stem Cells,* Stem Cell Reports **8**, 1144 (2017).

[67] A. E. Freeman and R. M. Hoffman, *In vivo-like growth of human tumors in vitro,* Proc. Natl. Acad. Sci. **83**, 2694 (1986).

[68] W. Asghar, R. E. Assal, H. Shafiee, S. Pitteri, R. Paulmurugan, and U. Demirci, *Engineering cancer microenvironments for in vitro 3-D tumor models,* Biochemical Pharmacology **18**, 539 (2015).

[69] X. Xu, M. C. Farach-carson, and X. Jia, *Three-dimensional in vitro tumor models for cancer research and drug evaluation,* Biotechnology Advances **32**, 1256 (2014).

5

MICROSTRUCTURES FOR MECHANICAL SENSING

The contents of this chapter are based on the work published in:

1. W.F.Quirós-Solano, N.Gaio, C.Silvestri, G.Pandraud and P.M.Sarro. *Polymeric strain gauges as pressure sensors for microfabricated organ-on-chips.* The 19th International Conference on Solid-State Sensors, Actuators and Microsystems, 2017.
2. W.F.Quirós-Solano, N. Gaio, C. Silvestri, G. Pandraud, P.M. Sarro. *PEDOT:PSS: a Conductive and Flexible Polymer for Sensor Integration in Organ-on-Chip Platforms.* 30th Eurosensors Conference, EUROSENSORS, 2016.
3. W.F.Quirós-Solano, G. Pandraud, P.M. Sarro. *Wafer-level fabrication of strain gauges on PDMS membranes for low-pressure sensing.* IEEE Sensors, 2015.

5.1. INTRODUCTION

Organs-on-Chips (OOC) aim to become the alternative tool for *in vitro* screening. Researchers are still facing biological and technological challenges that impede this cutting-edge technology to be adopted as a routine tool in drug development. The limited scalability of current fabrication processes and the lack of self-integrated monitoring are among the technical limitations hindering its adoption [1].

So far, the majority of devices have relied entirely on manual fabrication and bulk characterization techniques (e.g staining, microscope cell imaging). This limits both the degree of biological mimicry achievable and high content data to be acquired from the cell microenvironment and biological processes. Phenomena can be either not preset due to the lack of proper mimicry (stimulation cues) or simply are not detected by conventional (e.g optical,sampling, staining) characterization. For instance, a more complete view of cell behaviour in heart on chips can be obtained if mechanical stress, bioelectrical activities, pH level, potassium and oxygen concentration could be quantitatively measured and controlled*in situ* in a spatio-temporal manner. Recently, several heart-on-chips including microstructures for mechanical stimulation have demonstrated their advantage for structural organization and maturation of the cells [2–5]. Most heart-on-chips are based on mechanically flexible materials that enable continuous mechanical stimulation of the different cell cultures [6–10]. To do so, PDMS (Polydimethylsiloxane) is tipically used as structural substrate facilitating dynamic stretching, exploiting its intrinsic advantages of biocompatibility, optical transparency and mechanical flexibility [11–13].

Recently, a monolithically microfabricated PDMS-based microelectrode array has been demonstrated [14, 15]. This so-called *Cytostretch*, has been previously used as a Heart-on-Chip with integrated microelectrodes enabling to access data related to the action potential generated by iPSC-derived cardyiomyocites with also the possibility to precisely stimulate electrically the cell culture. Chapter 4 demonstrated the possibility of further developing more specialized OOCs based on this type of microfabricated platforms. Nevertheless, the robustness of these type of platforms can be improved and its reliance on bulk optical microscopy and pneumatic transduction overcome. Other indirect means to quantify the actual mechanical strain on the membrane or cell mediums could be enabled by exploiting other transduction mechanisms generating signals in the electrical domain [16]. The potential of microfabrication techniques have thus not been fully exploited towards OOCs with self-integrated sensors.

This chapter investigates fabrication processes for the integration of microfabricated metallic and polymeric structures (strain gauges) to enable sensing of the mechanical strain on membrane-based OOCs platforms. The integration of strain gauges aim to enable electronic *in situ* monitoring of mechanical strain and reduce the need of external and complex pneumatic actuation for mechanical stretching.

5.2. STRAIN GAUGES ON PDMS MEMBRANES

Strain gauges are microstructures commonly used to quantify the strain of a holding substrate subjected to mechanical stress. By monitoring the change in the electrical resistance of these microstructures, the strain experienced by the substrate when stretched can be indirectly obtained. Integrating strain gauges in a microfabricated PDMS-based OOC platform enables the acquisition and quantification of the mechanical strain provided to a cell culture, thus allowing to gather more relevant information for biological studies.

The following sections provide the fundamentals considered for the design of the devices investigated and materials employed, their modelling and simulation, and the fabrication processes developed to integrate them in a microfabricated PDMS-based OOC platform.

5.2.1. TRANSDUCTION PRINCIPLE

The transduction principle of strain gauges exploits the known dependence of the electrical resistance on geometrical features. The electrical resistance of microstructures like the one shown in Fig.5.1, is expressed as

$$R = \rho \frac{L}{WT} \tag{5.1}$$

where ρ, L, T and W are the resistivity, length, width and thickness of the conductive microstructures, respectively. When current (I) flows through the conductive structure subjected to deformation, a change in the electrical resistance is induced (Δ R). The total resistance change due to changes in the geometry can be calculated by

$$\Delta R = \frac{\partial R}{\partial L}\Delta L + \frac{\partial R}{\partial W}\Delta W + \frac{\partial R}{\partial T}\Delta T \tag{5.2}$$

where ΔL, ΔW and ΔT are given by the total strain of the corresponding dimensions. Thus, the ΔR in terms of the strain can be expressed as

$$\Delta R = R\varepsilon_L - R\varepsilon_W - R\varepsilon_T = R(\varepsilon_L - \varepsilon_W - \varepsilon_T) \tag{5.3}$$

Equation 5.3 accounts for changes in the resistance due to the total longitudinal strain and the consequent change in cross-section are due to the material becoming wider and thinner [17]. Supposing the microstructures are mechanically attached to the substrate and the material has a linear isotropic behaviour, the total resistance change can be generally reduced to

$$\Delta R = R(\varepsilon_{long}(1+\nu) - \varepsilon_{tan}(1-\nu)) \tag{5.4}$$

Where, (ε_{long}) and (ε_{tan}) are the longitudinal and tangential strain with respect to the current direction. Thus, the expression is valid for both radial and tangential geometries. Equation 5.4 highlights thus the potential to translate mechanical strain into an electrical signal. This transduction mechanism contemplates only geometrical changes, variations on the resistivity of the material and thermal effects are not included.

5.2.2. MECHANICS OF MEMBRANES

This section briefly describes the fundamental of mechanics for thin membranes considered to implement the strain gauges on PDMS membranes.

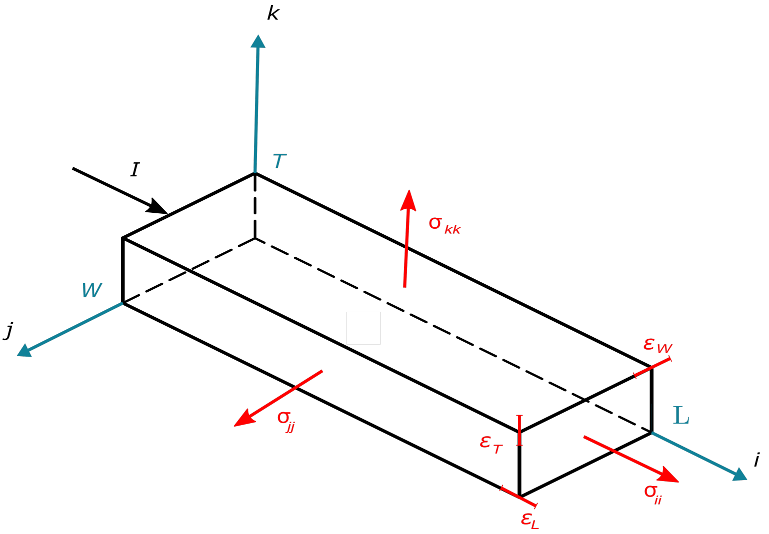

Figure 5.1: A 3D sketch of a resistor (R) with dimensions under a mechanical stress (σ_{ij}) and corresponding strain ($\varepsilon_L,\varepsilon_W,\varepsilon_T$). The corresponding dimensions that define the geometry are the length (L), width (W) and height (T).

The deformation of a material (ϵ) subjected to mechanical forces is directly proportional to the stress applied (σ). Such proportionality quantified by the stiffness tensor (c) as:

$$\varepsilon \mathbf{c} = \sigma \tag{5.5}$$

In this equation it is implicit that a material of certain characteristics and geometry deforms in all directions. The tensor c includes the adequate proportions including the material properties, namely the Young Modulous (E) and Poissons ratio (ν). Considering the case of an isotropic material in a linear elastic regime, Eq.5.5 can be expressed in index notation as:

$$\varepsilon_{ij} = \frac{1}{E}\left[(1+\nu)\sigma_{ij} - \nu\sigma_{kk}\delta_{ij}\right] \tag{5.6}$$

Which is refereed as Hookes law. The indexes *i,j,k* correspond to the components of an orthonormal coordinate system (Fig. 5.1). Equation 5.6 shows how deformations in an specific direction (e.g ε_{ii}) are not exclusively consequence of parallel forces (σ_{ii}), but that also forces present in perpendicular directions (σ_{jj},σ_{kk}) contribute to the total deformation of the material [17].

Particularly, the mechanics of membranes under load can be then understood by solving Eq. 5.6 for a specific geometry under certain boundary conditions. This can be done either through analytical methods or Finite Elements Method (FEM) to fully understand the displacement at the center of the membrane d) and strain distribution ($\varepsilon_r,\varepsilon_t$) as function of a pressure difference (ΔP) applied to the membrane. These type of problem has been extensively studied for circular and square thick and thin membranes, giving reliable analytical expressions [18–20]. For a circular membrane, the equation relating displacement and pressure drop as function geometry and material properties is given by

$$\Delta P = \frac{4td}{r^2}\left(\frac{4}{3}\frac{t^2}{r^2}\frac{E}{1-\nu^2} + \sigma_0 + \frac{64}{105}\frac{d^2}{r^2}\frac{E}{1-\nu^2}\right) \tag{5.7}$$

Where t,r and σ_0 are the thickness and radius of the membrane, and any residual stress, respectively.

Moreover, assuming a semicircular profile in the deformation of the membrane, continuously distributed along the radius, the radial strain can be calculated based on the displacement as introduced in previous chapter in Eq. 4.15, as

$$\varepsilon_r = \frac{r_{final} - 2r}{2r} = \frac{(r)^2 + d^2}{2rd} arcsin\left(\frac{2rd}{(r)^2 + d^2}\right) - 1 \tag{5.8}$$

Considering that radial and tangential strain at the center of the membrane are equivalent and that the membrane is fixed at its circumference, the corresponding tangential strain as a function of the position along the radius $\varepsilon_t(\varrho)$ can be approximated through a parabolic function given by

$$\varepsilon_t(\varrho) = \varepsilon_r\left(1 - \frac{\varrho^2}{r^2}\right) \tag{5.9}$$

where ϱ and r are the distance from the center of the membrane and the membrane radius, respectively. Equations 5.8 and 5.9 allow to estimate the expected strain and its distribution along a thin membrane for different applied pressures. This makes possible to establish the initial design criteria and define the optimal location and dimensions of the strain gauges.

5.3. DESIGN AND MATERIALS

The devices investigated consist of either metal or polymeric strain gauges integrated on a PDMS membrane suspended from a silicon holding frame, a platform based on the *Cytostretch* [14, 15]. The membrane acts as a stretchable substrate for cell culturing with the strain gauges allowing a continuous electrical monitoring of the strain on the substrate surface when mechanically stretched. Pneumatic actuation enables the stretching of the membrane by applying a pressure load on its bottom surface. In Figure 5.2, the architecture of the devices is shown.

The shape, thickness and diameter of the membrane is determined based on Eq. 5.8, aiming at providing specific radial strains (0-10%) for pneumatic actuation pressures up to 2 kPa, while reducing the risks to compromise the mechanical stability of the devices during fabrication. The circular shape was prefered to exploit the symmetry of the strain distribution along the membrane [17]. The final design comprises a flexible circular 9 μm-thick (t) PDMS membrane of 3 mm in diameter (D).

The position and dimensions of the strain gauges were defined based on the expected distribution of strain on circular membranes, and electrical criteria. Based on Eq. 5.9, the strain gauges were located close to the edge of the membrane, where the

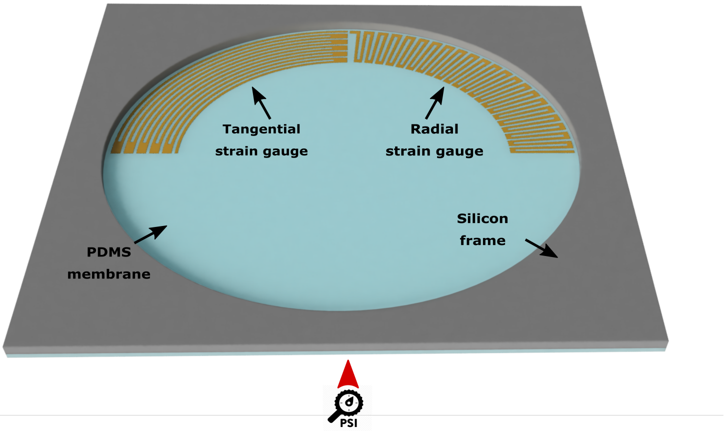

Figure 5.2: Architecture of the device investigated for stress sensing in a microfabricated PDMS-based OOC platform: Tangential and radial microstructures (strain gauges) on PDMS membranes suspended from a holding silicon frame. The membrane is pneumatically actuated to provide the stretching of a cell culture on its surface.

gradient of the tangential strain along the radial direction is high. Serpentine-like geometries of length (L_r, L_t) were then defined to maximize the microstructures parallel to the expected main strain directions (radial and tangential). Likewise, the width ($W = 20$ μm) was then defined to exploit the expected mechanical behaviour and to have final electrical resistances in the range of $k\Omega$, matching with standard resistors necessary for further signal conditioning. The thickness was defined to comply with the above mentioned electrical criteria and reduced as much as possible to minimize the effect of the strain gauges on the membrane deformation.

Two materials were investigated, namely a metal (Titanium) and a conductive polymer, poly(3,4-ethylenedioxythiophene)(PEDOT:PSS). Titanium was selected given its well known mechanical behavior, biocompatibility, gauge factor (GF$\simeq 0.8$) and the possibility to pattern it with conventional lithography and dry etching techniques[21–25]. PEDOT is a polymer derived from ethylene dioxythiophene monomer. The electrical conductivity is caused by the delocalized π-electrons within its chemical structure and the presence of sulfonated polystyrene (PSS). It was investigated due to its known electronic conduction, biocompatibility, high transparency (≥ 90 %) and particularly for its reported mechanical flexibility ($E \simeq 1.2$ GPa)[26–28], making it suitable for either sensing or stimulating microstructures[29]. Moroever, several studies suggest that this polymer can provice a gauge factor in the $0.48 - 17.8$[30–32].

5.4. MODELLING AND SIMULATION

An initial evaluation trough numerical simulations was done to study the expected mechanical performance of the envisioned microstructures. The microstructures and the PDMS membrane shown in Figure 5.2 were modelled and the corresponding solution to the set of equations given above (Eqs. 5.5 and 5.6) obtained using the FEM-based software Comsol Multiphysics®. The mechanical modelling implemented was defined so that the corresponding set of equations can be computationally solved and the boundary conditions match the experimental conditions intended for the electromechanical characterization. As demonstrated in other works, numerical simulation provide better insight on the mechanical behaviour of membranes with strain gauges, specially on thin membranes, as the effect of the microstructures on the final deformation of the membrane is better comtemplated [17].

The modelling of the membrane with strain gauges was done based on both linear and non-linear equations of solid mechanics. The non-linearity of the model is included to better approximate real behaviour by considering non-elastic properties of the polymeric membrane [33]. Hence in the model, the material properties were introduced through a stress-strain curve to include such non-linearity based on data reported in literature (Fig. 5.3c), as already shown in Chapter 4, Section 4.4.2 [33, 34]. The strain gauges were modelled assuming a linear isotropic and elastic material. Values reported in literature were used for the Youngs Modulus (90 GPa, 2 GPa) and Poisson ratio (0.31,0.35) of Titanium (Ti) and poly(3,4-ethylenedioxythiophene) polystyrene sulfonate (PEDOT:PSS), respectively [26–28, 35].

The boundary conditions established for the model were determined based on the envisioned use of the device for mechanical stretching of cell cultures, as illustrated in Figure 5.3a. A boundary condition of zero displacement on the substrate surface surrounding a circular membrane was considered, as this is the region where the membrane is clamped to the silicon substrate. A boundary force equivalent to the pneumatic pressure applied at the bottom surface of the membrane was considered (Fig. 5.3b). Subsequently, the geometry was meshed with (14 thousand elements) a high quality (≈ 0.83) meshing (Fig. 5.3b and d).

The computation was carried out to determine the displacement field of each of the elements of the geometry representing the device. In Figure 5.4a and b, the strain field of a membrane with radial and tangential strain gauges actuated with 2 kPa, is shown. In Figure 5.4c and d, curves illustrating the expected displacement at the center of the membrane and the average strain are reported.

5.5. FABRICATION PROCESS

To fabricate the strain gauges on PDMS membranes, wafer-level fabrication processes were developed based on conventional photolithography and on MEMS techniques. As the nature of the two materials investigated is significantly different, namely a metal (Ti) and conductive polymer (PEDOT:PSS), two independent processes were developed to integrate the strain gauges.

5.5.1. METAL STRAIN GAUGES

The fabrication process of the metal strain gauges is schematically depicted in Figure 5.5. The process starts with the deposition of a 1 μm PECVD SiO_2 on the front side of a 100 mm in diameter, 525 μm-thick silicon wafer (Fig. 5.5a). The oxide layer acts as an etch-stop for the Deep Reactive Ion Etching (DRIE) of the silicon substrate used to form

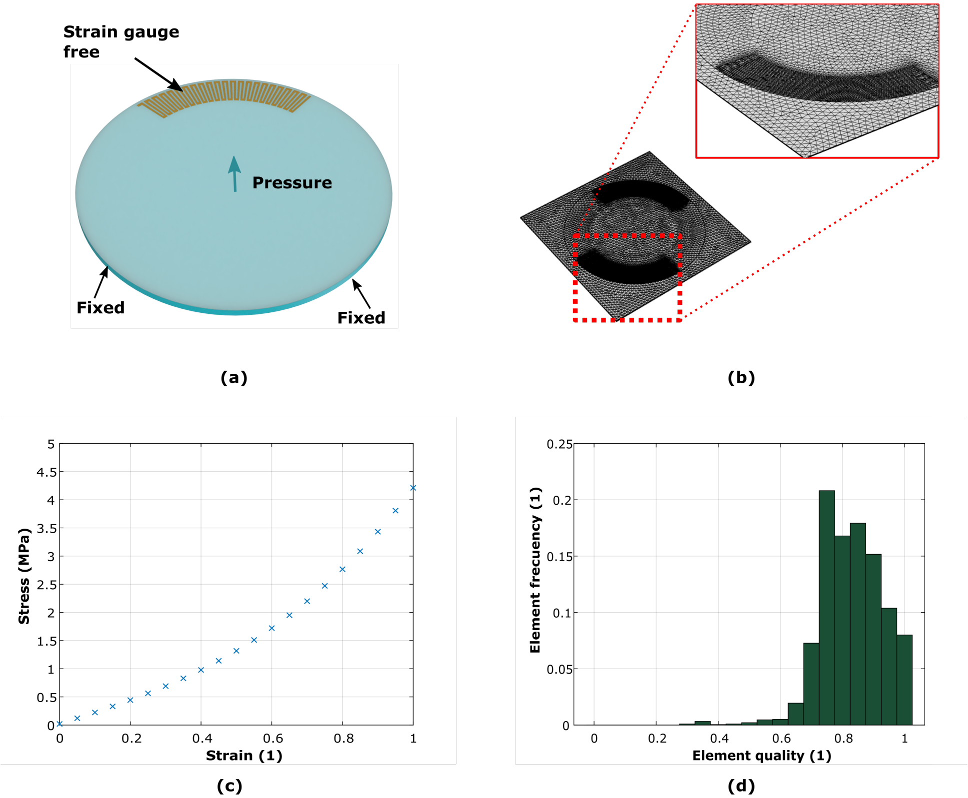

(a) **(b)**

(c) **(d)**

Figure 5.3: **(a)** Boundary conditions for the mechanical modelling of the strain gauges on 12 μm thick PDMS-membranes. The edges of the membranes are fixed through a zero velocity boundary conditions to reproduced the clamping to the holding silicon frame. The pneumatic stretching is provided to the model trough a boundary force conditions corresponding to a range of pressures for mechanical stretching. **(b)** Geometry of the devices meshed with Comsol Multiphysics®. **(c)** Stress-strain curved used to include the non-linear effects of the PDMS. **(d)** The corresponding Histogram on the quality of meshing of the geometry for solving the displacement and strain fields.

the membrane. On the backside of the wafer a 6 μm PECVD SiO_2 hard-mask layer is deposited and patterned to define the circular shape membranes (Fig. 5.5b).

A 300 nm photosensitive polyimide (PI) layer is deposited and patterned. This layer is included to provide electrical isolation as well as protection of the metal lines during the subsequent steps of the process (Fig. 5.5c). Next, a 600 nm-thick Aluminum (Al) and 100 nm-thick titanium layer is sputtered on the PI at room temperature. The resistivity of the sputtered materials is 20 $\mu\Omega$-cm and 106 $\mu\Omega$-cm, respectively. The Al layer is patterned and selectively etched by using wet etching (Fig. 5.5d). After defining the contacts, the Ti layer is patterned by dry etching (ICP Plasma etcher, Trikon Omega 201) with a 2 μm-thick positive resist as masking layer (Fig. 5.5e). Then, a layer of PDMS (Dow Corning, Sylgard 184) is spin coated on the front side. The elastomer and curing agent are mixed in a 10:1 ratio and degassed in a centrifugal vacuum mixing and degassing tool. The

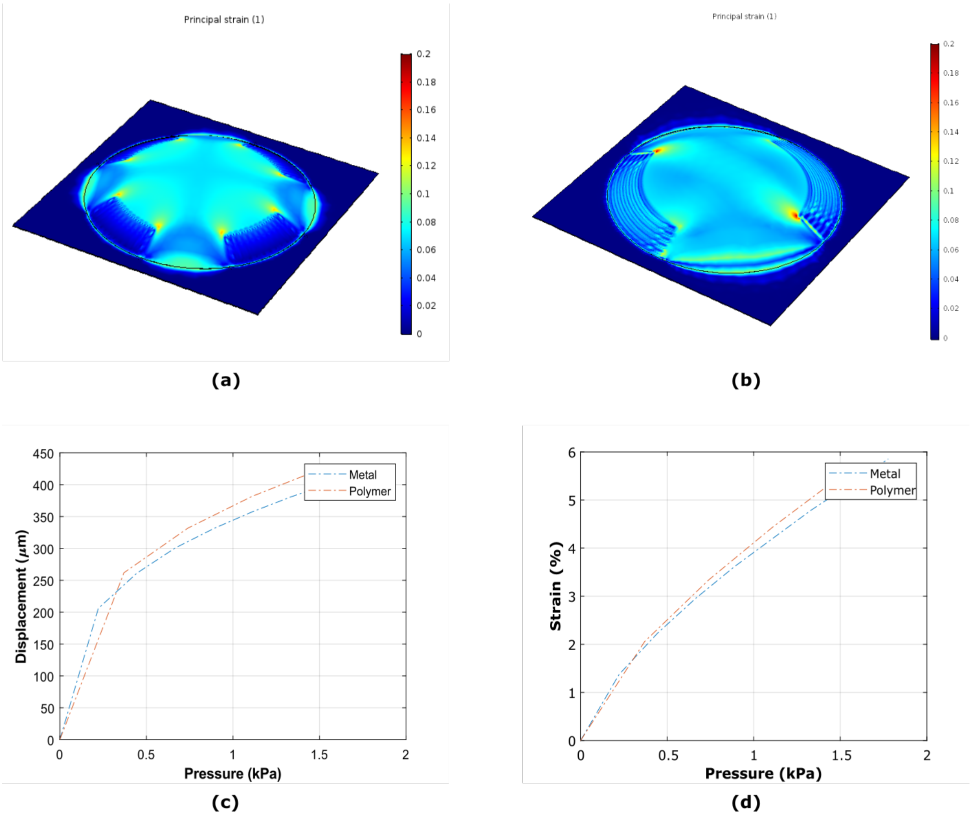

Figure 5.4: Strain field of the membranes with radial **(a)** and **(b)**tangential strain gauges for a boundary force corresponding to 2 kPa. (c) Curve of the displacement at the center of a membrane with metal and polymer strain gauges for pressures up to 2 kPa. (d) Corresponding average strain of the membrane.

polymer is spun in three steps: a first step to spread the material over the silicon wafer at 10 rpm for 10 s; a second step for uniform spreading at 300 rpm for 20 s and a final step at 6000 rpm for 30 s to get the desired 9 μm thickness. The polymer curing is done for 30 minutes at 90 °C in a convection oven (Fig. 5.5f). Subsequently, a 100 nm-thick Al layer is sputtered on the PDMS at room temperature. This temperature is set to avoid cracking of the PDMS layer during sputtering due to the high coefficient of thermal expansion of the PDMS (310 μm/m °C). The metal is patterned by dry etching (ICP Plasma etcher, Trikon Omega 201) to open the areas corresponding to the electrical contacts of the metallic microstructures (Fig. 5.5g). The etching process used was optimized to avoid any issue caused by thermo-mechanical stress. No cracking of the layers is in fact observed when exposing the materials to the thermal gradients during resist deposition and developing steps. Finally, the silicon substrate is etched from the backside by DRIE using a Bosh-based process (Fig. 5.5h). The oxide stop layer is removed by a combination of wet and dry etching (Fig. 5.5i). The Al layer is selectively etched in a solution of acetic, phosphoric and hydrofluoric acid (Fig. 5.5j). More details are found in Appendix B.2.

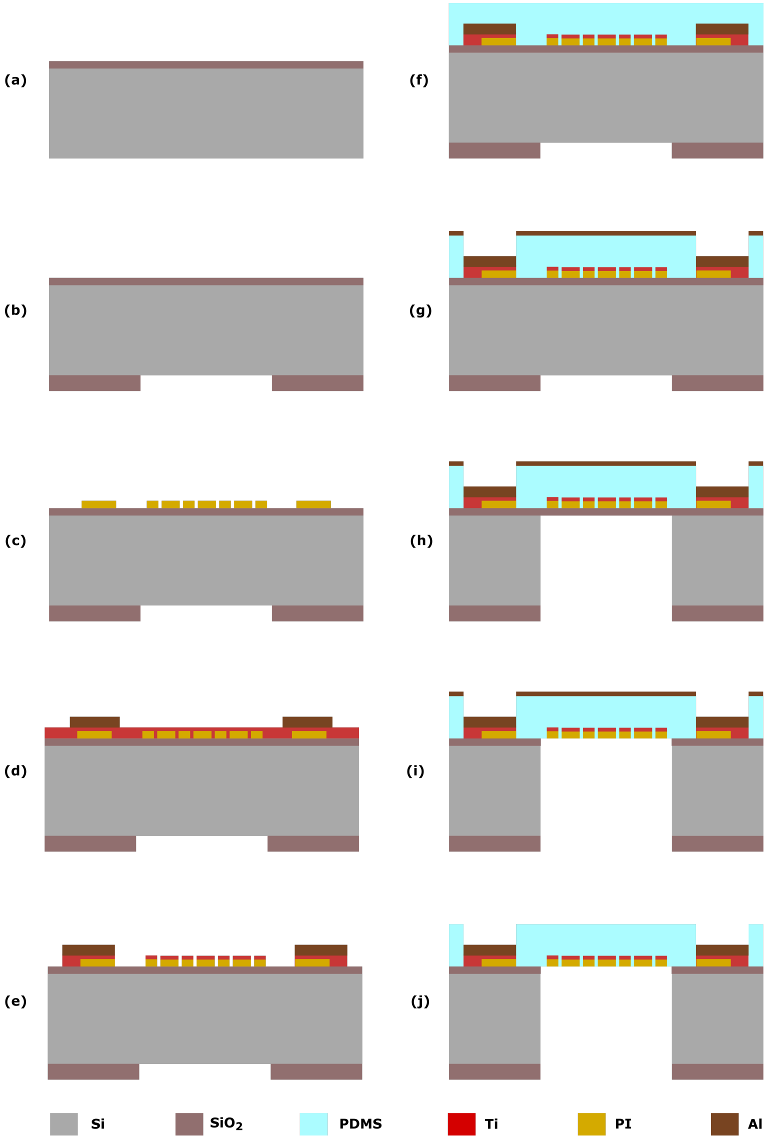

Figure 5.5: Main steps of the fabrication process for the integration of Ti strain gauges on PDMS membranes. **(a)** Deposition of oxide on the wafer front side. **(b)** Deposition and patterning of the oxide on the wafer back side to define the circular membrane. **(c)** Deposition and patterning of PI layer for electrical and mechanical isolation. **(d)** Deposition of Ti and patterning of electrical contacts (Al). **(e)** Patterning of the metal layer corresponding to the strain gauges (Ti). **(f)** Deposition of PDMS layer. **(g)** Deposition and patterning of the (Al) masking layer and etching of the PDMS layer to open the electrical contacts. **(h)** Etching of the silicon substrate using a DRIE process. **(i)** Removal of the landing oxide layer. **(j)** Removal of the masking layer (Al) by wet and dry etching.

In Figure 5.6 a full wafer containing several membranes with strain gauges is shown, demonstrating the wafer-scale capability of the developed process. A close-up of the released membranes (red dash line) and the titanium strain gauges can be also observed. In the background several fibers are noticed corresponding to the supporting substrate (napkins are used during microscope inspection), hence showing the transparency of the PDMS in the visible spectrum.

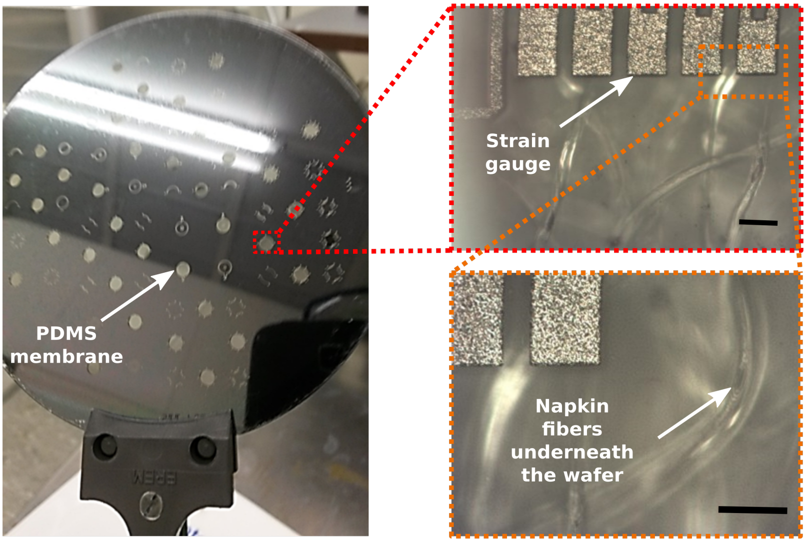

(a) (b)

Figure 5.6: **(a)** A completed wafer containing 36 membranes with strain gauges. **(b)** Optical image from the backside cavity showing a close-up of the Ti gauges on the released membranes. Scale bar: 60 μm.

5.5.2. POLYMERIC STRAIN GAUGES

Given the higher gauge factor suggested in literature, its electronic and ionic conduction, and the appropriate mechanical properties, the conductive polymer PEDOT:PSS is an interesting material to enable fully-polymeric strain gauges and other stimulating microstructures for OOC platforms. PEDOT is a polymer derived from ethylene dioxythiophene monomer. The electrical conductivity is caused by the delocalized π-electrons within its chemical structure and the presence of sulfonated polystyrene (PSS). The polymer offers advantages due to its electronic and ionic conduction, biocompatibility, as well as for its mechanical (E≈1.2 GPa) and optical properties (T >90 %), making it suitable for either sensing or stimulating microstructures [29].

PEDOT:PSS MICROSTRUCTURES

Microstructures were successfully realized by patterning the polymer on a silicon (Si) substrate, following a wafer-level fabrication approach. In Figure 5.7 the main steps of the patterning process are depicted.

Firstly, a 1 μ-thick plasma enhanced chemical vapor deposition (PECVD) silicon oxide (SiO_2) is deposited on a 100 mm-Si wafer. Then a layer of 100 nm of Silver (Ag) is deposited by evaporation and subsequently patterned by lift-off to create electrical contacts (Fig. 5.7a). An aluminium layer is then deposited and patterned to be used as protective layer during the subsequent etching of the polymer (Fig. 5.7b). The PEDOT:PSS layer is deposited by spin coating and cured in an oven at 150 °C for 40 minutes (Fig. 5.7c). The achieved layer thicknesses versus the spinning conditions are depicted in Figure 5.8. The electrical resistivity of a 300 nm thick PEDOT:PSS layer is 41 $\mu\Omega$m. On top of the PEDOT:PSS another Aluminum (Al) layer is sputtered and patterned (Fig. 5.7d). The Al layer is used as hard mask during the reactive-ion etching (RIE: O_2, 20 mTorr, 50 W) of the PEDOT:PSS (Fig. 5.7e). The PEDOT-based microstructures are now defined and metal contacts are exposed. As last step, the Al hard mask and protection layer of the contacts is removed by wet etching using a solution of acetic acid, nitric acid and hydrofluoric acid (PES) (Fig. 5.7f).

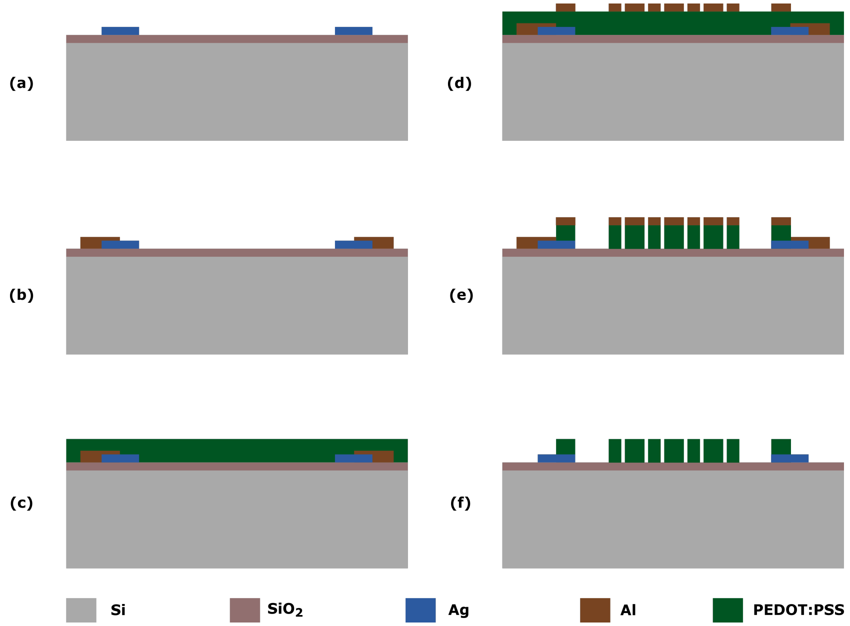

Figure 5.7: Main steps of the patterning process of the PEDOT:PSS microstructures. **(a)** Deposition of oxide and silver (Ag) on front and patterning of Ag layer to define the electrical contacts. **(b)** Deposition and patterning of Al layer to open the electrical contacts to the conductive polymer and cover the remaining Ag layer for the subsequent etching steps. **(c)** Deposition and curing of the PEDOT:PSS layer. **(d)** Deposition and patterning of the Al masking layer. **(e)** Dry etching of the PEDOT:PSS. **(f)** Removal of Al masking and protective layer from the patterned microstructures and metal contacts.

Customized features are obtained by lithographically defining the hard-mask patterning. The resulting PEDOT:PSS microstructures, that can be used as microelectrodes or strain gauges are shown in Figure 5.9a,c and Figure 5.9(b,d), respectively. In particular, figure 5.9c shows a close up of the microelectrodes for cell stimulation, with lateral dimensions down to 2 μm.

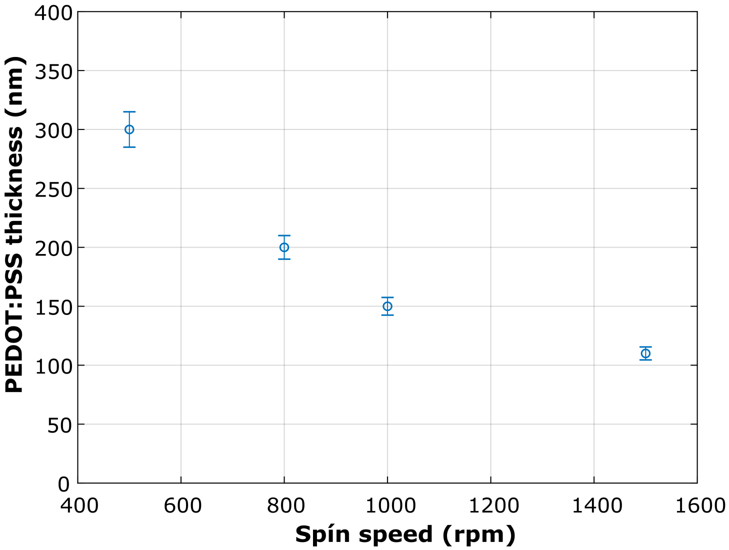

Figure 5.8: Thickness versus spin speed of the deposited and cured PEDOT:PSS layers.

In the process reported, special attention was paid to the optimization of the electrical contact between the polymer and the metal pads. Specifically, as first contact layer a low reactive metal was needed due to the high acidity of the sulfonate functional group (PSS), which easily oxidizes most metals used in IC fabrication processes, unavoidably increasing the contact resistance [36].

INTEGRATION OF POLYMERIC STRAIN GAUGES

The designed microstructures were successfully integrated in the PDMS membranes. Although PEDOT:PSS has already been applied in related devices for neuron cell study, either rigid materials were used as the supporting substrate or the complexity of fabrication methods lack of compatibility with high scale manufacturing schemes [29].

The microstructures were here integrated in the 9 μ-thick PDMS membranes, while maintaining a wafer-level fabrication approach. In Figure 5.10 the main steps of the fabrication process are shown.

Once the conductive polymer is patterned as described in previous section (Fig. 5.7a-f), a PDMS layer is deposited by two-step spin coating process (Fig. 5.10g). To open the contact pads, the PDMS is etched by RIE (SF_6/CF_4), using an Al hard mask (Fig. 5.10h). The last step corresponds to the membranes release by deep reactive-ion etching (DRIE) using a 6 μm-thick PECVD as masking layer on the wafer backside (Fig. 5.10i). The landing layer made of 1 μm PECVD SiO_2 and the Al layer are removed by wet etching (Fig. 5.10i). More details can be found in Appendix B.3.

Several membranes with strain gauges were realized on a single wafer. In Fig. 5.11 optical images show a close-up of the polymeric strain gauges released and integrated on the membranes. Both radial (Fig. 5.11a) and tangential (Fig. 5.11b) geometries were

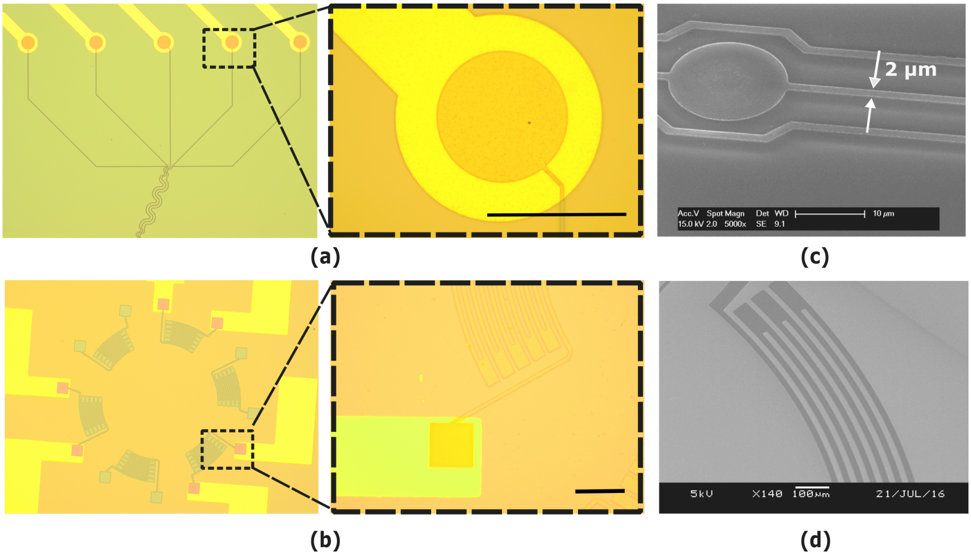

(a) (c)

(b) (d)

Figure 5.9: Optical and SEM images of successfully patterned PEDOT:PSS microstructures: **a)** and **c)** Microelectrodes; **b)** and **d)** A serpentine-like geometry proposed as a strain gauge to sense the stress on a cell culture medium. Scale bar: 100 μm.

realized, so to investigate the electromechanical response of the polymeric strain gauges.

The as deposited sheet resistivity of the PEDOT:PSS was 400 $\Omega/\square$ and is not significantly affected during the further processing steps necessary to realize the full device. Depending on the geometry, the absolute resistance value of the devices ranges from 30 to 900 kΩ. Since PEDOT:PPS is highly hygroscopic, the process has been optimized to avoid long time exposures of the conductive polymer layer to water [36].

5.6. CHARACTERIZATION SET-UP

The characterization set-up used to measure the resistance change of the strain gauges subjected to mechanical stress is shown in Figure 5.12. It consists of three main modules: a 3D-printed holder to interface the silicon chip with a pressure controller, a probe station and external circuitry for data acquisition and signal conditioning.

5.6.1. MECHANICAL COUPLING

To couple both the electrical functionality and pneumatic actuation of the devices, a custom-made holder was specifically designed and fabricated by 3D printing.

The holder allows to stretch the membrane through the silicon cavity by connecting the chip to a commercial pneumatic pumping system. A commercial Dual AF1 microfluidic pressure and a vacuum pump (Elveflow®) were used to control the pressure. This system makes possible to accurately control the pressure from 0 up to 30 mbar. Moreover, the holder enables electrical connection from the chip to external circuitry as they were both designed such that the Al contact pads on the silicon substrate are easily ac-

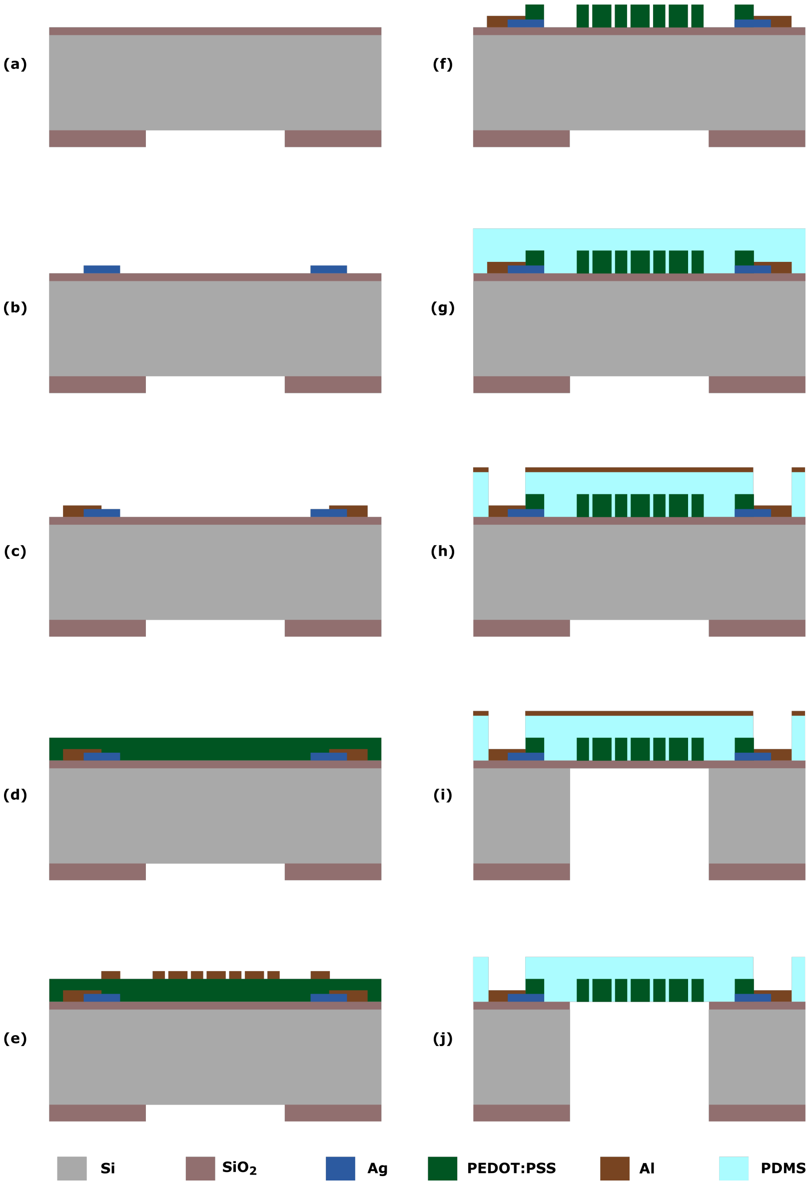

Figure 5.10: The main steps of the process flow developed for the wafer-scale fabrication of polymeric strain gauges. **(a)** Deposition of oxide on front and back and patterning to define the membranes area. **(b-f)** Deposition and patterning of PEDOT:PSS. **(g)** Deposition of the PDMS layer. **(h)** Deposition and patterning of the metallic (Al) masking layer and the PDMS layer to open the electrical contacts. **(i)** Etching of the silicon substrate using a Bosh-based DRIE process. **(j)** Removal of the landing oxide layer and the masking layer (Al) by wet and dry etching.

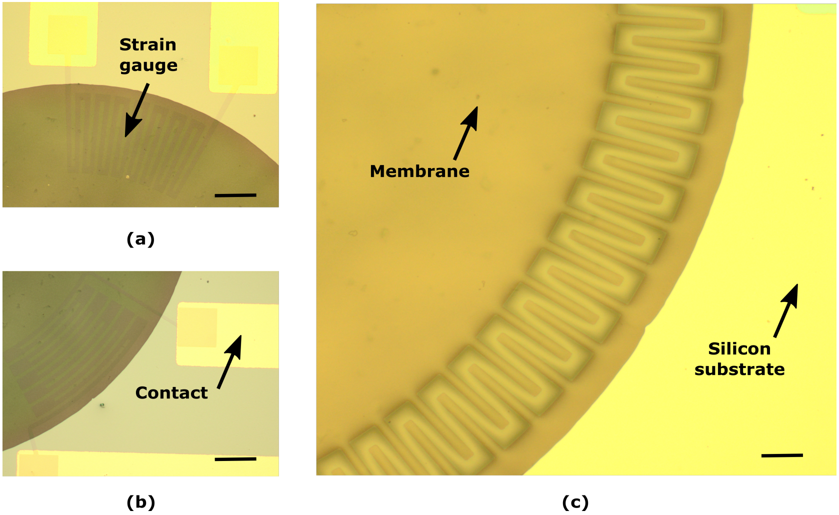

Figure 5.11: Optical images of **(a)** radial and **(b)** tangential polymeric strain gauges embedded in 10 μm-thick PDMS. **(c)** A zoom-in perspective illustrating the polymeric strain gauges integrated in the PDMS membranes. Scale bar: 100 μm.

cessed from the top (Fig. 5.13a). An actual image showing the holder coupled to the pumping system, is depicted in Figure 5.13b.

5.6.2. SIGNAL ACQUISITION AND CONDITIONING

The external circuitry to measure the electrical resistance change is connected to the metallic and polymeric strain gauges contacts through a standard probe station. The complete circuit for signal conditioning and acquisition is shown in Figure 5.14

A Wheatstone bridge is implemented as a first stage for signal conditioning. For this circuit topology, an expression for the resistance of the strain gauges (R_{SG}) as function of the voltage differences (V, V_{CC}) and the other resistors can be obtained applying Kirchhoffs voltage law

$$V_{R2} - V - V_{SG} = 0 \tag{5.10}$$

where

$$V_{R2} = \frac{V_{CC}R_2}{R_1 + R_2} \tag{5.11}$$

$$V_{R2} = \frac{V_{CC}R_{SG}}{R_{SG} + R_3} \tag{5.12}$$

Thus, the resistance can be obtained as

$$R_{SG} = \frac{V_{CC}R_2 - V(R_1 + R_2)}{V_{CC}R_1 + V(R_1 + R_2)}R_3 \tag{5.13}$$

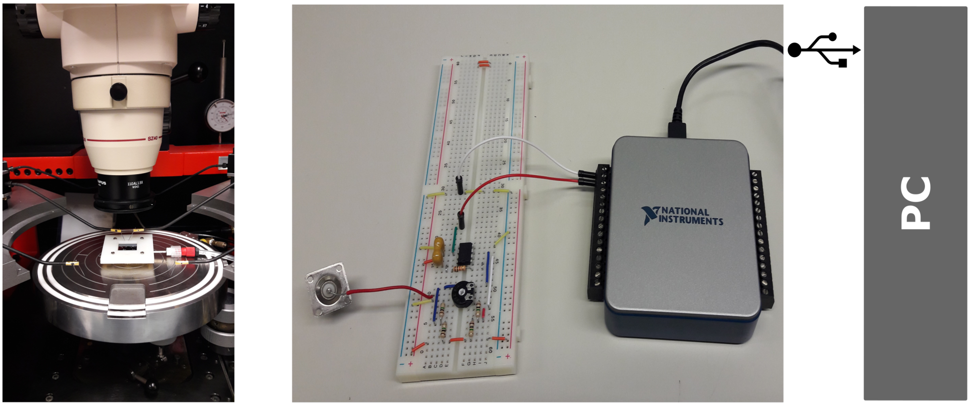

(a) (b)

Figure 5.12: Measurement set-up developed to characterize the microfabricated strain gauges. **(a)** The electrical signal from the strain gauges is acquired by probing them with a standard probe station. The pneumatic actuation is provided simultaneously through a special coupling holder connected to a pressure source. **(b)** The electrical signal is conditioned and transmitted to a PC for further calculations and data processing.

Table 5.1: Experimental values of the electrical components used in the circuitry for the radial and tangential strain gauges investigated.

	Metal strain gauges				**Polymeric strain gauges**			
	R1(kΩ)	*R2(kΩ)*	*R3(kΩ)*	*Rsg(kΩ)*	*R1(kΩ)*	*R2(kΩ)*	*R3(kΩ)*	*Rsg(kΩ)*
Radial geometry	3.9	3.8	3.9	3.8	60	59.9	60	59.9
Tangential geometry	9.2	9.8	9.2	9.8	310	315	310	315

The signal (V) is amplified by an operational amplifier (AMP04F, Analog Devices) with high gain ($G = 100$) and input impedance ($\approx M\Omega$). The output signal of the amplifier is acquired through an Analog-to-Digital converter (USB-6001, National Instruments), enabling the direct acquisition of the data in a personal computer and the corresponding calculation of the resistance change. The signal is further processed and filtered using a digital low pass filter with cut-off frequency fixed at 10Hz. The cut-off frequency is set as low as possible to reduce the high frequency noise and keep the measurement bandwidth within the range of typical biological processes e.g heartbeat: 1-4 Hz. The values of the resistors used are summarized in Table 5.1 for the strain gauges investigated.

5.7. ELECTROMECHANICAL CHARACTERIZATION

The characterization of the devices was carried out by continuously monitoring the electrical resistance for different stationary pressures. This was done for two geometries, radial and tangential for strain gauges located close to the edge of the PDMS membranes. The response of the devices was investigated for both Ti and PEDOT:PSS strain gauges.

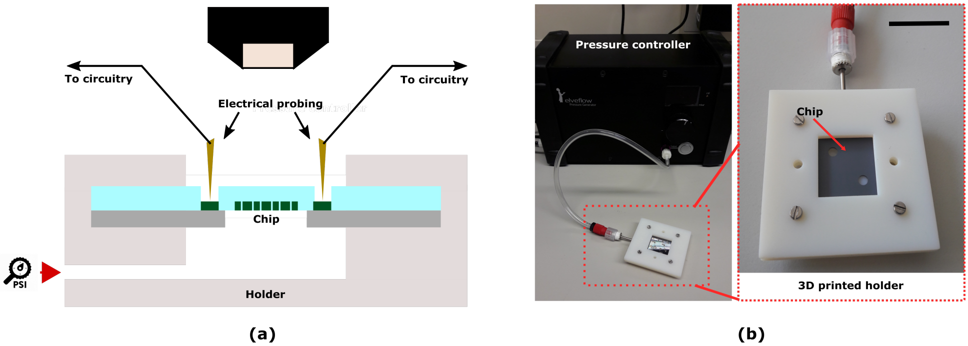

Figure 5.13: **(a)** Schematic of the holder designed to enable the coupling of the devices with both electrical circuitry and the commercial pneumatic pumping system. **(b)** A photograph of the custom-made holder coupled to the pumping system employed for the electromechanical characterization. Scale bar: 20 mm.

5.7.1. ELECTRICAL RESISTANCE

Stationary measurements of the resistance change for tangential and radial strain gauges are shown in Figure 5.15. The pressure was increased from 0 to 3kPa in steps of approximately 350 Pa, a value slightly higher than the minimum stable change in pressure achieved with the commercial pumping system employed.

An incremental variation of the resistance was observed. For titanium strain gauges, a relative resistance change up to ≈0.008 % over the tested pressure range was measured for both radial an tangential radial geometries (Fig. 5.15a).

For PEDOT:PSS straing gauges, a relative resistance change up to ≈1.4% was measured for the tangential geometries, a much higher value than the observed for its metal counterpart. In the case of the radial strain gauge, the resistance change was found to be ≈0.08% (Fig. 5.15a). The measurements were done under controlled humidity conditions with relative humidity ≈ 28%. Having a controlled humidity is important as it has been shown that both electrical and mechanical properties of PEDOT:PSS vary with humidity [26]. All results were thus obtained under the same environment conditions. For both geometries and materials, measurements at higher pressure were not possible as the pumping system reached the maximum flow capacity at 3 kPa.

5.7.2. MEMBRANE DISPLACEMENT AND STRAIN

The displacement at the center of the membrane with polymeric and metal strain gauges was measured for the same pressure ranges using the method described in previous chapter, section 4.6.3. In Figure 5.16a, the displacement for different pressures is shown.

Correspondingly, the strain on the membrane was indirectly obtained assuming a semicircular profile and a continuous distribution along the radius, the radial strain can be calculated based on the displacement by

$$\varepsilon_r = \frac{r_{final} - 2r}{2r} = \frac{(r)^2 + d^2}{2rd} arcsin\left(\frac{2rd}{(r)^2 + d^2}\right) - 1 \tag{5.14}$$

In Figure 5.16b, the calculated radial strain for the same pressures range used to investigate the resistance change, is shown.

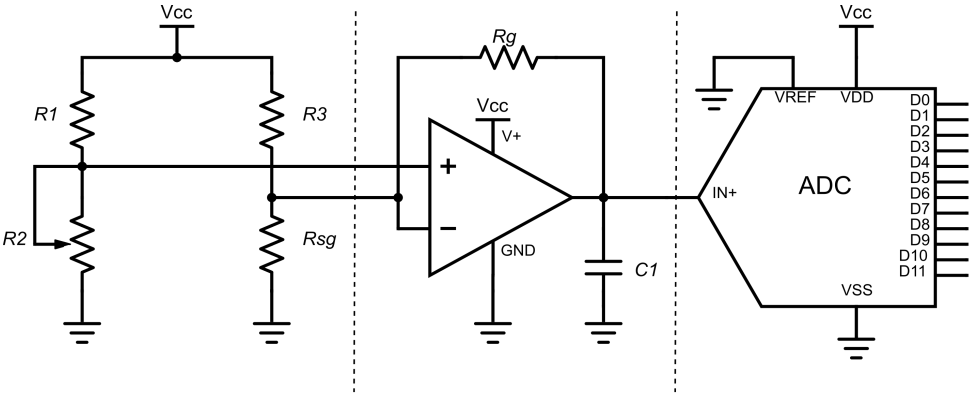

(a) **(b)** **(c)**

Figure 5.14: Circuit for converting the resistance changes into a differential voltage. $V_{CC} = 5V, Rg = 1k\Omega, C1 = 100nF$. **(a)** A half Wheatstone bridge with potentiometer for calibration of output signal with $R_1 = R_3$ with fixed values depending on the strain gauge (R_{sg}) investigated and R_2 varying to fix the offset voltage. **(b)** An amplification and filtering stage for conditioning the signal. **(c)** Serial communication stage to transfer the data of the voltage change for calculating the corresponding resistance change.

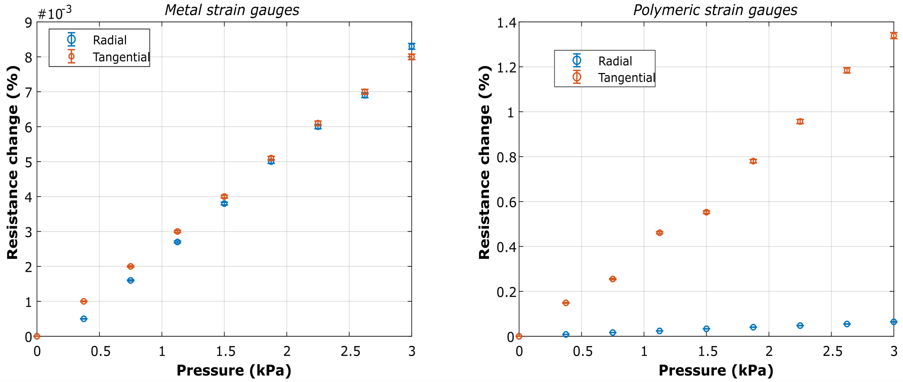

(a) **(b)**

Figure 5.15: Stationary measurements of resistance change for radial and tangential strain gauges made of **(a)** titanium (Ti) and **(b)** PEDOT:PSS.

5.7.3. CALIBRATION

The results from the electrical and mechanical measurements from Figures 5.15a-b were gathered to establish a calibration curve for the strain gauges investigated, namely the resistance change of the devices as function of the total strain on the membranes. In Figure 5.17a-b the curves are shown for both geometries and materials investigated.

5.8. DISCUSSION AND CONCLUSIONS

The fabrication processes presented in this chapter enabled the development of both metallic and polymeric strain gauges as a potential transduction mechanism for *in situ*

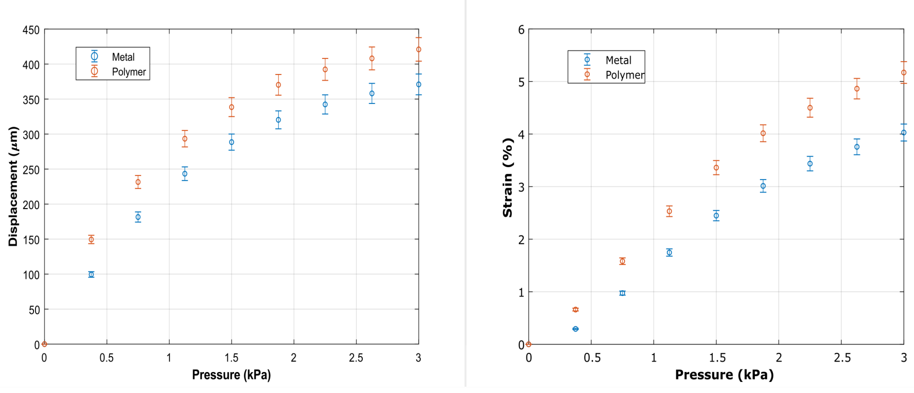

(a) **(b)**

Figure 5.16: **(a)** Displacement in the center of the membranes with metal and polymeric strain gauges measured optically for different pressures set through the pumping system (1-3 kPa). **(b)** Estimation of the radial strain of the membranes with strain gauges based on the displacement measurements.

monitoring of strain on PDMS membranes for OOC applications. The electrical resistance of the metallic strain gauges at the end of the fabrication was stable and did not show to be affected by the process. A slight deviation of approximately 2% compared to the designed values was measured. Both radial and tangential geometries (Fig. 5.6b) did not suffer any mechanical disruption after the releasing of the membrane, a critical step to realize the final devices. This demonstrated the robustness and reliability of the fabrication process developed.

The experimental data of resistance change for both metallic radial and tangential devices are within the same order of magnitude, as can be observed in Fig. 5.15. The results show a linear behaviour up to 3 kPa, pressure measurable and supplied by the pumping system. However, the data on the displacement shows a non-linear tendency for the same pressure range (Fig. 5.16), causing the non-linearities observed in the calibration curve for strains above 3 % (Fig. 5.17). This is due to the saturation of the displacement at the center of the membrane, which might be explained by the difference of a few orders of magnitude in stiffness between the membrane and the metal. Despite these non-linearities, a first linear approximation can be made to establish a transfer function for the actual strain on the membrane given certain resistance change. Thus, the estimated sensitivity for radial and tangential geometries for strains below 3 % is 4.5 $m\Omega\mu m^{-1}$ and 4.4 $m\Omega\mu m^{-1}$, respectively,

For polymeric strain gauges, the process was more challenging given the nature of the material. The main challenge encountered was to enable and optimize the electrical contact. As it was not possible to establish an ohmic contact using readily available metals (Al, Ti, TiN), the process needed to be adapted and optimized. To do so, it was redesigned to minimize long exposure of the materials to water as PEDOT:PPS is highly hygroscopic and degraded easily in contact with water. Given the characteristic reduction potential ($E^0 = +0.8V$) and the accessibility to Silver (Ag) deposition and patterning techniques, this material was used to create the electrical contacts. The addition of this

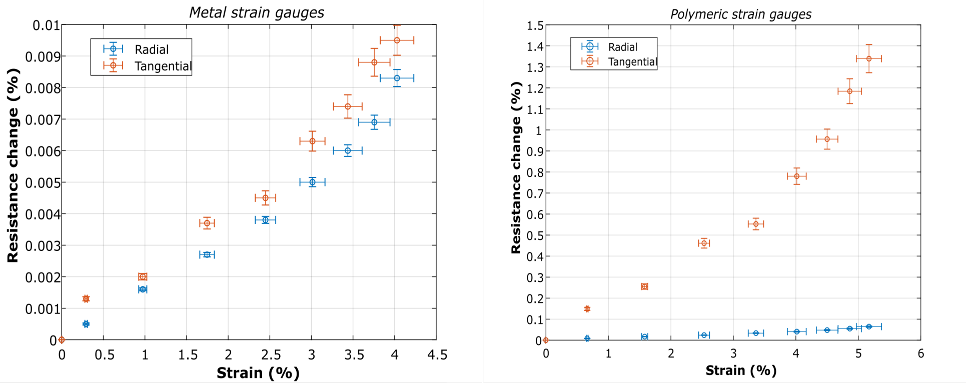

(a) **(b)**

Figure 5.17: Resistance change as function of the strain on the membrane for radial and tangential strain gauges made of**(a)** titanium (Ti) and **(b)** PEDOT:PSS.

material increased the number of steps and complexity of the process as the material is not standard in the facilities available. Thus, Aluminium was introduced as masking and protection layer so that the Ag contacts were never open when performing the lithography and dry etching steps, safeguarding the processing tools from possible exposure to Ag or unexpected back-sputtering.

Another aspect that was addressed, was the temperature and baking time of the polymer. The effect of these parameters on the electrical contact was investigated. By increasing the baking temperature to 150 °C and the baking time to 30 minutes, the contact resistance was decreased by 20 % compared to initial experiments. This indicates the importance of complete removal of water from the polymer to enhance electrical contact. It is worth mentioning that the measurements and fabrication were always carried out under controlled humidity conditions with relative humidity around 48%. Having a controlled humidity was important to keep the consistency of the experiments, as it has been shown that both electrical and mechanical properties of PEDOT:PSS might vary with humidity [17].

Regarding the electrochemical characterization of the polymeric strain gauges, the results also showed a measurable change in resistance of the microstructures when stretching the membrane. Particularly, a higher value of relative resistance change (up to 1.4 %) was observed compared to metal strain gauges. The tangential structures showed a higher value than radial structures. This might be correlated with the nature of PEDOT:PSS and the deposition technique used. The polymer has a structure of fibre-like chains with de-localized $\pi-$electrons that enable the conductivity. This suggest that the deposition technique might be inducing a radial arrangement of the fibers as consequence of the spinning, leading to higher resistance changes when stretched. Significant degradation of the devices was observed with stretching and time, suggesting still the need of optimizing the patterning of PEDOT:PSS microstructures and a proper characterization of the dependence of mechanical properties with environmental conditions. Alternative depositions, such as electro-deposition and encapsulation of the material can be explored to address this issue. Despite this, it is possible to establish a preliminary linear approximation for the transfer function of polymeric strain gauges. In this case the sensitivity of 0.571 $\Omega \mu m^{-1}$ and 62 $\Omega \mu m^{-1}$ for radial and tangential geometries, are obtained respectively for strains below 3 %. This indicates a much higher sensitivity for polymeric strain gauges. However, an extensive characterization on the stability with time and environmental conditions is necessary for these devices, specially under dynamic conditions typical of a cell culture to discard disruption of the mechanical and electrical performance.

REFERENCES

[1] A. van de Stolpe and J. den Toonder, *Workshop meeting report Organs-on-Chips: human disease models.* Lab on a chip **13**, 3449 (2013).

[2] R. R. Besser, M. Ishahak, V. Mayo, D. Carbonero, and I. Claure, *Engineered Microenvironments for Maturation of Stem Cell Derived Cardiac Myocytes,* Theranostics **8** (2018), 10.7150/thno.19441.

[3] T. Matsuda, K. Takahashi, T. Nariai, T. Ito, T. Takatani, Y. Fujio, and J. Azuma, *N-cadherin-mediated cell adhesion determines the plasticity for cell alignment in response to mechanical stretch in cultured cardiomyocytes,* Biochemical and Biophysical Research Communications **326**, 228 (2005).

[4] S. Dhein, A. Schreiber, S. Steinbach, D. Apel, A. Salameh, F. Schlegel, M. Kostelka, P. M. Dohmen, and F. Wilhelm, *Mechanical control of cell biology . Effects of cyclic mechanical stretch on cardiomyocyte cellular organization,* Progress in Biophysics and Molecular Biology **115**, 93 (2014).

[5] I. Banerjee, K. Carrion, R. Serrano, J. Dyo, R. Sasik, S. Lund, E. Willems, S. Aceves, R. Meili, M. Mercola, J. Chen, A. Zambon, G. Hardiman, T. A. Doherty, S. Lange, C. Juan, and V. Nigam, *Cyclic stretch of embryonic cardiomyocytes increases proliferation , growth , and expression while repressing Tgf- β signaling,* Journal of Molecular and Cellular Cardiology **79**, 133 (2015).

[6] R. E. Taylor, K. Kim, N. Sun, S. J. Park, J. Y. Sim, G. Fajardo, D. Bernstein, J. C. Wu, and B. L. Pruitt, *Sacrificial layer technique for axial force post assay of immature cardiomyocytes,* Biomedical Microdevices **15**, 171 (2013).

[7] T. Boudou, W. R. Legant, A. Mu, M. a. Borochin, N. Thavandiran, M. Radisic, P. W. Zandstra, J. a. Epstein, K. B. Margulies, and C. S. Chen, *A Microfabricated Platform to Measure and Manipulate the Mechanics of Engineered Cardiac Microtissues,* Tissue Engineering Part A **18**, 910 (2012).

[8] A. Gaitas, R. Malhotra, T. Li, T. Herron, and J. Jalife, *A device for rapid and quantitative measurement of cardiac myocyte contractility,* Review of Scientific Instruments **86** (2015), 10.1063/1.4915500.

[9] J. You, H. Moon, B. Y. Lee, J. Y. Jin, Z. E. Chang, S. Y. Kim, J. Park, Y. S. Hwang, and J. Kim, *Cardiomyocyte sensor responsive to changes in physical and chemical environments,* Journal of Biomechanics **47**, 400 (2014).

[10] B. Yuan, Y. Li, D. Wang, Y. Xie, Y. Liu, L. Cui, F. Tu, H. Li, H. Ji, W. Zhang, and X. Jiang, *A general approach for patterning multiple types of cells using holey PDMS membranes and microfluidic channels,* Advanced Functional Materials **20**, 3715 (2010).

[11] A. Mata, A. J. Fleischman, and S. Roy, *Characterization of polydimethylsiloxane (PDMS) properties for biomedical micro/nanosystems.* Biomedical microdevices **7**, 281 (2005).

[12] Y. Hongbin, Z. Guangya, C. F. Siong, W. Shouhua, and L. Feiwen, *Novel polydimethylsiloxane (PDMS) based microchannel fabrication method for lab-on-a-chip application,* Sensors and Actuators, B: Chemical **137**, 754 (2009).

[13] E. Berthier, E. W. K. Young, and D. Beebe, *Engineers are from PDMS-land, Biologists are from Polystyrenia,* Lab on a Chip **12**, 1224 (2012).

[14] S. Khoshfetrat Pakazad, a. Savov, a. van de Stolpe, and R. Dekker, *A novel stretchable micro-electrode array (SMEA) design for directional stretching of cells,* Journal of Micromechanics and Microengineering **24**, 034003 (2014).

[15] N. Gaio, B. V. Meer, W. Q. Solano, L. Bergers, A. V. D. Stolpe, C. Mummery, P. M. Sarro, and R. Dekker, *Cytostretch , an Organ-on-Chip Platform,* Journal of Micromachines , 1 (2016).

[16] M. Elwenspoek, F. R. Blom, S. Bouwstra, T. S. J. Lammerink, F. C. M. van de Pol, H. A. C. Tilmans, T. J. A. Popma, and J. H. J. Fluitman, *Transduction mechanisms and their applications in micromechanical devices,* in *IEEE Micro Electro Mechanical Systems, , Proceedings, 'An Investigation of Micro Structures, Sensors, Actuators, Machines and Robots'* (1989) pp. 126–132.

[17] W. K. Schomburg, Z. Rummler, P. Shao, K. Wulff, and L. Xie, *The design of metal strain gauges on diaphragms,* Journal of Micromechanics and Microengineering **14**, 1101 (2004).

[18] S. Timoshenko and S. Woinowsky-Krieger, *Theory of Plates and Shells, (Engineering Societies Monographs)* (McGraw-Hill College, 1959).

[19] A. Chouaf, C. Malhaire, M. L. Berre, M. Dupeux, F. Pourroy, and D. Barbier, *Stress analysis at singular points of micromachined silicon membranes* (Elsevier Science, 2000) pp. 109–115.

[20] V. A. Gridchin, V. V. Grichenko, and V. M. Lubimsky, *Square-Membrane Deflection and Stress : Identifying the Validity Range of a Calculation Procedure,* Rusian Microelectronics **34**, 210 (2005).

[21] B. D. Ratner, *A perspective on titanium biocompatibility,* in *Titanium in Medicine: Material Science, Surface Science, Engineering, Biological Responses and Medical Applications* (Springer Berlin Heidelberg, Berlin, Heidelberg, 2001) pp. 1–12.

[22] P. Schmid, C. Zarfl, G. Balogh, and U. Schmid, *Gauge factor of titanium/platinum thin films up to 350řC,* Procedia Engineering **87**, 172 (2014).

[23] N. Dam Madsen, M. Hausladen, S. Chiriaev, P. Johannesen, Z. E. Fabrim, P. F. Fichtner, and J. Kjelstrup-Hansen, *Titanium nitride as a strain gauge material,* Journal of Microelectromechanical Systems **25**, 683 (2016).

[24] R. Millard, G. Bond, and J. Toole, *Implementation of a titanium strain gauge pressure transducer for CTD applications,* Deep-Sea Research Part I **40**, 1009 (1993).

[25] U. Heckmann, R. Bandorf, H. Gerdes, M. Lübke, S. Schnabel, and G. Bräuer, *New materials for sputtered strain gauges,* Procedia Chemistry **1**, 64 (2009).

[26] U. Lang, N. Naujoks, and J. Dual, *Mechanical characterization of PEDOT:PSS thin films,* Synthetic Metals **159**, 473 (2009).

[27] Y. Li, Y. Masuda, Y. Iriyama, and H. Okuzaki, *Stretchable and Highly Conductive Polymer Films,* Trans. Mat. Res. Soc. Japan **37**, 303 (2012).

[28] F. Greco, A. Zucca, S. Taccola, A. Menciassi, T. Fujie, H. Haniuda, S. Takeoka, P. Dario, and V. Mattoli, *Ultra-thin conductive free-standing PEDOT/PSS nanofilms,* Soft Matter **7**, 10642 (2011).

[29] C. K. Cho, W. J. Hwang, K. Eun, S. H. Choa, S. I. Na, and H. K. Kim, *Mechanical flexibility of transparent PEDOT:PSS electrodes prepared by gravure printing for flexible organic solar cells,* Solar Energy Materials and Solar Cells **95**, 3269 (2011).

[30] G. Latessa, F. Brunetti, a. Reale, G. Saggio, and a. Di Carlo, *Piezoresistive behaviour of flexible PEDOT:PSS based sensors,* Sensors and Actuators, B: Chemical **139**, 304 (2009).

[31] N. Trifigny, F. M. Kelly, C. Cochrane, F. Boussu, V. Koncar, and D. Soulat, *PEDOT:PSS-based piezo-resistive sensors applied to reinforcement glass fibres for in situ measurement during the composite material weaving process.* Sensors (Basel, Switzerland) **13**, 10749 (2013).

[32] U. Lang, P. Rust, B. Schoberle, and J. Dual, *Piezoresistive properties of PEDOT:PSS,* Microelectronic Engineering **86**, 330 (2009).

[33] T. K. Kim, J. K. Kim, and O. C. Jeong, *Microelectronic Engineering Measurement of nonlinear mechanical properties of PDMS elastomer,* Microelectronic Engineering **88**, 1982 (2011).

[34] I. D. Johnston, D. K. McCluskey, C. K. L. Tan, and M. C. Tracey, *Mechanical characterization of bulk Sylgard 184 for microfluidics and microengineering,* Journal of Micromechanics and Microengineering **24**, 035017 (2014).

[35] T. Tsuchiya, M. Hirata, and N. Chiba, *Young's modulus, fracture strain, and tensile strength of sputtered titanium thin films,* Thin Solid Films **484**, 245 (2005).

[36] E. Voroshazi, B. Verreet, A. Buri, R. Müller, D. Di Nuzzo, and P. Heremans, *Influence of cathode oxidation via the hole extraction layer in polymer:fullerene solar cells,* Organic Electronics: physics, materials, applications **12**, 736 (2011).

6

CONCLUSIONS AND RECOMMENDATIONS

6.1. GENERAL CONCLUSIONS

6.1.1. ORGANS-ON-CHIPS

Advances in tissue engineering and microfabrication have made possible to realize Organs-on-Chips (OOCs). These customized cell culture microenvironments are becoming a reliable alternative to conventional static cell cultures and animal testing in drug development. This cutting edge technology has already enabled a better understanding of infection mechanisms, tumour metastasis and stem cell technology. At the same time, OOC opens promises to bring the highly envisioned personalized medicine a step forward.

However, most of these devices are fabricated by soft lithography, as this enabled biologists rapid prototyping microstructures resembling human organs. This fabrication technique has intrinsic limits on the feature sizes achievable and on scalability, thus hampering the widespread use in the drug development pipeline. Alternatively, using IC and MEMS microfabrication techniques makes possible to develop microstructures to mimic the minimal unit of human organs with higher accuracy, reliability and reproducibility. Moreover, with these techniques Organs-on-Chips can be complemented with self-integrated sensors and actuators. Bringing their fabrication closer to such well known techniques will allow to have a manufacturable and cost-effective production, creating an alternative and reliable tools for applications beyond fundamental biology research.

6.1.2. MICROFABRICATED POROUS PDMS MEMBRANES

Chapter 3 has demonstrated a simple and reproducible method to fabricate and transfer porous PDMS membranes with a high control on pore size, porosity, thickness, thus reducing the risks involved in integrating fragile membranes into OOCs. The fabrication and transfer method circumvent the limitation imposed by manual handling of other assembly and fabrication methods, while keeping the well-known mechanical and optical advantages PDMS offers for cell culturing.

It has been shown that very thin (thickness <10 μm) porous membranes with small features sizes down to 2 μm and porosity up to 65% can be fabricated and successfully transferred to a OOC device with high reproducibility and high yield (≥ 80 %). The results obtained suggest that the microfabrication and transfer method provide an opportunity to develop these devices with higher quality and reproducibility of the physical and topographical properties of the membrane used as barrier to model certain physiological activities. The results on cell transmigration, topology and barrier formation demonstrated the biocompatibility of the porous PDMS membranes. Moreover, they contribute to highlight the importance of considering the accurate control of the pore features as a design variable when developing devices that represent more closely the conditions of interest.

6.1.3. SILICON/POLYMER-BASED ORGAN-ON-CHIP DEVICE

Chapter 4 demonstrates the monolithic microfabrication of a OOC device with a variety of potential applications. The microfuidic channel is suitable to provide perfusion to two different cells cultured in two separate compartments delimited by the porous PDMS membranes. This enables to mimic vasculature and investigate further new cell mechanisms and diseases mechanisms. Preliminary biological experiments demonstrated its biocompatibility as cells were successfully cultured in the microchannels and the silicon cavity. To do so, two different cell types were used, human umbilical vein endothelial cells (HUVECs) and cardiomyocytes (CM).

Moreover, unlike most OOCs, the device along with its interface allows to accomodate other structures such as organoids or tissue slices with thickness up to few centimetres and lengths up to 8 mm. Structures needing more development in the z axis such in gut-on-chip, might be implemented with the proposed device. The interface developed to connect the microchannel to external hydraulic circuitry is easy to use and compatible with standardised microfluidic connectors and tubing, which facilitates its initial adoption for both research as well as for further commercial implementation in the drug development pipeline.

6.1.4. MICROSTRUCTURES FOR MECHANICAL SENSING

So far, the majority of OOCs have relied entirely on bulk optical techniques (immunofluorescence end-point detection, microscope cell imaging) to acquire and analyse the information of cultured microenvironments. The limitation of these techniques appears when specific data is missing due to the intrinsic inability of purely optical methods to capture biological phenomenon that involve also mechanical, chemical and topographical cues. A more complete view of cell responses can be obtained if mechanical strain, bioelectrical activities, pH level, potassium and oxygen concentration could be quantitatively measured in a spatio-temporal manner in a culture.

Chapter 5 reports on the successful wafer-scale microfabrication processes developed for metal and polymeric strain gauges on 9 μm-thick PDMS membranes for cell culture microenvironments. The results indicate that both conventional IC metals (Ti) and polymeric materials (PEDOT:PSS) can be used in microfabrication processes in devices for sensing mechanical cues. The results showed the successful patterning of PEDOT:PSS microstructures with a good electrical conductivity and in a variety of features and sizes. The achieved results clearly indicate that this material can be effectively included in microfabrication processes.

The transduction behaviour and functionality of the devices was preliminarily proven. A custom made set-up allows to show a resistance change of the devices for different pressures applied to the membranes, demonstrating the functionality of the proposed device. Relative resistance changes of approximately 0.008% and 1.2% for titanium and polymeric strain gauges have been observed, respectively. This for pressures up to 3 kPa applied to stretch the membranes. Correspondingly, the displacement measurements showed that for such resistance changes a strain of up to ≈4 % is induced on the membrane. Devices with transfer functions showing sensitivities of up to 62 $\Omega \cdot \mu m^{-1}$, as is the case of the preliminary results of the polymeric strain gauges. In both metallic and polymeric devices, the tangential geometry showed higher sensitivity.

6.2. RECOMMENDATIONS AND FUTURE WORK

Future work is necessary to bring the devices presented in this thesis to its full use in drug development and specially to improve its performance and fully exploit the capabilities of IC amd MEMS fabrication techniques. Following some recommendations that will enhance further the reliability and impact of the results obtained:

- Generally, both academia and industry must increase the efforts to develop scalable fabrication processes of Organs-on-Chips at early stages of research to have a manufacturable and cost-effective production, thus creating an alternative and reliable tools for applications beyond fundamental biology research.
- In the fabrication of porous membranes, further work is necessary to evaluate the transfer method at wafer scale. If this is demonstrated, the transfer process might be adapted to automated assembling techniques, contributing even more to the scalability of the assembly of conventional OOCs towards more reproducible and high throughput manufacturing.
- Further work is necessary to fully validate the Silicon/polymer-based Organ-on-Chip device with different cell lines and probe the advantages of the stimulation cues provided by the device, strengthening this contribution as a first demonstration of a highly reliable, manufacturable and monolithically fabricated OOCs.
- Further electrical and mechanical investigation on the operation of the strain gauges is necessary to evaluate the dynamic response of the devices and the reliability for long term experiments. Specially, experimental data on the mechanical properties of the materials and the real distribution of the strain in the microstructures will give a better understanding and fully demonstrate the sensing functionality of the devices. Moreover, the development of a proper packaging would help to increase the robustness and reliability of the devices, namely a better interfacing between the membranes and the pumping system. Regarding the circuitry, including the the Wheatstone bridge and the amplification phase in the fabrication process will contribute even further the advantages of using IC and MEMS techniques for developing OOCs.

A

APPENDIX A

A.1. FLOW VELOCITY IN A FINITE RECTANGULAR MICROCHANNEL

The analytical solution for the velocity field of Navier-Stokes equations has been already reported in literature[1]. Following is the described mathematical procedure to obtain the velocity field, which is used in this thesis to design the microchannels of Chapter 4. Considering the geometry shown in Figure 4.2 centred in the origin, Eqs. 4.3 and 4.4 and the boundary conditions

$$[\partial_y^2 + \partial_z^2]\mathbf{v}_x(y,z) = -\frac{\Delta p}{\eta L}, \text{ for } -\frac{1}{2}w < y < \frac{1}{2}w, 0 < z < h, \tag{A.1}$$

$$\mathbf{v}_x(y,z) = 0, \text{ for } y = \pm\frac{1}{2}w, z = 0, z = h. \tag{A.2}$$

where w and h are the width and height of the rectangular channel.

Expanding all functions of Eqs. A.1 and A.2 as Fourier series along the vertical direction (z)

$$-\frac{\Delta p}{\eta L} = -\frac{\Delta p}{\eta L}\sum_{n,odd}^{\infty}\frac{1}{n}\sin\left(n\pi\frac{z}{h}\right) \tag{A.3}$$

$$\mathbf{v}_x(y,z) = \sum_{n=1}^{\infty} f_n(y)\sin\left(n\pi\frac{z}{h}\right) \tag{A.4}$$

To make sure that the boundary conditions are fulfilled, the left side of equation A.1 can be expressed as

$$[\partial_y^2 + \partial_z^2]\mathbf{v}_x(y,z) = \sum_{n=1}^{\infty}\left[f_n''(y) - \frac{n^2\pi^2}{h^2}f_n(y)\right]\sin\left(n\pi\frac{z}{h}\right) \tag{A.5}$$

---

[1] H. Bruss,Microscale Acoustofluidics (Royal Society of Chemistry, 2014).

In order to find the function $f_n(y)$, the terms with coefficients n from Eqs. A.3 and A.5 must be equal for any value n. This condition leads to a system of equations

$$f_n(y) = 0, \text{ for } n \text{ even,} \tag{A.6}$$

$$f_n''(y) - \frac{n^2\pi^2}{h^2} f_n(y) = -\frac{\Delta p}{\eta L}\frac{4}{\pi}\frac{1}{n}, \text{ for } n \text{ odd} \tag{A.7}$$

Considering Eq.A.7 an inhomogeneous second order differential equation with general solution

$$f_n(y) = f_n^{inhomogeneous}(y) + f_n^{homogeneous}(y) \tag{A.8}$$

Considering a simple case in which $f_n^{inhomogeneous}(y) = constant$ a particular solution to the inhomogeneous equation can be found, by inserting $f_n^{inhomogeneous}(y)$ in Eq.A.7

$$f_n^{inhomogeneous}(y) = \frac{4h^2\Delta p}{\pi^3\eta L n^3}, \text{ for } n \text{ odd} \tag{A.9}$$

On the other side, the solution to the homogeneous equation is obtained by making zero the right side of Eq.A.7, which leads to the general solution given by the linear combination

$$f_n^{homogeneous}(y) = A\cosh\left(\frac{n\pi}{h}y\right) + B\sinh\left(\frac{n\pi}{h}y\right) \tag{A.10}$$

Thus, by considering the boundary condition that establishes that the velocity field is zero at the walls of the microchannel, the parameters (A,B) can be found and a final expression for the function $f_n(y)$ is given by

$$f_n(y) = \frac{4h^2\Delta p}{\pi^3\eta L n^3}\left[1 - \frac{\cosh\left(\frac{n\pi}{h}y\right)}{\cosh\left(\frac{n\pi}{2h}y\right)}\right], \text{ for } n \text{ odd} \tag{A.11}$$

Thus, inserting Eq.A.11 in Eq.A.4, the final expression of the velocity field in a rectangular channel is obtained

$$\mathbf{v}_x(y,z) = \frac{4h^2\Delta p}{\pi^3\eta L}\sum_{n,odd}^{\infty}\frac{1}{n^3}\left[1 - \frac{\cosh\left(\frac{n\pi}{h}y\right)}{\cosh\left(\frac{n\pi}{2h}y\right)}\right]\sin\left(n\pi\frac{z}{h}\right) \tag{A.12}$$

A.2. FLOWRATE IN A FINITE RECTANGULAR MICROCHANNEL

Once known an analytical expression for the velocity field in a rectangular microchannel, the flow can be found by integration as given by

$$Q = \iint_V \mathbf{v}_x(y,z)\cdot dy\,dz = 2\int_0^{\frac{1}{2}w} dy \int_0^h \mathbf{v}_x(y,z)\,dz \tag{A.13}$$

Considering the expression of the velocity field given in Eq.A.12 and inserting it in Eq.A.13

$$Q = 2\frac{4h^2\Delta p}{\pi^3\eta L}\int_0^{\frac{1}{2}w} dy \int_0^h \sum_{n,odd}^{\infty}\frac{1}{n^3}\left[1-\frac{\cosh\left(\frac{n\pi}{h}y\right)}{\cosh\left(\frac{n\pi}{2h}y\right)}\right]\sin\left(n\pi\frac{z}{h}\right)dz \tag{A.14}$$

After the double integration, considering that in the limit $\frac{h}{w}\longrightarrow 0$

$$\sum_{n,odd}^{\infty}\frac{1}{n^4}=\frac{\pi^4}{96} \tag{A.15}$$

and the Riemann zeta function

$$\varsigma(a)\equiv\sum_{n=1}^{\infty}\frac{1}{n^a} \tag{A.16}$$

The expression for the flowrate is simplified to

$$Q=\frac{h^3 w\Delta p}{12\eta L}\left[1-\frac{192}{\pi^5}\frac{31}{32}\varsigma(5)\frac{h}{w}\right] \tag{A.17}$$

$$Q=\frac{h^3 w\Delta p}{12\eta L}\left[1-0.630\frac{h}{w}\right] \tag{A.18}$$

B

APPENDIX B

In this appendix, a detailed description of the steps of the process flows is given. The fabrication process of the porous PDMS, and the metal and polimeric strain gauges are particularly given.

The starting material of the fabrication processes of all devices correspond to 100 mm in diameter and 525 μm thick Silicon wafers, p-type, with orientation $< 100 >$ and resistivity 2-5 Ωcm. Before starting any of the process here detailed, the wafers were cleaned as following:

Full cleaning

- 10 minutes in fuming nitric acid (HNO_3,99 %) at ambient pressure.
- Rinsing in DI (deionized water) water for 10 min or monitoring resistivity until it reaches $5M\Omega$.
- 10 minutes in concentrated nitric acid (HNO_3,69.5 %) at 110 °C.
- Rinsing in DI (deionized water) water for 10 min or monitoring resistivity until it reaches $5M\Omega$.
- Drying of the wafers in a centrifuge-based dryer.

B.1. FLOWCHART - POROUS PDMS MEMBRANES

Once the first cleaning step is done, the following steps comprehend the process flow of the porous PDMS membranes (Chapter 3, Section 3.2.1).

1. *Alignment marks on the back:*
    (a) Coating: A 1,5 μm photoresist is deposited on the back-side of the wafer.
    (b) The coated substrate is exposed to create alignment marks for both contact aligner and stepper.

   - (c) The substrate is baked after exposure (115 °C) and develop for 90 seconds using MF322 developer.
   - (d) After optical inspection, the open areas of silicon are etched with Reactive Ion Etching(RIE) using a $CF_4/O_2/Cl_2/HBr$-based plasma (Omega).

2. *Removal of photoresist and full cleaning (See Full cleaning).*

3. *Deposition of Silicon Oxide (SiO_2) or Poly(acrylic acid)(PAA) on the front:*
   - (a) A 2 μm-thick silicon oxide thick is deposited using PECVD when suspended membranes (3.3) are to be fabricated.
   - (b) If the membranes are meant to be transferred (3.4), a sacrificial later (PAA) is deposited by spin coating at 4000 rpm for 40 s and baked in a temperature controlled oven at 100 °C for 2 h (Go to step 7).

4. *Deposition of Silicon Oxide (SiO_2) on the back:*
   - (a) A 6 μm-thick silicon oxide thick is deposited using PECVD when suspended membranes (3.3) are to be fabricated.
   - (b) If the membranes are meant to be transferred(3.4) this step is not necessary.

5. *Patterning of the Silicon Oxide (SiO_2) on the back:*
   - (a) A 3 μm-thick photoresist is deposited on the back-side of the wafer using no-edge removal (no-EBR).
   - (b) The coated substrate is exposed to defined the membrane area using a contact aligner.
   - (c) The substrate is baked after exposure (115 °C) and develop for 180 seconds using MF322 developer.
   - (d) The silicon oxide layer is etched for 12 minutes with RIE using a C_2F_6/CHF_3-based plasma (Drytek).

6. *Removal of photoresist and full cleaning (See Full cleaning).*

7. *Deposition of PDMS:*
   - (a) The base elastomer and the curing agent of PDMS are mixed a 10:1 ratio.
   - (b) A PDMS layer is deposited by two-step spin coating, the first spreading step at 300 rpm and the second step at 6000 rpm.
   - (c) The PDMS is baked for 1h at 90°C.

8. *Patterning of PDMS:*
   - (a) After baking of the PDMS (preferably within the next 3 hours), a masking layer is deposited by sputtering. Aluminum (Al) with 1 % silicon (Si) is used. Given the nature of PDMS, prior starting the deposition process a special procedure (leak-up rate test) is necessary to avoid degassing. To do so, the substrate needs to be input inside the deposition chamber under vacuum while

continuously monitoring the pressure of the chamber for 10 min. The initial and final pressure of the chamber is recorded and the leak-up rate calculated based on these values and the volume of the chamber. If the leak-up rate is below the established by the facilities ($< 2x10^{-6} Tls^{-1}$), the deposition can be safely done.

(b) After the leak-up rate test, 250 nm of Al/Si are sputtered at room temperature.

(c) A 2 μm-thick photoresist is deposited on the Al/Si-coated PDMS.

(d) The coated substrate is exposed to defined the membrane area using a contact aligner .

(e) The substrate is baked after exposure (115 °C) and develop for 90 seconds using MF322 developer.

(f) After optical inspection, the open areas of the Al are etched with Reactive Ion Etching(RIE) using a Cl_2-based plasma (Omega).

(g) Subsequently, the PDMS is etched using the Al/Si as mask. The etching is done with Reactive Ion Etching(RIE) using a CF_4-based plasma (Omega). Special attention should be paid to make sure the PDMS has been completely etched. If the porous PDMS is meant to be transferred, go to step 10.

9. *Release of the porous PDMS:*

   (a) If the porous membranes are meant to be suspended, the Al/Si layer after etching of the PDMS should be kept.

   (b) The silicon is etched from the back of the wafer by DRIE using a Bosh process (Rapier).

   (c) The landing layer (Step 3.a) is them removed by we etching using BHF (use dedicated bath).

   (d) The Al/Si masking layer is then removed by wet etching using PES, resulting in the final porous membranes suspended from the silicon substrate.

10. *Transfer of the porous PDMS to an OOC:*

   (a) If the porous membranes are meant to be transferred to a PDMS-based OOC, the Al/Si layer should be removed by wet etching using PES (use dedicated bath).

   (b) The OOC part and the porous PDMS need to be treated by oxygen plasma to activate the surface and guarantee their mechanical bonding.

   (c) The porous PDMS and the OOC bottom substrate are brought together for several hours to create the bonding.

   (d) Both the porous PDMS and the OOC are submerged in either water or acetone using an ultrasonic bath for 10 min. This leaves to the detachment of the silicon substrate and transfer of the porous PDMS to the OOC device.

B.2. FLOWCHART - TI STRAIN GAUGES

Once the first cleaning step is done, the following steps comprehend the process flow of the Ti Strain Gauges (Chapter 5, Section 5.5.1).

1. *Alignment marks on the front:*
    (a) Coating: A 1,5 μm photoresist is deposited on the front-side of the wafer.
    (b) The coated substrate is exposed to create alignment marks for both contact aligner and stepper.
    (c) The substrate is baked after exposure (115 °C) and develop for 90 seconds using MF322 developer.
    (d) After optical inspection, the open areas of silicon are etched with Reactive Ion Etching(RIE) using a $CF_4/O_2/Cl_2/HBr$-based plasma (Omega).
2. *Removal of photoresist and full cleaning (See Full cleaning).*
3. *Alignment marks on the back:*
    (a) Coating: A 1,5 μm photoresist is deposited on the back-side of the wafer.
    (b) The coated substrate is exposed to create alignment marks for both contact aligner and stepper.
    (c) The substrate is baked after exposure (115 °C) and develop for 90 seconds using MF322 developer.
    (d) After optical inspection, the open areas of silicon are etched with Reactive Ion Etching(RIE) using a $CF_4/O_2/Cl_2/HBr$-based plasma (Omega).
4. *Removal of photoresist and full cleaning (See Full cleaning).*
5. *Deposition of Silicon Oxide (SiO_2) on the front:*
    (a) A 2 μm-thick silicon oxide thick is deposited using PECVD to be used as landing layer.
6. *Deposition of Silicon Oxide (SiO_2) on the back:*
    (a) A 6 μm-thick silicon oxide thick is deposited using PECVD to be used as the mask to define the circular membranes area (5.5.1).
7. *Patterning of the Silicon Oxide (SiO_2) on the back:*
    (a) A 3 μm-thick photoresist is deposited on the back-side of the wafer using no-edge removal (no-EBR).
    (b) The coated substrate is exposed to defined the membrane area using a contact aligner.
    (c) The substrate is baked after exposure (115 °C) and develop for 180 seconds using MF322 developer.

   (d) The silicon oxide layer is etched for 12 minutes with RIE using a C_2F_6/CHF_3-based plasma (Drytek).

8. *Removal of photoresist and full cleaning (See Full cleaning).*

9. *Polyimide (PI) deposition and patterning.*

   (a) A 600 nm-thick PI layer is deposited by two-step spin coating, the first spreading step at 300 rpm for 5 sec and the second step at 2000 rpm for 30 seconds. The PI used is photosensitive, which enables to use photolithography to pattern it more easily. After deposition, a soft-bake at 100 °C is done in a hotplate.

   (b) The PI-coated substrate is exposed for 15 sec to defined the strain gauges using a contact aligner (EC1940-V1-Gauge).

   (c) The substrate is baked after exposure (90 °C) and develop for 90 seconds. Avoid contact with water while developing if the development is not complete after the time specified.

   (d) The PI layer is hard-baked for 4 h in a vacuum oven at 350 °C.

10. *Deposition and patterning of Titanium and Aluminium (Strain gauges and contacts)*

   (a) After baking of the PI the metal layers (Ti, Al/Si) corresponding to the strain gauges and the contacts are deposited by sputtering. Given the nature of PI, prior starting the deposition process the leak-up rate test is necessary to avoid degassing.

   (b) After the leak-up rate test, 200 nm of Ti and 600 n of Al/Si are sputtered at room temperature.

   (c) A 2 μm-thick photoresist is deposited on the metal stack (AlSi/Ti) using no-edge removal (no-EBR).

   (d) The coated substrate is exposed to defined the area of the electrical contacts using a contact aligner.

   (e) The substrate is baked after exposure (115 °C) and develop for 180 seconds using MF322 developer.

   (f) The Al/Si layer is selectively etched by wet etching using PES, leaving the Al/Si contacts patterned.

   (g) The photoresist is removed in an acetone bath at 40 °C for 3 minutes. The substrate is quickly ($\approx$ 30 s) cleaned (HNO_3,99 %) and rinsed with DI water.

   (h) A 2 μm-thick photoresist on the metal Ti and Al contacts is deposited using no-edge removal (no-EBR and Topo).

   (i) The substrate is baked after exposure (115 °C) and develop for 180 seconds using MF322 developer.

   (j) After optical inspection, the Ti layer is etched with Reactive Ion Etching(RIE) using a $CF_4/O_2/Cl_2/HBr$-based plasma (Omega).

11. *Removal of photoresist (Flash, Oxygen plasma) and cleaning (HNO_3,99 %,30 sec).*

12. *Deposition of PDMS:*
    (a) The base elastomer and the curing agent of PDMS are mixed a 10:1 ratio.
    (b) A PDMS layer is deposited by two-step spin coating, the first spreading step at 300 rpm and the second step at 6000 rpm.
    (c) The PDMS is baked for 1h at 90°C.

13. *Patterning of PDMS for opening electrical contacts:*
    (a) After baking of the PDMS (preferably within the next 3 hours), a masking layer (Al/Si) is deposited by sputtering and used to etched the PDMS to open the electrical contacts of the strain gauges. Prior starting the deposition the leak-up rate test is necessary to avoid degassing.
    (b) After the leak-up rate test, 250 nm of Al/Si are sputtered at room temperature.
    (c) A 2 μm-thick photoresist is deposited on the Al/Si-coated PDMS.
    (d) The coated substrate is exposed to define contacts area using a contact aligner.
    (e) The substrate is baked after exposure (115 °C) and develop for 90 seconds using MF322 developer.
    (f) After optical inspection, the open areas of the Al are etched with Reactive Ion Etching(RIE) using a Cl_2-based plasma (Omega).
    (g) Subsequently, the PDMS is etched using the Al/Si as mask. The etching is done with Reactive Ion Etching(RIE) using a CF_4-based plasma (Omega). Special attention should be paid to make sure the PDMS has been completely etched and guarantee ohmic contact during characterization.

14. *Release of the PDMS membranes with strain gauges:*
    (a) The silicon is etched from the back of the wafer by DRIE using a Bosh process (Rapier).
    (b) The landing layer (Step 3.a) is them removed by a combination of wet and dry etching using BHF (use dedicated bath) and a CF_4-based plasma.
    (c) The Al/Si masking layer is then removed by wet etching using PES (use dedicated bath), resulting in the final membranes with strain gauges. This step should be made carefully to avoid removing the aluminium contacts, constant visual inspection is necessary to stop the etching process on time.

B.3. FLOWCHART - PEDOT:PSS STRAIN GAUGES

Once the first cleaning step is done, the following steps comprehend the process flow of the Ti Strain Gauges (Chapter 5, Section 5.5.2).

1. *Alignment marks on the front:*
   - (a) Coating: A 1,5 μm photoresist is deposited on the front-side of the wafer.
   - (b) The coated substrate is exposed to create alignment marks for both contact aligner and stepper.
   - (c) The substrate is baked after exposure (115 °C) and develop for 90 seconds using MF322 developer.
   - (d) After optical inspection, the open areas of silicon are etched with Reactive Ion Etching(RIE) using a $CF_4/O_2/Cl_2/HBr$-based plasma (Omega).
2. *Removal of photoresist and full cleaning (See Full cleaning).*
3. *Alignment marks on the back:*
   - (a) Coating: A 1,5 μm photoresist is deposited on the back-side of the wafer.
   - (b) The coated substrate is exposed to create alignment marks for both contact aligner and stepper.
   - (c) The substrate is baked after exposure (115 °C) and develop for 90 seconds using MF322 developer.
   - (d) After optical inspection, the open areas of silicon are etched with Reactive Ion Etching(RIE) using a $CF_4/O_2/Cl_2/HBr$-based plasma (Omega).
4. *Removal of photoresist and full cleaning (See Full cleaning).*
5. *Deposition of Silicon Oxide (SiO_2) on the front:*
   - (a) A 2 μm-thick silicon oxide thick is deposited using PECVD to be used as landing layer.
6. *Deposition of Silicon Oxide (SiO_2) on the back:*
   - (a) A 6 μm-thick silicon oxide thick is deposited using PECVD to be used as the mask to define the circular membranes area (5.5.1).
7. *Patterning of the Silicon Oxide (SiO_2) on the back:*
   - (a) A 3 μm-thick photoresist is deposited on the back-side of the wafer using no-edge removal (no-EBR).
   - (b) The coated substrate is exposed to defined the membrane area using a contact aligner.
   - (c) The substrate is baked after exposure (115 °C) and develop for 180 seconds using MF322 developer.

   (d) The silicon oxide layer is etched for 12 minutes with RIE using a C_2F_6/CHF_3-based plasma (Drytek).

8. *Removal of photoresist and full cleaning (See Full cleaning).*

9. *Deposition of Silver (Ag) contacts:*

   (a) A 3 μm-thick negative photoresist is deposited on the front-side of the wafer using no-edge removal (no-EBR).

   (b) The coated substrate is exposed to defined the contacts of the polymeric strain gauges.

   (c) The substrate is baked after exposure (115 °C) and develop for 180 seconds using MF322 developer.

   (d) The substrate is over expose to a deep UV treatment as the contacts are obtained through a lift-off process.

   (e) The open areas where the Ag is to be deposited are cleaned further with Oxygen plasma for 2 minutes at low power (Plasma flash).

   (f) A photoresist layer is deposited in the back of the wafer by manual spin coating.

   (g) The backside of the wafer is furthered protected with a double Al foil and the Ag layer (300 nm) is deposited by thermal evaporation. A Chromium (Cr) layer (50 nm) is used to improve adhesion of the metal with the substrate.

   (h) The resist and Al foil on the back of the wafer is removed for further processing.

   (i) The Ag layer is patterned by lift-off in an ultrasonic bath using NMP at 70 °C.

10. *Removal of photoresist (use dedicated equipment) and full cleaning (Use dedicated baths).*

11. *Patterning of Al protection layer for electrical contacts:*

   (a) A 300 nm-thick layer of Aluminum (pure) is deposited by sputtering (with carrier wafer) at room temperature.

   (b) A 2 μm-thick photoresist is deposited (use dedicated holder) on the metal stack (Al/Ag) using no-edge removal (no-EBR).

   (c) The coated substrate is exposed to defined the area of the electrical contacts using a contact aligner (use dedicated holder).

   (d) The substrate is baked after exposure (115 °C) and develop for 180 seconds using MF322 developer (use dedicated hotplate).

   (e) The Al layer is selectively etched by wet etching using PES (use dedicated bath), leaving the Ag contacts accessible only in the areas where direct contact with PEDOT:SS is intended.

   (f) The photoresist is removed in an acetone bath at 40 °C for 3 minutes. The substrate is quickly ($\approx$ 30 s) cleaned (HNO_3,99 %, ue dedicated bath) and rinsed with DI water.

12. *Deposition of (PEDOT:PSS):*
    (a) PEDOT:PSS is available as a liquid solution. For pouring the material, 2 ml of the solution is necessary per wafer. Make sure the material is not expired and has been kept under the right temperature conditions. Before deposition make sure it is at room temperature and mix it properly.
    (b) The PEDOT:PSS layer is deposited by two-step spin coating, the first spreading step at 100 rpm and the second step at 2000 rpm.
    (c) The material is baked for 1h at 180°C in an over, preferably under vacuum.
13. *Patterning of PEDOT:PSS strain gauges:*
    (a) After baking of the PEDOT:PSS (preferably within the next 30 minutes), a masking layer (100 nm, Al/Si) is deposited by sputtering and used to etched the PDMS to open the electrical contacts of the strain gauges. Prior starting the deposition the leak-up rate test is necessary to avoid degassing.
    (b) After the leak-up rate test, 250 nm of Al/Si are sputtered at room temperature.
    (c) A 2 μm-thick photoresist is deposited on the Al/Si-coated PDMS.
    (d) The coated substrate is exposed to defined the strain gauges structures using a contact aligner (EC1940-V1-Gauge).
    (e) The substrate is baked after exposure (115 °C) and develop for 90 seconds using MF322 developer.
    (f) After optical inspection, the open areas of the Al are etched with Reactive Ion Etching(RIE) using a Cl_2-based plasma (Omega).
    (g) Subsequently, the PEDOT:PSS is etched with Reactive Ion Etching(RIE) using a O_2-based plasma (Omega). Special attention should be paid to make sure the PDMS has been completely etched and guarantee that the Al contacts don't have any residue.
    (h) The Al/Si masking layer is then removed by wet etching using PES (use dedicated bath), resulting in the PEDOT:PSS microstructures. This step should be made carefully to avoid removing the aluminium contacts, constant visual inspection is necessary to stop the etching process on time.
14. *Deposition of PDMS:*
    (a) The base elastomer and the curing agent of PDMS are mixed a 10:1 ratio.
    (b) A PDMS layer is deposited by two-step spin coating, the first spreading step at 300 rpm and the second step at 6000 rpm.
    (c) The PDMS is baked for 1h at 90°C.
15. *Patterning of PDMS for opening electrical contacts:*

   (a) After baking of the PDMS (preferably within the next 30 min), a masking layer (Al/Si) is deposited by sputtering and used to etched the PDMS to open the electrical contacts of the strain gauges. Prior starting the deposition the leak-up rate test is necessary to avoid degassing.
   (b) After the leak-up rate test, 250 nm of Al/Si are sputtered at room temperature.
   (c) A 2 μm-thick photoresist is deposited on the Al/Si-coated PDMS.
   (d) The coated substrate is exposed to define contacts area using a contact aligner.
   (e) The substrate is baked after exposure (115 °C) and develop for 90 seconds using MF322 developer.
   (f) After optical inspection, the open areas of the Al are etched with Reactive Ion Etching(RIE) using a Cl_2-based plasma (Omega).
   (g) Subsequently, the PDMS is etched using the Al/Si as mask. The etching is done with Reactive Ion Etching(RIE) using a CF_4-based plasma (Omega). Special attention should be paid to make sure the PDMS has been completely etched and guarantee ohmic contact during characterization.

16. *Release of the PDMS membranes with PEDOT:PSS strain gauges:*
   (a) The silicon is etched from the back of the wafer by DRIE using a Bosh process (Rapier).
   (b) The landing layer (Step 3.a) is them removed by a combination of wet and dry etching using BHF (use dedicated bath) and a CF_4-based plasma.
   (c) The Al/Si masking layer is then removed by wet etching using PES (use dedicated bath), resulting in the final membranes with the PEDOT:PSS strain gauges.

SUMMARY

Drug development is a complex, time-consuming (10 - 15 years) and expensive process. For a new medicine to reach the market, the net expenses covered by the pharmaceutical industry have been estimated to be around \$2.6 billion. Nevertheless, the risk of finding adverse effects or toxicity cases once the drug is already on the market is still high. Thus, pharmaceutical companies have been keenly looking forward to means to eliminate this at an early stage of the development process.

Recently, Organs-on-Chips (OOCs) emerged as a potential alternative to traditional drug screening. These devices, promise, in the middle-term, to enhance the *in vitro* screening and, in the long term, to reduce and eventually eliminate animal models in safety and efficacy essays. Nevertheless, the fabrication methods for most of these devices are hardly adaptable to scalable fabrication processes for *in vitro* screening application, as they rely strongly on manual techniques.

This thesis demonstrates the successful development of diverse microstructures for Organ-on-Chip applications by using scalable IC and MEMS-based fabrication techniques. Chapter 3 demonstrates the development of microfabricated porous PDMS membranes for barrier modelling. A simple and reproducible method to fabricate and transfer porous PDMS membranes with a high control on pore size, porosity, thickness, is shown. Very thin (thickness <10 μm) porous membranes with small features sizes down to 2 μm and porosity up to 65% can thus be fabricated and successfully transferred with high reproducibility. The presented results on cell transmigration, topology and barrier formation demonstrated the biocompatibility of the porous PDMS membranes.

Chapter 4 shows further efforts towards the realization of manufacturable OOCs. A monolithically microfabricated OOC device, an alternative to the available devices capable to address many more applications, was demonstrated. Preliminary biological experiments indicate its biocompatibility as cells (HUVEC, Cardyomyocites) are successfully cultured and maintained viable in the microchannels and the silicon cavity.

Finally, Chapter 5 demonstrates other possibilities allowed by the use of IC and MEMS techniques. The integration of microstructures that enable transduction mechanisms to monitor the cell microenvironment, is shown. Specifically, strain gauges for stress sensing as an alternative to monitor *in situ* strain in microfabricated OOCs, are presented. Relative resistance changes of approximately 0.008% and 1.2% for titanium and polymeric strain gauges have been observed, respectively.

The technological advances shown in this thesis form a significant contribution towards manufacturable fabrication of Organs-on-Chips and the standardization of OOCs as routinely used tools for drug development.

SAMENVATTING

De ontwikkeling van een medicijn is een tijdrovend (10 -15 jaar) en duur proces. De netto kosten voor een farmaceutisch bedrijf om een nieuw medicijn op de markt te brengen worden geschat op circa \$2.6 miljard. Desalniettemin is het risico op kwalijke bijwerkingen of vergiftigingsgevallen na introductie op de markt nog steeds hoog. Farmaceutische bedrijven kijken daarom reikhalzend uit naar een manier om dit in een vroeg stadium van het ontwikkelingsproces te vermijden.

Organen op een chip (OOC) zijn recentelijk verschenen als een potentieel alternatief voor de traditionele in vitro screening. Deze apparaten beloven in de nabije toekomst in vitro tests te verbeteren en op de lange termijn dierproeven te verminderen of zelfs overbodig te maken. Helaas zijn de productie methoden voor dergelijke apparaten voor in vitro analyse toepassingen nauwelijks geschikt voor schaalbare processen, aangezien deze methoden veelal handwerk vereisen.

Dit proefschrift demonstreert de succesvolle ontwikkeling van diverse microstructuren voor organen op een chip toepassingen door middel van schaalbare technologieën uit de halfgeleider industrie. Hoofdstuk 3 demonstreert de ontwikkeling van gemicrofabriceerde poreuze PDMS membranen voor het modelleren van barrières. Er wordt een simpele en reproduceerbare methode gepresenteerd om poreuze PDMS membranen te fabriceren en transfereren met goede controle van de grootte, porositeit en dikte. Zeer dunne (<10 μm dik) poreuze membranen met kleine structuren tot 2 μm en porositeit tot 65% kunnen gemaakt en getransfereerd worden met hoge reproduceerbaarheid. De resultaten van cel transmigratie, topologie en barrière formatie tonen de biocompatibiliteit van deze poreuze PDMS membranen aan.

Hoofdstuk 4 laat meer werk zien voor de realisatie van produceerbare OOCs. Een monolithisch gemicrofabriceerd OOC apparaat wat meer applicaties ondersteunt wordt gepresenteerd als alternatief voor de beschikbare apparaten. De eerste biologische experimenten tonen de biocompatibiliteit aan aangezien cellen (HUVEC, hartspiercellen) met succes gekweekt en in leven zijn gehouden in de microkanelen en de silicium holtes.

Als laatste demonstreert hoofdstuk 5 meer mogelijkheden met het gebruik van IC en MEMS technieken. De integratie van microstructuren voor transductie mechanismen om de micro-omgeving van de cel te monitoren is gedemonstreerd. Spanningsmeters worden gepresenteerd als alternatief om in situ spanning te meten in microgefabriceerde OOCs. Relatieve weerstand veranderingen van respectievelijk 0.008% en 1.2% voor titanium en polymerische spanningsmeters zijn waargenomen.

De in dit proefschrift gepresenteerde technologische voortgang is een significante toevoeging aan de fabricage van organen op een chip en de standaardisering van OOCs als routine gereedschap voor medicijn ontwikkeling.

CURRICULUM VITAE

William F. Quirós Solano was born in Turrialba, Costa Rica, in 1988. He received his B.Sc. degree in Electronics Engineering from Instituto Tecnológico de Costa Rica, Cartago, Costa Rica in 2011. The same year he joined the School of Electronic Engineering as research and teaching assistant.

In 2014 he received a M.Sc (cum laude) in Electronics Engineering with emphasis on Microelectromechanical Systems (MEMS). He received an scholarship from Instituto Tecnológico de Costa Rica to pursue his Ph.D degree at Delft University of Technology (TU Delft) at the Department of Microelectronics. His research focuses on Organ-on-Chip with particular interest in design, fabrication and characterization of novel microstructures for cell culture microenvironments. He is also co-founder of the Biotech spin-off BI/OND (BIOND Solutions B.V), which provides dynamic cell culture environments to recreate human physiology and pathology for predictive in-vitro assays.

He is currently a Post-Doctoral Researcher working on a collaborative project (Building Blocks of Life, BBOL) between TU Delft, Erasmus MC and Phillips Research.

LIST OF PUBLICATIONS

JOURNAL PAPERS

1. **W. F.Quirós-Solano**, N.Gaio, C. Silvestri, G.Pandraud, R. Dekker and P. M. Sarro. *Metal and polymer strain gauges for Si-based, monolithically fabricated Organs-on-Chips.* Micromachines, Submitted.

2. N.Gaio, A. Waafi, **W. F.Quirós-Solano**, P.Dijkstra, P.M.Sarro and R.Dekker. *Low-impedance PEDOT:PSS MEA integrated in an Organ-on-Chip Device.* IEEE Sensors Journal, Under Revision.

3. **W. F.Quirós-Solano**, N.Gaio, O. M. J.A. Stassen, Y. B.Arik, C. Silvestri, N.C.A.Van Engeland, A.Van der Meer, R. Passier, C. M. Sahlgren, C.V. C. Bouten, A. van den Berg, R. Dekker and P. M. Sarro. *Microfabricated tuneable and transferable porous PDMS membranes for Organs-on-Chips.* Scientific Reports, 8, 13524 (2018).

4. Giorgio Pennazza, Marco Santonico, Luca Vollero, Alessandro Zompanti, Anna Sabatini, Nandeesh Kumar, Ivan Pini, **W. F.Quirós-Solano**, P.M.Sarro and Arnaldo DAmico. *Advances in the Electronics for Cyclic Voltammetry: the Case of Gas Detection by Using Microfabricated Electrodes.* Frontiers in Chemistry, 6, 327 (2018).

5. Nikolas Gaio, Berend van Meer,**W. F.Quirós-Solano**, Lambert Bergers, Anja van de Stolpe, Christine Mummery, P.M. Sarro and Ronald Dekker. *Cytostretch, an Organ-on-Chip Platform.* Micromachines, 7, 7 (2016).

CONFERENCE PROCEEDINGS PAPERS

1. N.Gaio, Sebastiaan Kersjes, **W.F.Quirós-Solano**, P.M.Sarro and R.Dekker. *Versatile and Automated 3D Polydimethylsiloxane (PDMS) Patterning for Large-Scale Fabrication of Organ-on-Chips.* 32nd Eurosensors Conference, EUROSENSORS, 2018.

2. **W.F.Quirós-Solano**, N. Gaio, C. Silvestri, Y.B. Arik, O.M.J.A. Stassen, A.D. van der Meer, C.V.C. Bouten, A. van den Berg, R. Dekker and P.M. Sarro. *A novel method to transfer porous PDMS membranes for high throughput Organ-on-Chip and Lab-on-Chip assembly.* 31st IEEE International Conference on Micro Electro Mechanical Systems (MEMS), 2018.

3. **W.F.Quirós-Solano**, N.Gaio, C.Silvestri, G.Pandraud and P.M.Sarro. *Polymeric strain gauges as pressure sensors for microfabricated organ-on-chips.* The 19th International Conference on Solid-State Sensors, Actuators and Microsystems, 2017.

4. **W.F.Quirós-Solano**, N. Gaio, C. Silvestri, G. Pandraud, P.M. Sarro. *PEDOT:PSS: a Conductive and Flexible Polymer for Sensor Integration in Organ-on-Chip Platforms.* 30th Eurosensors Conference, EUROSENSORS, 2016.

5. **W.F.Quirós-Solano**, G. Pandraud, P.M. Sarro. *Wafer-level fabrication of strain gauges on PDMS membranes for low-pressure sensing.* IEEE Sensors, 2015.

PATENTS

1. N.Gaio and **W.F.Quirós-Solano**. *Versatile 3D Stretchable Micro-Environment for Organ-on-Chip Devices Fabricated with Standard Silicon Technology.* Patent Granted in NL, NL2017227B1, 2018 in PCT Phase, WO2018021906A1.

RESEARCH PROPOSAL CONTRIBUTIONS

1. *BI/OND: The Versatile Organ-on-Chip platform.* Take-off phase II, Early-phase Project, 2018.

2. *Design, Fabrication and Testing of an User-Friendly Interface for Organ on Chips.* Take-off phase I, Feasibility Study, 2018.

3. *Developing a validated Cancer-on-Chip prototype for personalized medicine.* KWF - Unique High Risk Project, 2018.

4. *BIOND the Lab: Versatile Organ-on-Chip Platform toward the market.* EIT Health Proof of Concept - Head Start Project, 2018.

5. *Membranes for a Heart Valve on a Chip.* Nanoinside Pilot Project Proposal, Funded by NanoNextNL, 2017.

6. *Towards realistic barriers: Bringing microfabrication and Organ-on-Chips tehcnology together to model cellular barriers.* Nanoinside Pilot Project Proposal, Funded by NanoNextNL, 2017.

7. *BIOND: A Universal OOC platform.* NanoNextNL Valorisation Grant, 2016.

WORKSHOPS AND POSTER PRESENTATIONS

1. S. Chakrabarty, N.Gaio, **W.F.Quirós-Solano**, M. Kuijten, H. Odijk , Jos Jonkers, R. Dekker, R. Kanaar, D. van Gent. *Cancer-on-chip: optimizing models for personalized medicine.* EURoOC Conference, Graz, Austria, 2019.

2. J. Stein, M, De Graaf, N.Gaio, **W.F.Quirós-Solano**,C.Silvestri,L. Van Den Hill, E. Giacomelli, B. van der Meer, R. van Helden, V. Orlova, M. Bellin and C. Mummery. *A multicellular approach to iPSC-derived myocardium on a microfluidic platform for human disease modelling.* EURoOC Conference, Stuttgart, Germany, 2018.

3. O. M. J.A. Stassen, N.C.A.Van Engeland, **W.F.Quirós-Solano**, N.Gaio, A. Pollet, J.M.J. Toonder, R.Dekker, P.M. Sarro, C. M. Sahlgren and C.V. C. Bouten. *Cardiovascular-tissue-on-a-chip to study crosstalk between hemodynamics and cell-cell signalling in tissue engineering outcome.* 1^{st} International Conference on Tissue Engineered Heart Valves, Amsterdam, The Netherlands, 2018.

4. N. Gaio, C. Silvestri, **W.F. Quirós-Solano**. *Versatile Organ-on-Chip Platform.* International MicroNano Conference 2017, Amsterdam, The Netherlands, 2017.

5. **W.F.Quirós-Solano**, N.Gaio, Y.B. Arik, A. Van der Meer, R.Passier, R.Dekker, Albert van den Berg and P.M. Sarro. *Highly porous and transferable microfabricated PDMS membranes for Organ-on-Chip.* Design of Medical Devices Conference Europe (DMD) Europe - Microfabrication for medical devices, Eindhoven, The Netherlands, 2017.

6. N. Gaio, **W.F. Quirós-Solano**, P. Dijkstra, T. van Weelden, E. Boschman, R. Dekker. *Cystostretch: A Multi-Well Plate Heart-on-Chip Device.* Design of Medical Devices Conference Europe (DMD 2017), Eindhoven, The Netherlands, 2017.

7. **W.F.Quirós-Solano**, N.Gaio, Y.B. Arik, C.Silvestri, A. Van der Meer, R.Passier, and P.M. Sarro. *Highly porous microfabricated PDMS foils for Organ-on-Chip applications.* International Organ-on-Chip Symposium, Lausanne, Switzerland, 2017.

8. N. Gaio, **W.F. Quirós-Solano**, C. Silvestri, P.M. Sarro, R. Dekker. *Cytostretch Platform: Towards the Industrialization of an Heart-on-Chip Device.* International Organ-on-Chip Symposium, Lausanne, Switzerland, 2017.

9. **W.F.Quirós-Solano**, N.Gaio, G.Pandraud and P.M. Sarro. *Sensing devices in Organ-on-Chip: Towards an integrated sensing microtechnology for heart cells study.* ICT OPEN Conference, Amersfoort, The Netherlands, 2016.

10. N. Gaio, **W.F. Quirós-Solano**, R. Dekker. *Large-Scale fabrication of PDMS membranes for Organ-on-Chip applications.* ICT OPEN Conference, Amersfoort, The Netherlands, 2016.

AWARDS RELATED TO THIS THESIS

1. BI/OND, *NanoLabNl Voucher*, May, The Netherlands, 2019.

2. BI/OND, *Phillips Innovation Award*, May, The Netherlands, 2019.

3. BI/OND, *Accenture Innovation Award* in Health section, November, The Netherlands, 2018.

4. *Best innovative idea*, 12 STARTUP weekend, YES!Delft, March, The Netherlands, 2016.

ACKNOWLEDGEMENTS

The richest and one of the most challenging experiences of my life has come to an end. This life stage has taught me new things about science and technology, but more importantly it has contributed to my personal growth. All these would have never been possible without the support and companionship from many people.

First and foremost, I should start acknowledging all those people and institutions that together enabled me to pursue a Ph.D. I must thank the Instituto Tecnológico de Costa Rica (*la alma matter*), which provided me the scholarship and financial support to start my doctoral studies. I express my sincere gratitude to Dr. Julio Calvo Alvarado, Dpl.-Ing. Luis Paulino Mendez Badilla, Dr. Roberto Pereira Arroyo, Ing. Francisco Navarro Enríquez, Dr.-Ing. Paola Vega Castillo, Ing. Anibal Coto Cortez, Alfonso Chacón Rodríguez and all the members of the School of Electronics Engineering and the Scholarships Department. I must particularly thank to Dr. Saúl Guadamuz Brenes and Ing. Arys Carrasquilla Batista for their unconditional trust.

To my promotor, Prof.dr.ir. Lina Sarro, I am grateful for giving me the opportunity to pursue my Ph.D at the Electronic Components, Technology and Materials (ECTM). Prof, I could not express sufficiently my gratitude and admiration towards you. Thanks for believing in me since the very beginning and the support in good and difficult times over the past years. I appreciate all the lessons you taught me about research but especially the ones that helped me for personal growth. Thanks for the discussions, brainstorming and the freedom given to develop my research. I feel immensely proud of having the opportunity of being under the supervision of such recognized, successful and experienced researcher.

I must definitively also thank Prof.dr.ir. Ronald Dekker. Ronald, I will always appreciate your enthusiasm and vivid encouragement towards new ideas. Thanks for briefly introducing me to the topic of Organ-on-Chip. Your passion and superb clarity when exposing and explaining complex topics convinced me more to focus my research on this topic. I appreciate your unconditional support and encouragement along the last years. I am proud of having the opportunity to work close to such highly experienced researcher. I will always be grateful for many things about technology that I learned from you.

Of course, to Dr. Gregory Pandraud. Gregory (Boss), I will always appreciate the discussions about design and fabrication, and all the tricks to optimize fabrication processes. Many thanks for the brainstorming and troubleshooting when I was totally inexperienced in processing, and specially for motivating me when I was getting stuck at some point.

I would like to express my appreciation to the committee members, Prof.dr. Peter Steeneken, Prof.dr.rer.nat. Wilfried Mokwa, Prof.dr.ir. Jaap den Toonder, Prof.dr. Giuseppe Barillaro and Prof.dr. Paddy French. I am honoured that such highly knowledgeable, experienced and recognized researchers read and evaluated my work.

To The Institute for human Organ and Disease Model technologies (hDMT), thanks for enabling and promoting over the last years collaborative and multidisciplinary research in Organ-on-Chip technologies in The Netherlands and all over Europe. Thanks to hDMT it was also possible the materialization of collaborations to perform some of the preliminary biological experiments presented in this thesis. Particularly, thanks to Dr. Janny van den Eijnden - van Raaij and Dr. Mieke Schutte for creating such a nice and constructive environment for brainstorming within such an heterogeneous group of people. I really admire your determination to make of hDMT a success and to contribute with the progress of science and technology in healthcare. The parts of this thesis concerning biological experiments were possible thanks to the contribution of Profesors, Postdocs and PhD students from Eindhoven University of Technology (TU/e), Twente University (UTwente), Leiden University Medical Center (LUMC) and Erasmus Medical Center (Erasmus MC). Particularly, I shall thank to Dr. Oscar Stassen and Yusuf Arik for our nice brainstorming sessions and successful collaboration and for taking some steps along to bring technology and biology together.

To Else Kooi Laboratory, thanks for making available the facilities to carry out most of the experiments. Tom Scholtes, thanks for all your advices and sharp feedback given during processing, I do really appreciate your interest to help me improving the fabrication processes. I am also grateful to Robert Verhoeven, thanks for the kind availability and help when requesting and handling new chemicals. Koos van Hartingsveldt, thanks also for the kind availability and the dicing tricks. To Hitham Mahnoud, thanks for the discussions on chemistry and your kind availability. To Bianca Knot, thanks for your kind availability and supporting us over the last years. To Silvana, Johannes, Mario, Joost, Loek, Wim, Alex, Cassan, Giles, Ruud, Johan, Jan Cornelis, Ron thanks for keeping the cleanroom up and running all these years.

I would also like to express my gratitude to Marian Roozenburg. Thanks for all you have done, since the very beginning when I was a lost Costa Rican student you helped me go through the cultural transition smoothly. Special thanks for helping us (The Ticos) to organize the Annual Review party and make possible for us to share with the group a bit of our country, traditions and more importantly our food. To Annegreeth Lameijer, thanks for all your advice to handle IP matters, management, conflicts and negotiations. Many thanks also to Rosario Salazar, who keeps all the financial matters running. I must thank Minke van der Put and Everdine de Vreede for their assistance. To Wim Tiwon, thanks for all your help with the servers and IT issues. Without the knowledge, assistance and experience of you all things will never happen.

I came across with many colleagues at the ECTM along these years. It has been a pleasure to share this time with you in such a nice, collaborative and constructive environment. Among past and present member of the group I thank: Boyao Sun, Yelena Grachova, Pan Liu, Brahim Mansouri, Luke Middelburg, Manjunath Ramachandrapa Venkatesh, Robert Sokolowski, Xueming Li, Penfei Sun, An Tran, Violeta Prodanovic, Aleksandar Jovic, Hang Bui, Hong Wah Chan, Nello Franzese, Uto Toshihiko, Angel Savov, Ronald Stoute, Shivani Joshi, Lambert Vergers, Amir Sammak, Miki Trifunovic, Tonie van Loon, Jia Wei, Amir Mirza Gheitaghy, Fabio Rodriguez, Enrico Serra, Massimo Mastrangeli, Leandro Sacco, Hande Aydogmus, Milica Dostanic, Fengze Hou, Hao Zang, Hongyu Tang, Jian Li, Jianwen Sun, Shinnosuke Kawasaki, Safoora Khosravi, Paul Motreuil-

Ragot, Alexandru Prisacaru, Joos Romijn, Tianfeng Wang, Tianyi Jin, Xu Li, Yue Sun, Zhen Cui, Salvatore Forte, Giuseppe Fiorentino, Rene Poelma, Yu Zhang and others. I appreciate you all for the time we interact either in the coffee corner, corridors or inside the cleanroom. Special thanks to Joost van Ginkel for translating the summary of this thesis.

I would also like to particularly thank the officemates I had along the Ph.D. I had the opportunity to be in two different rooms, where I shared space with nice and special people. First, thanks to Jing Zhang, Marian Yazdan Mehr, Peters Tjitte-Jelte and Alessandro Zompanti for make me feel welcomed since the very first day I came to my first office. I appreciate your help to deal with the issues that young Ph.D students initially encounter, such as learning how to print, ventilate frustrations, how to get a coffee or thee (not that I would die without a coffee from those machines) or even define what needs to be done the next four years of our lives. To Daniel Li and Zahra Kolahdouz Esfahani, thanks for kindly receiving me at your office for the last two years.

I would like to thank to the daily life colleagues and friends whom I was sharing lunch and coffee breaks with. To Marta, Bruno, Loana, Filiberto, Leandro and Paolo, thanks for letting me join and enabling my transition towards the "non-Dutch, namely Italian" lunch time. I appreciate all the discussions and fun we had during these spare times. I hope we keep in touch and cultivating a friendship outside the work environment.

I am immensely grateful also to people that always believed in me since long before I started my Master at Instituto Tecnológico de Costa Rica. Thanks to Dpl.-Ing. Arnoldo Rojas Coto for enabling my first experience in teaching assistance (Tutoría). I will always appreciate listening to you sharing your vast knowledge and how you easily handle all sort of topics. To Dr.-Ing. Pola Vega Castillo, thanks for believing in my potential since the very beginning of my Masters and introducing me to the MEMS field, which ultimately influenced the decision to pursue the Ph.D. I will never forget your lectures about Microelectronics and MEMS, the passionate way you handle, comprehend and transmit every small and important detail. I must definitively thank to M.Sc. Marta Vílchez Monge, who also saw potential in me from the very beginning. Thanks for your teachings and always encouraging me to improve myself along the time we shared at our Masters. To Dr. Gabriela Ortiz León, many thanks for back then giving me the opportunity to work on my Master thesis with you. I also appreciate you believing on me and for always encouraging to go further and improve myself.

To the intimate and highly valued group of Costa Rican friends (Ticos), I appreciate your presence during good and difficult times over the last years and all experiences shared as expats in The Netherlands. Many thanks to Víctor Vega Garita (already Dr. Vega), Ana Lucía Parra Trejos and of course Tomas Vega Parra (he is growing fast). I enjoyed very much the Costa Rican gatherings we had to relax and share a bit of good food and other celebrations. To Johan Carvajal Godínez, though we have not shared that many experiences here, I appreciate your friendship and thank you for always supporting us (Me and Laura) since we were B.Sc. students few years ago. To Juan Andrés Alfaro Barrantes, thanks for sharing a friendship since already many years and for your support at work and other various matters. It was definitively a privilege to have the perspective from you, another Costa Rican, in an international working environment. Many thanks to Eduardo Santamaría Quesada, who somehow was also there at the precise moment to provide me support to reach the end.

Cinzia and Nikolas, I am proud to have the opportunity of sharing many exciting and challenging experiences with you. I have grown and learned so much next to you; to believe more in myself, take more risks and to keep up despite the difficult circumstances, among many others. Nikolas, I admire the passion and energy that you put in every thing you do, I strongly believe that if you keep on doing everything the way you do you would succeed at whatever you try. Thanks also for all the brainstorming session we had, the crazy ideas we tried (successes and fails) and for being able to cope with my communication style (e.g. when inspecting things under the microscope).
Cinzia, I admire the passion you put into things, the attention to small details and your capability to adapt to change and keep up despite difficulties. Thanks for your unconditional trust and specially for always being so attentive to my well-being. I appreciate all your help when structuring and organizing ideas, and all the reviews you did when I was preparing written documents. I wish I can have those writing skills. Please keep on going, I believe there a many great things still to come for you. For all these and more I am immensely grateful to you both, but mostly for your unconditional friendship and enabling this adventure that goes BI/OND ourselves. I hope we can preserve our special connection beyond BI/OND.

I shall finish writing in Spanish as it is very important to me that those I will acknowledge fully understand and realize my appreciation.

Madre mía, nunca hubiera llegado tan largo sin usted y en especial sin los sacrificios que incondicionalmente hizo para poder darme la mejor educación posible. La mayor herencia que me puede dar es eso, la educación y una mejor preparación para enfrentar el resto de la vida. Nos salimos de su manos sí, pero para volar alto y sin nunca olvidar el nido del que siempre estaremos pendiente. Hermana, gracias por siempre estar ahí para mí y resguardarme desde que tengo memoria, sin usted a la par no sé que hubiera sido de mí. Ita y tío, gracias por ser el apoyo inmediato en los tiempos de dificultad y por los sacrificios que hicieron para hacer posible mi educación y bienestar. A Felipe, Marielena, Luigi (Luis Diego), Hector, Flory (Floribeth), Pablo y Albert (Felipe), gracias por siempre estar cerca pendiente de mami, ita y tío durante el tiempo que he estado tan lejos los últimos años. Luigi, gracias por el concepto, diseño y realización de la portada.

Al resto de mi familia mi apreciación y agradecimiento, a los gemelos (Carlos y Jorge), Tío Chito (Hector), Tío Victor y Lidiete, y todos los primos de Juan Viñas (Marilia, Rosibel, Anabelle, Laura, Iris) y de San Jose (Rodolfo, Adrian, Pablo, Sandra, Royner) y sus hijos, gracias por también estar pendiente de la casa y sus palabras de apoyo en determinado momento. Si se me escapa algún nombre, me disculpo y le agradezco de todo corazón.

A Laura, mi novia y confidente, la persona que me ha acompañado en las buenas y malas. No tengo suficientes palabras para expresar mi amor y agradecimiento hacia vos. Muchos obstáculos que he superado en los últimos años ha sido gracias a tu apoyo incondicional en todo momento. Gracias por ayudarme a levantarme y motivarme a seguir hacia adelante a pesar de las circunstancias. Sin tus palabras reconfortantes y tu actitud positiva no hubiera podido llegar al final de esta aventura. Todavía nos quedan muchas más aventuras por delante, como siempre juntos somos un gran equipo.

From sugarcane and coffee fields to windmills and tulip fields.

William Quirós Solano, June, 2019